University of Stavanger

Faculty of Science and Technology

MASTER'S THESIS

Study program/ Specialization: Marine- and Offshore Technology	Spring semester, 2019 Open / ~~Restricted access~~
Writer: Martin Bakk Andersen	(Writer's signature)
Faculty supervisor: Prof. Muk Chen Ong Dr. Guang Yin	
Thesis title: Numerical Simulations of Flow Around Subsea Covers at High Reynolds Number	
Credits (ECTS): 30	
Key words: Computational Fluid Dynamics, CFD, OpenFOAM, wall-mounted trapezoids, Turbulent flow over Bluff bodies, tandem	Pages: ……71…… + enclosure: …18…… Stavanger, 15 June 2019 Date/year

Abstract

The present study investigates turbulent flow over square and trapezoidal wall-mounted subsea covers in single and tandem configuration.

The structures under investigation in the single configuration are subjected to a turbulent boundary layer flow at Reynolds numbers of $1.19 \times 10^5$and 1×10^6 (based on the height of the structures and the free stream velocity) using Reynolds-averaged Navier-Stokes (RANS) equations combined with the $k - \omega$ Shear Stress Transport (SST) turbulence model. The mesh independence is assessed and comparisons with the published data are made. The results are found to be reasonably accurate as compared to the published data. Time averaged results for pressure, velocity profiles, bed shear stress and hydrodynamic coefficients around single structures are investigated for different trapezoidal configurations.

The structures in tandem configuration are subjected to the same flow conditions as the single structure case at the Reynolds number of 1.19×10^5 using the Reynolds-averaged Navier-Stokes (RANS) equations combined with the $k - \omega$ Shear Stress Transport (SST) turbulence model. The mesh independence studies with the variation of the normalized gap ratio G/D between the two structures are carried out. Time averaged results for pressure, horizontal velocity profile and hydrodynamic coefficients around structures in tandem are studied with different G/D and trapezoidal configurations.

Acknowledgements

This thesis completes my master's degree in Marine Offshore technology at the University of Stavanger (UIS). I want to thank my supervisors Prof. Muk Chen Ong and Dr Guang Yin for their motivation and help with my work. I would like to extend my sincere thanks to Dr Yin for providing academical and technical support throughout my thesis.

I'm also grateful to Marek Janocha and my co-students Kjartan Eie and Bjørnar Nitter for support and insightful conversations on the topic of computational fluid dynamics.

I would like to thank the University of Stavanger, Department of Mechanical and Structural Engineering and Materials Science for providing the resources necessary to carry out the present study.

Finally, I would like to thank my family and girlfriend for their encouragement and love.

Table of Contents

ABSTRACT I

ACKNOWLEDGEMENTS II

TABLE OF CONTENTS III

LIST OF FIGURES VI

LIST OF TABLES VIII

ABBREVIATIONS IX

LIST OF SYMBOLS X

1 INTRODUCTION 13

1.1 Background and motivation 13

1.2 Literature review 14

1.3 Outline 16

2 THEORY 17

2.1 Flow physics around immersed wall-mounted structures 17

2.2 Turbulence 18

2.2.1 Reynolds Number 18

2.2.2 Laminar and Turbulent flow 18

2.2.3 Boundary Layer 20

2.3 Hydrodynamic Coefficients 24

3 COMPUTATIONAL FLUID DYNAMICS 25

3.1 OpenFOAM 25

3.1.1 Meshing and Pre-Processing 26

3.1.2 Solving 26

3.1.3 Courant number 26

3.1.4 Post- processing 27
3.2 Governing Equations 27
3.2.1 Mass and momentum conservation 27
3.2.2 Reynolds-Averaged Navier Stokes RANS.....27
3.2.3 $k-\omega$ SST Turbulence Model 28
3.3 Finite Volume Method.....30
3.4 simpleFoam.....31
4 COMPUTATIONAL MODEL 33
4.1 Model description 33
4.2 Boundary Conditions 34
4.2.1 Inlet 34
4.2.2 Walls: Bottom and Structures 35
4.2.3 Outlet, Top and Front & Back.....35
4.3 Computational mesh 36
5 RESULTS AND DISCUSSION FOR SINGLE CASE.....37
5.1 Convergence study.....38
5.2 Validation study.....42
5.3 Effect of α on hydrodynamic quantities and xR/D 45
5.4 Velocity and Pressure Distributions 46
5.5 Bed shear stress and Scour.....52
5.6 Streamlines.....53
6 RESULTS AND DISCUSSION FOR TANDEM CASE 56
6.1 Convergence 57
6.2 Effects of G/D and α on hydrodynamic quantities 59
6.3 Pressure distribution 62
6.3.1 Pressure distribution for squares in tandem 62

6.3.2 Pressure distribution for trapezoids in tandem 64
6.4 Horizontal velocity contours 68
6.4.1 Horizontal velocity contours for squares in tandem 68
6.4.2 Horizontal velocity contours for trapezoids in tandem 70
6.5 Streamlines 74
6.5.1 Streamlines over tandem squares 74
6.5.2 Streamlines over trapezoids in tandem 76
7 CONCLUSIONS 79
7.1 Structures in single configuration 79
7.2 Structures in tandem configuration 80
7.3 Future work 80

List of Figures

FIGURE 1.1 GRP COVER OVER SUBSEA INSTALLATION (WWW.HIGHCOMP.NO) 13

FIGURE 2.1 LAMINAR, TRANSITIONAL AND TURBULENT FLOWS OVER A FLAT PLATE (CENGEL & CIMBALA, 2017) 19

FIGURE 2.2 INSTANTANEOUS TURBULENT VELOCITY VARIATION WITH RESPECT TO TIME (VERSTEEG & MALALASEKERA, 2007) 19

FIGURE 2.3 TURBULENT FLOW OVER A FLAT PLATE (FUNDAMENTALS OF HEAT AND MOMENT TRANSFER, 8TH EDITION) 21

FIGURE 2.4 BOUNDARY LAYER REGIONS (TAUQEER, 2016) 22

FIGURE 3.1 ORGANIZED OPENFOAM FOLDERS FOR THE PRESENT STUDY 25

FIGURE 3.2 FLOW CHART OF THE SIMPLE ALGORITHM 31

FIGURE 4.1 COMPUTATIONAL DOMAIN AND BOUNDARY CONDITIONS FOR SINGLE STRUCTURE CASE 33

FIGURE 4.2 COMPUTATIONAL DOMAIN AND BOUNDARY CONDITIONS FOR TANDEM CASE 34

FIGURE 4.4 MESH STRUCTURE FOR $\mathrm{A} = 15°$ AT $Re = 1 \times 106$ 36

FIGURE 4.3 MESH STRUCTURE FOR FOR $\mathrm{A} = 30°$ AT $Re = 1.19 \times 105$ 36

FIGURE 5.1 MESH CONVERGENCE WITH RESPECT TO HYDRODYNAMIC COEFFICIENTS FOR $Re = 1.19 \times 105$ (LEFT SIDE) AND $Re = 1.0 \times 106$ (RIGHT SIDE) 40

FIGURE 5.2 COMPARISONS OF HORIZONTAL VELOCITY PROFILES OF THE PRESENT SIMULATION AND EXPERIMENTAL DATA FROM LIU ET AL. (2009) 43

FIGURE 5.3 EFFECT OF A ON HYDRODYNAMIC QUANTITIES: (A) C_D, (B) C_L AND (C) X_R/D 45

FIGURE 5.4 PRESSURE CONTOURS FOR WALL-MOUNTED SQUARES IN TANDEM WITH GAP RATIOS OF: A) G/D = 2, B) G/D = 3, C) G/D = 6, D) G/D = 10 AND E) G/D = 14 47

FIGURE 5.5 HORIZONTAL VELOCITY CONTOURS AT $\mathrm{RE} = 1 \times 106$ FOR VARYING α: (A) $0°$, (B) $15°$, (C) $30°$, (D) $45°$ AND (E) $60°$ 49

FIGURE 5.6 VERTICAL VELOCITY CONTOURS AT $\mathrm{RE} = 1 \times 106$ FOR VARYING α: (A) $0°$, (B) $15°$, (C) $30°$, (D) $45°$ AND (E) $60°$ 51

FIGURE 5.7 BED SHEAR STRESS ALONG THE BOTTOM SURFACE AT $\mathrm{RE} = 1 \times 106$ FOR: A) THE WHOLE DOMAIN. B) THE FRONT FACE OF THE STRUCTURES 52

FIGURE 5.8 DETAILED STREAM LINES FOR RE=1×10^6 FOR (A) A=0° AND (B) A=60° 53

FIGURE 5.9 STREAM LINES AT $\mathrm{RE} = 1.19 \times 105$ FOR VARYING A: (A) $0°$, (B) $15°$, (C) $30°$, (D) $45°$ AND (E) $60°$ 54

FIGURE 5.10 STREAM LINES AT $\mathrm{RE} = 1 \times 106$ FOR VARYING A: (A) $0°$, (B) $15°$, (C) $30°$, (D) $45°$ AND (E) $60°$ 55

FIGURE 6.1 CONVERGENCE STUDY FOR WALL-MOUNTED SQUARES IN TANDEM WITH $G/D = 2,3,6,10$ AND 14 FOR THE HYDRODYNAMIC QUANTITIES: A) $CD1$ FOR SQUARE1, B) $CD2$ FOR SQUARE2, C) $CL1$ FOR SQUARE1 AND D) $CL2$ FOR SQUARE2 58

FIGURE 6.2 INVESTIGATION OF GAP RATIOS G/D FOR DIFFERENT CONFIGURATIONS OF α FOR THE HYDRODYNAMIC QUANTITIES: A) $CD1$ FOR SQUARE 1, B) $CD2$ FOR SQUARE 2, C) $CL1$ FOR SQUARE 1 AND D) $CL2$ FOR SQUARE 2 60

FIGURE 6.3 INVESTIGATION OF α FOR GAP RATIOS OF $G/D = 6,10,14$ AS WELL AS FOR SINGULAR STRUCTURES, FOR THE HYDRODYNAMIC QUANTITIES: A) CD FOR SQUARE 1, B) CD FOR SQUARE 2, C) CL FOR SQUARE 1 AND D) CL FOR SQUARE 2 61

FIGURE 6.4 PRESSURE CONTOURS FOR WALL-MOUNTED SQUARES IN TANDEM WITH GAP RATIOS OF: A) $G/D = 2$, B) $G/D = 3$, C) $G/D = 6$, D) $G/D = 10$ AND E) $G/D = 14$ 63

FIGURE 6.5 PRESSURE CONTOURS FOR $G/D = 6$ FOR VARYING TRAPEZOIDAL CONFIGURATIONS A: (A) $0°$, (B) $15°$, (C) $30°$, (D) $45°$ AND (E) $60°$ 65

FIGURE 6.6 PRESSURE CONTOURS FOR $G/D = 10$ FOR VARYING TRAPEZOIDAL CONFIGURATIONS A: (A) $0°$, (B) $15°$, (C) $30°$, (D) $45°$ AND (E) $60°$ 66

FIGURE 6.7 PRESSURE CONTOURS FOR $G/D = 14$ FOR VARYING TRAPEZOIDAL CONFIGURATIONS A: (A) $0°$, (B) $15°$, (C) $30°$, (D) $45°$ AND (E) $60°$ 67

FIGURE 6.8 HORIZONTAL VELOCITY CONTOURS FOR WALL-MOUNTED SQUARES IN TANDEM WITH GAP RATIOS OF: A) $G/D = 2$, B) $G/D = 3$, C) $G/D = 6$, D) $G/D = 10$ AND E) $G/D = 14$ 69

FIGURE 6.9 HORIZONTAL VELOCITY CONTOURS FOR $G/D = 6$ FOR VARYING TRAPEZOIDAL CONFIGURATIONS A: (A) $0°$, (B) $15°$, (C) $30°$, (D) $45°$ AND (E) $60°$ 71

FIGURE 6.10 HORIZONTAL VELOCITY CONTOURS FOR $G/D = 14$ FOR VARYING TRAPEZOIDAL CONFIGURATIONS A: (A) $0°$, (B) $15°$, (C) $30°$, (D) $45°$ AND (E) $60°$ 73

FIGURE 6.11 TIME-AVERAGED STREAMLINES OVER WALL-MOUNTED SQUARES IN TANDEM WITH GAP RATIOS OF: A) $G/D = 2$, B) $G/D = 3$ AND C) $G/D = 6$ 74

FIGURE 6.12 STREAMLINES FOR WALL-MOUNTED SQUARES IN TANDEM WITH GAP RATIOS OF: A) $G/D = 2$, B) $G/D = 3$, C) $G/D = 6$, D) $G/D = 10$ AND $G/D = 14$ 76

FIGURE 6.13 STREAMLINES FOR G/D = 6 FOR VARYING TRAPEZOIDAL CONFIGURATIONS A: (A) $0°$, (B) $15°$, (C) $30°$, (D) $45°$ AND (E) $60°$ 77

FIGURE 6.14 STREAMLINES FOR G/D = 14 FOR VARYING TRAPEZOIDAL CONFIGURATIONS A: (A) $0°$, (B) $15°$, (C) $30°$, (D) $45°$ AND (E) $60°$ 78

List of Tables

TABLE 5.1 HYDRODYNAMIC QUANTITIES FOR VARYING A WITH DIFFERENT GRIDS AT $Re = 1.19 \times 105$ 38

TABLE 5.2 HYDRODYNAMIC QUANTITIES FOR VARYING A WITH DIFFERENT GRIDS AT $Re = 1 \times 106$ 38

TABLE 6.1 RESULTS OF CONVERGENCE STUDY FOR HYDRODYNAMIC COEFFICIENTS FOR SQUARE 1 AND SQUARE 2 56

TABLE 6.2 HYDRODYNAMIC COEFFICIENTS FOR STRUCTURE 1 AND STRUCTURE 2 WITH G/D = 6 FOR TRAPEZOIDAL CONFIGURATIONS USING MESH NUMBER OF 66855 57

TABLE 6.3 HYDRODYNAMIC COEFFICIENTS FOR STRUCTURE 1 AND STRUCTURE 2 WITH G/D = 10 FOR TRAPEZOIDAL CONFIGURATIONS USING MESH NUMBER OF 76395 57

TABLE 6.4 HYDRODYNAMIC COEFFICIENTS FOR STRUCTURE 1 AND STRUCTURE 2 WITH $G/D = 14$ FOR TRAPEZOIDAL CONFIGURATIONS USING MESH NUMBER OF 89115 57

Abbreviations

2D	Two-dimensional
3D	Three-dimensional
CFD	Computational Fluid Dynamics
CFL	Courant Friedrichs Lewy number
DNS	Direct Numerical Simulation
GRP	Glass reinforced plastic
LES	Large Eddy Simulation
RANS	Reynolds-Averaged Navier-Stokes
SIMPLEC	Semi-Implicit Method for Pressure Linked Equations Constant
SST	Shear Stress Transport

List of Symbols

α	Angle of steepness for trapezoids	[°]
δ	Boundary layer thickness	$[m]$
ε	Dissipation rate	$[m^2/s^3]$
μ	Dynamic viscosity	$[kg/m \cdot s]$
κ	von Kàrmàn constant	$[-]$
ν	Kinematic viscosity	$[m^2/s]$
τ	Bed shear stress	$[kg/m \cdot s^2]$
τ_∞	Undisturbed bed shear stress	$[kg/m \cdot s^2]$
ρ	Fluid denisty	$[kg/m^3]$
ω	Specific dissipation rate	$[s^{-1}]$
A	Projected area	$[m^2]$
C_D	Drag force coefficient	$[-]$
C_L	Lift force coefficient	$[-]$
D	Diameter/characteristic length	$[m]$
F_D	Drag force	$[kg \cdot m/s^2]$
F_L	Lift force	$[kg \cdot m/s^2]$
G	Gap distance	$[m]$
k	Turbulence kinetic energy	$[m^2/s^2]$
Ld	Dimensionless downstream length	$[-]$
Lu	Dimensionless upstream length	$[-]$
Ma	Mach number	$[-]$
P	Dynamic pressure	$[m^2/s^2]$
p	Pressure	$[kg/m \cdot s^2]$
Re	Reynolds number	$[-]$
U	Mean velocity	$[m/s]$
U_∞	Free stream flow velocity	$[m/s]$
u	Velocity in the x direction	$[m/s]$
u′	Fluctuating velocity	$[m/s]$
u^+	Dimensionless velocity	$[-]$

u_τ	Shear flow velocity	$[m/s]$
v	Velocity in the y direction	$[m/s]$
x	Horizontal length	$[m]$
x_R	Recirculation length	$[m]$
y	Vertical length	$[m]$
y^+	Dimensionless distance from the wall	$[-]$

1 Introduction

1.1 Background and motivation

The offshore industry is continuously shifting to deeper waters with advanced subsea equipment in the Norwegian continental shelf. The submerged equipment is exposed to impact loads from dropped objects and environmental loads exerting on the seabed. Therefore, protection covers are often required to shield the most exposed components from critical impact loads. Glass reinforced plastic (GRP) covers have recently been used widely due to its low-cost, high strength and good corrosion properties. The GRP covers are produced in various shapes and sizes, and often as elongated ribs to cover pipeline segments. However, the weight of a GRP cover is typically one third of a subsea steel cover with the equivalent size; hence, it is more sensitive to hydrodynamic forces (Nymo, 2015).

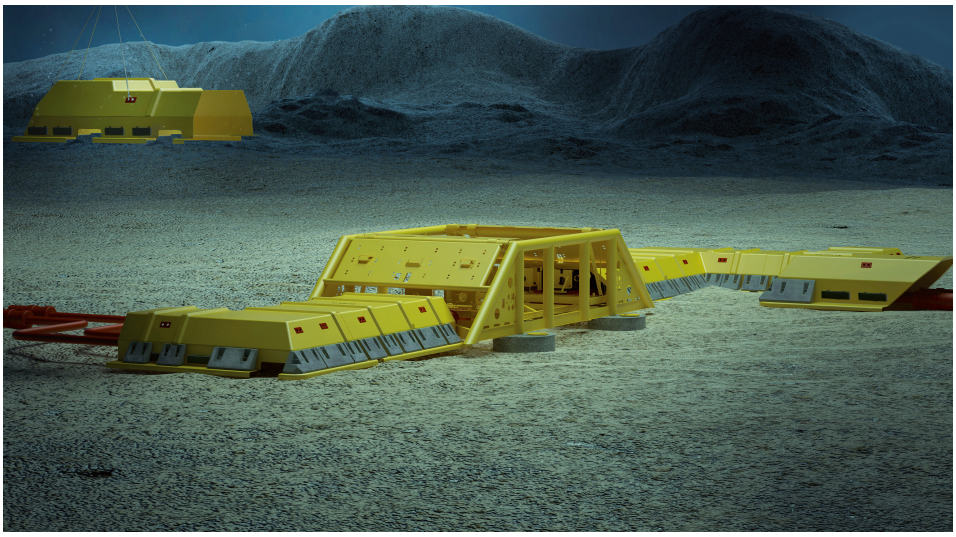

Figure 1.1.1 GRP cover over subsea installation (www.highcomp.no)

The seabed flow forces imposed on the GRP covers are composed of the current and wave induced streams resulting in a high Reynold turbulent boundary layer flow. The GRP covers are regularly subjected to extreme subsea environmental conditions and at a typical Reynolds number of $300 < Re < 3 \times 10^5$ (sub-critical regime) and $Re > 4 \times 10^6$ (transcritical regime) (Ong et al, 2010). Here $Re = U_\infty D/\nu$ where U_∞ is the free stream velocity and D is the

structure/cover height and ν is the kinematic viscosity of the fluid. Flows around these structures are complex and depends on various parameters such as Reynolds number, normalized boundary layer thickness δ/D (δ is the incident boundary layer thickness) and the shape of the structures (Adams & Johnston, 1988). Analytical solutions for these types of flow problems are yet not feasible for engineering design. Hence, experimental and numerical investigations are needed to study the hydrodynamic behaviors.

In recent years, Computational Fluid Dynamics (CFD) has become a popular method when investigating high Reynolds flow problems. Recent advances in computing power and software development have made CFD more accessible for both industry and research purposes. In an economical point of view, Reynolds-Averaged Navier-Stokes RANS is preferred over Direct Numerical Simulation (DNS) and Large Eddy Simulation (LES) due to lower computational cost as well as giving reasonable engineering accuracy in predicting the hydrodynamic forces.

This thesis will investigate boundary layer flow over two dimensional subsea covers in single and tandem configurations using the RANS k-ω SST turbulence model. Hydrodynamic coefficients, bed shear stress, recirculation length, pressure distribution and velocity profiles will be studied for different bottom angles of the trapezoidal configurations and different gap ratios between the structures in tandem. The numerical setup will be validated to the published experimental data with respect to drag coefficient and flow profiles over a wall-mounted square.

1.2 Literature review

Many experimental and numerical studies have been carried out to investigate the flow around wall mounted structures at high Reynolds numbers. Arie et al. (1975) conducted experimental studies of the pressure distribution around square structures subjected to a turbulent boundary layer flow at Reynolds numbers $3.41 \times 10^4 < Re < 1.19 \times 10^5$. Tauqeer et al. (2017) conducted a numerical study for flows around subsea covers with different geometries subjected to different δ/D at $Re = 1 \times 10^6$. The study presented reasonable results compared to the experimental data (Arie et al., 1975) using the $k - \varepsilon$ turbulence model. Hydrodynamic quantities on wall-mounted structures with different geometries were also investigated. Meroney & Neff (2010) conducted validation studies on turbulence models for flows over wall-mounted panels. The study found that the $k - \omega$ turbulence model is sufficient to reproduce

consistent hydrodynamic quantities with the experimental data. Martinuzzi et al. (1993) investigated flow over square ribs with varying spanwise lengths W/D (W is the spanwise length of the rib structures and D is the height of the structures) using experiments. The study found that the flow around rib structures with W/D >10 can be considered as two-dimensional. Liu et al. (2008) studied the spatio-temporal characteristics of the separation and reattachment of turbulent flows over a two-dimensional square rib at $Re = 1.32 \times 10^4$ with δ/D = 0.75. Synchronized measurements of fluctuating pressure and velocity were obtained by using microphone arrays and a split-fiber film. The study showed that the shear layer separates from the leading edge of the rib, sweeps past the rib and reattaches on the bottom wall with a distance of $x_R = 9.75$ from the rib. Ryu et al. (2007) investigated the characteristics of turbulent channel flow over two-dimensional rib structures in tandem at $Re = 2 \times 10^4$ employing Reynolds Averaged Navier-Stokes Equations and the $k - \omega$ turbulence model. The structures in their study were square, triangular, semicircular and wavy wall (sinusoidal function shaped). It was found that the square shaped structure imposed the most resistance to the incoming flow while the wavy wall offered the least. The results were in good agreement with experimental data and the RANS $k - \omega$ turbulence model was found to capture the essential features of flow over wall-mounted structures.

The literature review shows that flow around wall-mounted structures has been studied in experiments for high Reynolds numbers and by RANS equations with the $k - \varepsilon$ and the $k - \omega$ turbulence models. To the authors knowledge, the hydrodynamic effects of varying trapezoidal configurations have not been studied using 2D RANS equations with $k - \omega$ SST turbulence model.

1.3 Outline

Chapter 2 presents the fundamental theories for wall-mounted structures under turbulent flow. This includes theory on flow over bluff and streamlined bodies, and an introduction to turbulence.

Chapter 3 gives an introduction to Computational Fluid Dynamics (CFD) and the software used in the present study. $k - \omega$ SST turbulence model and governing equations are explained in detail.

Chapter 4 describes the computational model and boundary conditions used throughout the study.

Chapter 5 presents the results of the single case simulations. The convergence and validation study are presented and discussed. The pressure contours, velocity profiles, streamlines and bed shear stress profiles are shown and discussed thoroughly for the single structure case.

Chapter 6 presents the results of the tandem case simulations. The convergence study is presented for the different gap ratios between the two structures. The pressure contours, velocity profiles and streamlines are shown and discussed in detail for the tandem case.

Chapter 7 gives the conclusions and outlines the main findings from Chapter 5 and Chapter 6. Possibilities for further work on the subject of flow over wall-mounted structures are also presented.

2 Theory

This chapter gives a brief theoretical introduction to the basic fluid dynamic principles and concepts which are relevant for studying wall-mounted structures in a turbulent boundary layer flow. The theory presented are flow concepts over bluff and streamlined bodies, turbulent flow and hydrodynamic coefficients.

2.1 Flow physics around immersed wall-mounted structures

The force exerted by a fluid flow on a submerged wall mounted body can be resolved along the normal and tangential directions to the body-surface. The force per unit area in the normal direction is the local pressure and the force per unit area in the tangential direction is the viscous stress. The pressure and viscous forces are dependent on the flow properties of the boundary layer flow which is characterized by the boundary layer thickness δ/D, free stream turbulence intensity, boundary layer profile and obstacle geometry. (Adams & Johnston, 1988).

The body shape of the structures decides how the velocity field and varying forces will work around them. Body shapes can be categorized into bluff and streamlined bodies. Bluff structures are defined as bodies where the major drag force contribution is due to the pressure forces arising from separation of the boundary layer flow adjacent to the surface over the rear end of the structures. Streamlined bodies are defined as bodies for which the major contribution to drag force in the freestream direction comes from the viscous friction (Cengel & Cimbala, 2017). A trapezoidal structure can be categorized as a bluff body due to its characteristic edges where turbulent separation often will take place. However, low angles of incident (or high α in the present case) will shape the trapezoid in a streamwise manner, and hence its characteristics too.

Bernoulli's principle explains the pressure and velocity interactions around the structure/structures discussed in Chapter 5 and Chapter 6. It states that an increase in fluid speed will transpire simultaneously with the decrease in pressure due to a reduction in the fluid's potential energy (Clancy, 1975). Bernoulli's principle can be derived from the principles of conservation of energy and Newtons second law which will be explained in Chapter 3.2.

Wall-mounted structures are often characterized by a large dominating vortex in its wake which is generated by smaller eddies. Since there are no vortex shedding, the present flow problem is assumed to be time independent and a steady state solution is likely to predict the flow field with high accuracy (Nymo, 2015).

2.2 Turbulence

2.2.1 Reynolds Number

The nondimensional Reynolds number is an important parameter when studying turbulent boundary layer flow around immersed bodies. It is denoted as the ratio between inertia forces and viscous forces and defined as

$$Re = \frac{Inertia\ Force}{Viscous\ Force} = \frac{U_\infty D}{\nu} \tag{2.1}$$

Here U_∞ is the free stream velocity, D is the characteristic length scale over the structure and ν is the kinematic viscosity of the fluid (Cengel & Cimbala, 2017). The characteristic length scale in the present study is the height of the structure D.

The flow in the present study is incompressible, meaning the fluid density ρ is constant due to negligible compressibility effects. Incompressible flow is valid for Mach number $Ma \leq 0.3$ where the Mach number is the ratio between speed of flow and speed of sound. This ratio is essential for aerodynamic behaviors but is negligible in subsea environment.

2.2.2 Laminar and Turbulent flow

Fluid flow can be categorized as either laminar or turbulent depending on low or high Reynolds numbers, respectively. Laminar flow can be characterized as streamlined flow patterns while the turbulent flow is unpredictable and chaotic as shown in Figure 2.1.

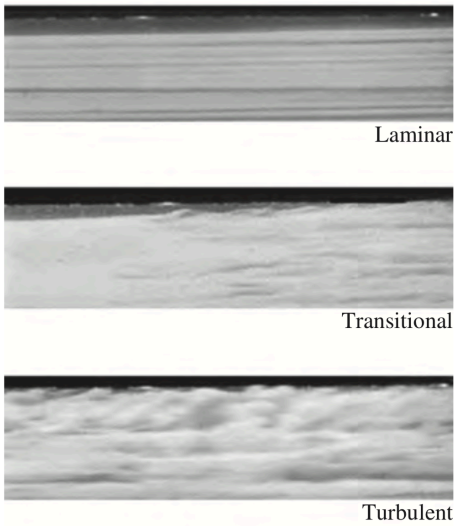

The transition between laminar and turbulent flow occurs after passing the critical Re. This transition point will however change with respect to the boundary conditions of flow problem. The turbulent flow has small horizontal velocity fluctuations $u'(t)$ around the mean velocity U as presented in Figure 2.2. These fluctuations are caused by small eddies and stochastic behavior of turbulent flow (Versteeg & Malalasekera, 2007).

Figure 2.2 Instantaneous turbulent velocity variations with respect to time (Versteeg & Malalasekera, 2007)

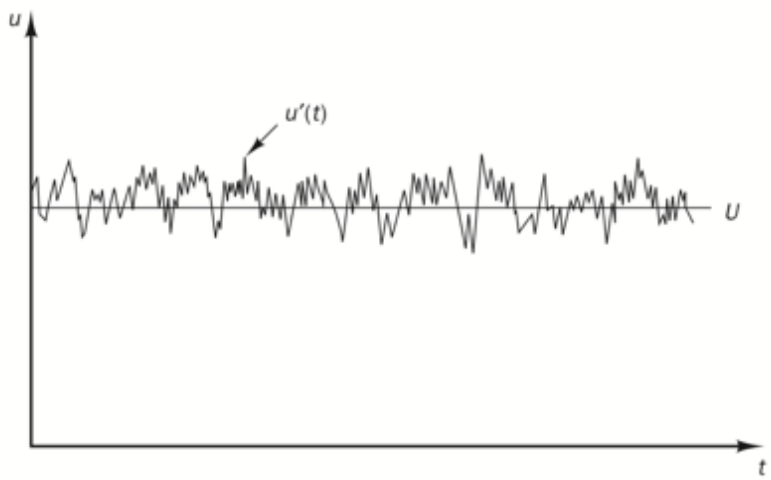

The total horizontal velocity $u(t)$ at a particular instance of time can be expressed as:

$$u(t) = u'(t) + U \qquad 2.2$$

In order to get a steady state solution for a turbulent flow, the Reynolds Averaged Navier-Stokes (RANS) equations needs to be solved. In RANS, flow properties like the velocity u and pressure p are expressed by their time-averaged as in Equation 2.2 and will be elaborated from the governing equations for CFD in Chapter 3.4.

The flow around any objects will have a 3D spatial character, even for 2D flow fields. These 3D flow effects are however small and negligible for boundary layer flows over wall-mounted rib structures (Martinuzzi & Tropea, 1993; Keshmiri, 2012), which is in the scope of the present study.

Turbulent flow is recognized by turbulent eddies which varies in a broad range of length scales. The larger eddies have velocity and length in the same order as U_∞ and D, respectively. The eddies are mainly developed by inertia forces and small viscous effects, and also contributing to the total shear stress on the fluid layers. The smaller eddies tend to be stretched by the motion of the large eddies, which results in kinetic energy being handed down from large eddies to progressively smaller eddies. When the eddies reach a length scale of 0.1 to 0.01 millimeters in engineering flow, the eddy motions are dissipated and converted into thermal internal energy. (Versteeg & Malalasekera, 2007)

2.2.3 Boundary Layer

For high Re flows, the boundary layer will be developed into a turbulent flow. Figure 2.3 shows how the turbulent boundary layer over a flat plate permutes from a laminar state to a turbulent state with characterized by swirling eddies. The no-slip condition assumes that the fluid layer adjacent to the wall has zero velocity relative to the boundary. This interaction creates negative shear stresses along the buffer layer and resolves into turbulent flow for the upper layers.

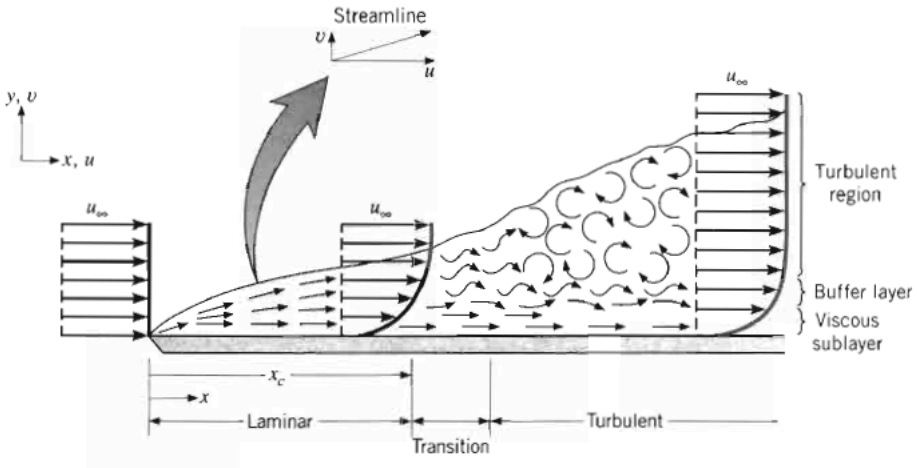

Expressions for the velocity profiles in boundary layer flows are based on extensive analysis and measurements (Versteeg & Malalasekera, 2007). The properties of the different layers can be expressed by the ratio between velocity and shear velocity u^+ and non-dimensional vertical distance from the wall y^+, which are given as

$$u^+ = \frac{U}{u_\tau} \qquad 2.3$$

and

Figure 2.3 Turbulent flow over a flat plate (Fundamentals of Heat and moment transfer, 8th edition)

$$y^+ = \frac{\rho y u_\tau}{\mu} \qquad 2.4$$

where y is the vertical distance which varies normal from the wall, u_τ is the shear flow velocity between the flow stream layers given by $u_\tau = \sqrt{\frac{\tau}{\rho}}$ where τ is the wall shear stress.

The first layer over the wall is the viscous sub layer shown in Figure 2.3. This is a laminar boundary layer dominated by viscous stresses. It is also referred to as the wall sublayer and dominates 1% of the total boundary layer thickness which corresponds to $y^+ \leq 5$ (Cengel & Cimbala, 2017). The viscous sub layer follows a linear relationship between u^+ and y^+ for smooth walls given by:

$$u^+ = y^+ \qquad 2.5$$

Above the viscous sub layer is the buffer layer, where the turbulence effects become relevant in addition to the viscous stresses. This layer is difficult to properly model since it inhabits flow characteristics from its adjacent layers seen in Figure 2.4. The upper layer is called the log-law layer which is dominated by turbulent stresses and is valid for $30 < y^+ < 500$. In this region, the shear stress changes gradually with respect to the normal distance to the wall. The log law can be expressed as:

$$u^+ = \frac{1}{\kappa}\ln(Ey^+) \qquad 2.6$$

where the von Kàrmàn constant $\kappa = 0.41$ and the log-law constant $E = 9.8$ in the employed simulation program OpenFOAM for smooth walls. Figure 2.4 shows how the plotted lines of experimental data corresponds to the two wall laws from equation 2.5 and 2.6.

Figure 2.4 Boundary layer regions (Tauqeer, 2016)

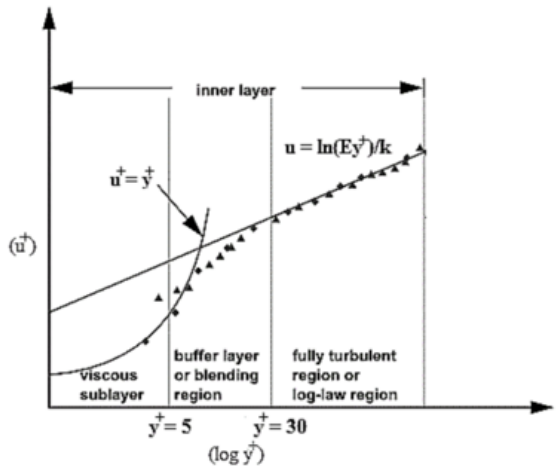

The proceeding boundary layer is the outer layer, also called law of the wake, which is fully dominated by inertia effects while viscous effects are negligible. In contrast to the transition region between the previously discussed wall functions from Equation 2.5 and 2.6, the log law and the law of the wake have the similar values in the point of transition. This non-dimensional velocity profile is expressed:

$$\frac{U_\infty - U}{u_\tau} = \frac{1}{\kappa}\ln\left(\frac{y}{\delta}\right) + c \qquad 2.7$$

where c is a constant. (Coles, 1956)

2.3 Hydrodynamic Coefficients

The pressure force, working normal on the obstacle surface, and shear forces, working tangential to the obstacle surface can describe the drag and lift force as:

$$F_D = \int_0^A -p\cos(\theta_n) + \tau_w \sin\ (\theta_n))\, dA \qquad 2.8$$

$$F_L = \int_0^A p\cos(\theta_n) - \tau_w \sin\ (\theta_n))\, dA \qquad 2.9$$

where dA is the differential area the force is working on and θ_n is the angle which the force works normal on the plane dA.

The drag and lift force over a body subjected to flow are often expressed using force coefficients. This is convenient because the coefficients can describe the non-dimensional properties of a specific shape, which can be utilized for other dimensions for the same shape. Moreover, the non-dimensional coefficients provide a common ground for comparing results to other investigations with identical flow conditions. The drag and lift coefficients can be expressed as

$$C_D = \frac{F_D}{\frac{1}{2}\rho U_\infty^2 A} \qquad 2.10$$

$$C_L = \frac{F_L}{\frac{1}{2}\rho U_\infty^2 A} \qquad 2.11$$

Here A is the front area of the projected body (Cengel & Cimbala, 2017).

3 Computational Fluid Dynamics

Computational fluid dynamics (CFD) is a computational tool using numerical analysis, data structures and computer computation to solve problems in fluid dynamics. The majority of CFD problems are boundary value problems solved through Navier-Stokes equations using Finite volume method (FVM). CFD is used in many applications and has become a widely used tool for predicting flow behavior in academic and industrial applications due to its low cost and reasonable accuracy. This chapter will briefly describe OpenFOAM, governing equations, FVM and the solver used for the present study.

3.1 OpenFOAM

OpenFOAM is a free, Linux based, open source software package designed to solve problems in continuum mechanics like CFD. The software is organized through a set of applications and libraries and is operated through text files and terminal commands. An OpenFOAM simulation case consists of various directories containing information about the flow problem as shown with an example from the present study in Figure 3.1.

Figure 3.1 Organized OpenFOAM folders for the present study

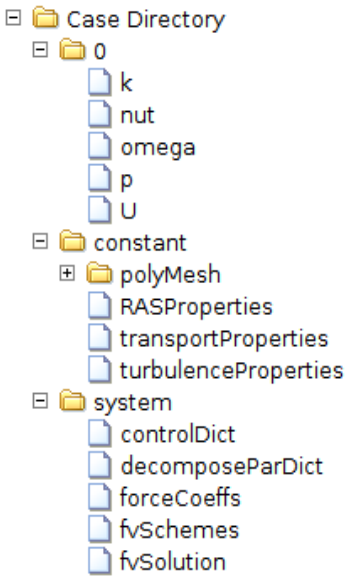

The 0 directory contains text files which defines the boundary conditions of the flow properties characterizing the boundary problem. The constant folder holds the files with information of the mesh and the physical boundaries of the simulation. The system folder contains files regarding the solver schemes and simulation options.

3.1.1 Meshing and Pre-Processing

First step in constructing an OpenFOAM case is to define the geometry of the boundary problem and partition it to discrete cells. The partitioned domain is called a mesh or a grid, and its interface is crucial for the accuracy of the numerical simulation. Areas with the largest velocity and pressure gradients requires the smallest cells to thoroughly capture the critical areas in the boundary layers, often located close to the walls. It is also necessary to avoid abrupt changes in mesh density since OpenFOAM solves the flow problem spatially with finite volume methods. The mesh generating software used in the present study is GMSH due to its mesh generating tools, scripting options and OpenFOAM support.

3.1.2 Solving

OpenFOAM solves the Navier-Stokes equations over a space using the finite volume methods (FVM). Spatial schemes for gradient, Laplacian and divergence used in the present study are Gauss linear, bounded Gauss linear upwind, and Gauss linear limited corrected, respectively. The solver is steady state, which means that the flow problem characteristics do not change with time. If the simulation is found to have trouble converging, it may indicate that the solution is transient. At every time step, the initial solution from the integration is improved with the SteadyState solver which uses a looped algorithm to iterate the solution until the Navier-Stokes equations are satisfied for the user, further explained in Chapter 3.4.

3.1.3 Courant number

The Courant number is a condition for stability when solving partial differential equations with finite difference methods in time. The Courant Friedrichs Lewy (CFL) condition is defined as

$$CFL = \frac{u\Delta t}{\Delta x} \leq CFL_{max} \qquad 3.1$$

Here u is the local velocity inside a mesh cell, Δt is the assigned time step and Δx is the cell length in x-direction (Sanz-Serna, 1989). For example, if CFL > 1, a fluid particle will travel further than the length of the cell during the time-step. The simulation may produce inaccurate results if this condition is not met, hence the present study has specified $CFL_{max} < 1$.

3.1.4 Post- processing

OpenFOAM has various post processing utilities and there are numerous software packages to analyze the output from a simulation. In the present study, ParaView is used to extract data values from areas of interest in the computational domain which is further processed into graphs and tables using Matlab 2018b. Techplot360 is used to draw streamlines and create contour plots of pressure and velocity.

3.2 Governing Equations

3.2.1 Mass and momentum conservation

The governing equations for any incompressible and isothermal fluid flow are the continuity equations and the momentum equations, which are known as the Navier-Stokes equations. The continuity equations describe the conservation of mass and the momentum equations are based of Newtons second law and the equations are respectively given as:

$$\frac{\partial u_i}{\partial x_i} = 0 \tag{3.2}$$

$$\frac{\partial u_i}{\partial t} + u_j \frac{\partial u_i}{\partial x_j} = -\frac{1}{\rho}\frac{\partial p}{\partial x_i} + \nu \frac{\partial^2 u_i}{\partial x_j^2} \tag{3.3}$$

where $i, j = 1,2$ (for x, y) denote the streamwise and cross-stream directions, respectively; u_1 and u_2 (for u and v) are the corresponding mean velocity components. p is the pressure and ρ is the fluid density.

3.2.2 Reynolds-Averaged Navier Stokes RANS

The Reynolds-averaged Navier-Stokes (RANS) are Reynolds averaged equations for turbulent flow. In an economical point of view RANS is preferred over Direct Numerical Simulation

(DNS) and Large Eddy Simulation (LES) due to computational cost as well as giving reasonable accuracy. RANS implement Reynolds decomposition to the original Navier-Stokes equations to represent the fluctuating velocity terms from Equation 2.2. And then, the RANS equation can be given by (Wilcox, 2004):

$$\frac{\partial u_i}{\partial t} + u_j \frac{\partial u_i}{\partial x_j} = -\frac{1}{\rho}\frac{\partial p}{\partial x_i} + \nu \frac{\partial^2 u_i}{\partial x_j^2} - \frac{\partial \overline{u'_i u'_j}}{\partial x_j} \qquad 3.4$$

here $\overline{u'_i u'_j}$ is the Reynolds stress component. According to Boussinesq assumption, the turbulent eddies causing momentum transfer can be modeled as the effect of the eddy viscosity (Clement, 1998). The Reynolds stress component can be expressed as:

$$-\overline{u'_i u'_j} = \nu_t \left(\frac{\partial u_i}{\partial x_j} + \frac{\partial u_j}{\partial x_i} \right) - \frac{2}{3} k \delta_{ij} \qquad 3.5$$

where δ_{ij} is the Kronecker delta, k is the turbulent kinetic energy and ν_t is the turbulent viscosity. Kronecker delta is defined as:

$$\delta_{ij} = \begin{cases} 0 & if\ i \neq j \\ 1 & if\ i = j \end{cases} \qquad 3.6$$

To solve the resulting system of the Equations 3.4 and 3.5, additional assumptions of the turbulence quantities have to be made. Closure of Reynolds stress is obtained by using the $k - \omega$ SST turbulence model which is elaborated in the next chapter.

3.2.3 $k - \omega$ SST Turbulence Model

The $k - \omega$ SST turbulence model (Menter, 1994) is a two-equation eddy-viscosity model which is used in the present study due to its good performance in predictions of adverse pressure gradients and separating flow (Zhang, 2017). The $k - \omega$ SST turbulence model is a combination of the $k - \omega$ and the $k - \varepsilon$ model. The near wall region of the computational domain is treated with the $k - \omega$ model of Wilcox (1998) while the standard $k - \varepsilon$ model of

Jones & Launder (1973) is used in the outer wake region and in the free shear layers. According to Menter et al. (2003), the equations of k and ω can be expressed as follow:

$$\frac{D(\rho k)}{Dt} = \widetilde{P_k} - \beta^* \rho \omega k + \frac{\partial}{\partial x_j}\left[(\mu + \sigma_k \mu_t)\frac{\partial k}{\partial x_j}\right] \qquad 3.7$$

$$\frac{D(\rho \omega)}{Dt} = \alpha \rho S^2 - \beta \rho \omega^2 + \frac{\partial}{\partial x_j}\left[(\mu + \sigma_\omega \mu_t)\frac{\partial \omega}{\partial x_j}\right] + 2(1 - F_1)\rho \sigma_{\omega 2}\frac{\partial k}{\partial x_j}\frac{\partial \omega}{\partial x_j} \qquad 3.8$$

where $\widetilde{P_k}$ is expressed by

$$\widetilde{P_k} = min\left[\mu_t \frac{\partial u_i}{\partial x_j}\left(\frac{\partial u_i}{\partial x_j} + \frac{\partial u_j}{\partial x_i}\right), 10\beta^* \rho \omega k\right] \qquad 3.9$$

Φ_1 represents any constant in the original $k - \omega$ model (σ_{k1}, …) and Φ_2 represents any constant in the original $k - \varepsilon$ model (σ_{k2}, ...). Then the constant Φ of the new model is denoted as

$$\Phi = F_1 \Phi_1 + (1 - F_1)\Phi_2 \qquad 3.10$$

$$F_1 = tan\,h(arg_1^4) \qquad 3.11$$

$$arg_1 = min\left[\max\left(\frac{\sqrt{k}}{\beta^* \omega y}, \frac{500\nu}{y^2 \omega}\right)\frac{4\rho \sigma_{\omega 2} k}{CD_{k\omega} y^2}\right] \qquad 3.12$$

$$CD_{k\omega} = ma\,x\left(2\rho \sigma_\omega \frac{1}{\omega}\frac{\partial k}{\partial x_j}\frac{\partial \omega}{\partial x_j}, 10^{-10}\right) \qquad 3.13$$

here y is the distance to the closest wall. $CD_{k\omega}$ is the positive portion of the cross-diffusion term in Equation 3.8.

The turbulent eddy viscosity is defined as

$$\nu_t = \frac{a_1 k}{max(a_1 \omega, SF_2)} \qquad 3.14$$

Here S is the invariant measure of the strain rate and F_2 is

$$F_2 = tanh(arg_2^2) \tag{3.15}$$

$$arg_2 = max\left(2\frac{\sqrt{k}}{0.09\omega y}, \frac{500\nu}{y^2\omega}\right) \tag{3.16}$$

The SST constants are: $\beta^* = 0.09$, $\alpha_1 = 0.5532$, $\alpha_2 = 0.4403$, $\beta_1 = 0.075$, $\beta_1 = 0.0828$, σ_{k2}= 1.0 and $\sigma_{\omega 1}$= 0.5, $\sigma_{\omega 2}$ = 0.85616.

3.3 Finite Volume Method

OpenFOAM is based on the finite volume method (FVM) which directly applies the conservation laws, using the integral formulation of the governing RANS equations from Chapter 3.2. The finite volume method discretizes the governing equations by partitioning the physical domain into discrete cells/control volumes. Furthermore, the volume integrals over these cells can be converted into a surface integral at the cell boundaries using Gauss theorem. Subsequently, the integrals are turned from integrating the differential of the dependent variable inside of the cells to surface integrals of the flux dependent on the variables across the cell boundary. This simplification allows for iterative solvers to compute the flow domain. (Versteeg & Malalasekera, 2007)

3.4 simpleFoam

The simulations in the present study applies the steady-state solver for incompressible, turbulent flow, using the SIMPLEC (Semi-Implicit Method for Pressure Linked Equations Consistent) algorithm-based solver, simpleFoam. The algorithm uses standard pressure-velocity coupling and the flow chart is presented in Figure 3.2. The solution strategy is to find a steady-state solution with the aid of under-relaxation factors between iterations (Jasak, 1996).

Figure 3.2 Flow chart of the SIMPLE algorithm

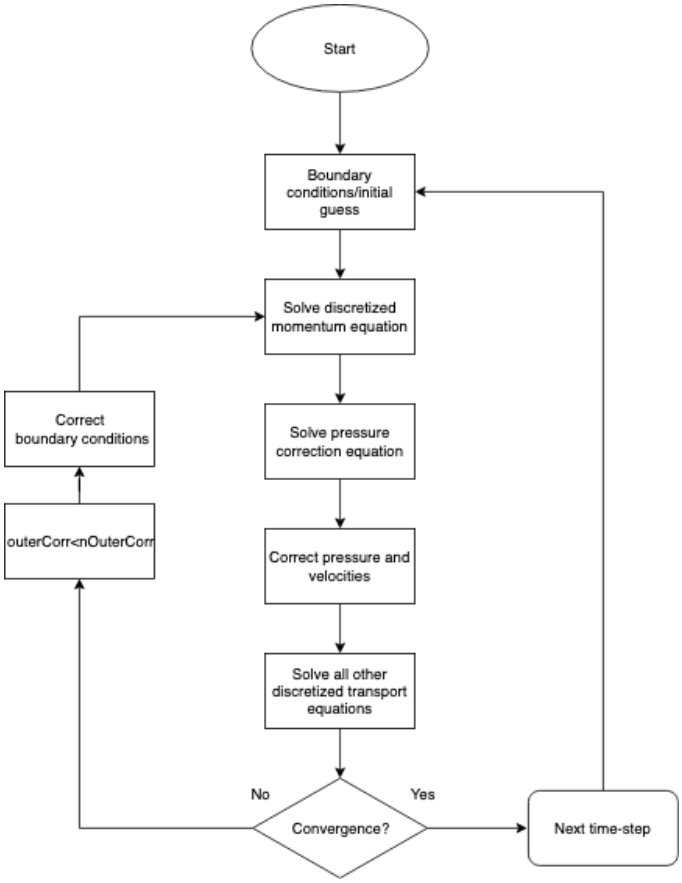

nOutercorr is the number of outer corrector loops set for one time-step. The outer corrector rewrites the boundary conditions with the solved equations of pressure, velocity and transport. The simulation will go over to the next time-step if outerCorr surpasses the iteration-count given by nOuterCorr (Robertson et al.,2015).

4 Computational model

Descriptions for the computational models of squares and trapezoids in single and tandem configurations are presented in this chapter. The boundary conditions concerning the present simulations are also outlined.

4.1 Model description

Figure 4.1 and Figure 4.2 presents the 2D computational domain used in the present study for the single structure case and the tandem case, respectively. The origin of the coordinates is located at the bottom center of the wall mounted structure. The height and top lengths of the structure is D and the bottom angels of the trapezoidal structures are $90° - \alpha = 90°(\text{square}), 75°, 60°, 45°$and $30°$. The length and height of the computational domain are $52D$ and $20D$, respectively. The flow inlet boundary is located Lu upstream from the center of the structure and the flow outlet boundary is located Ld downstream from the center of the structure. Ong et al. (2010) performed a numerical study of flow around circular cylinder close to a flat seabed at the same Reynolds number range as the present study and found that a computational domain with $(Lu, Ld) = (10D, 20D)$ is sufficient to suppress any far-field effects on the structures. In the present study, Lu is set to be $11.5D$ and Ld is set to be $40.5D$

Figure 4.1 Computational domain and boundary conditions for single structure case

to ensure that the domain is large enough and to capture the motions of interest.

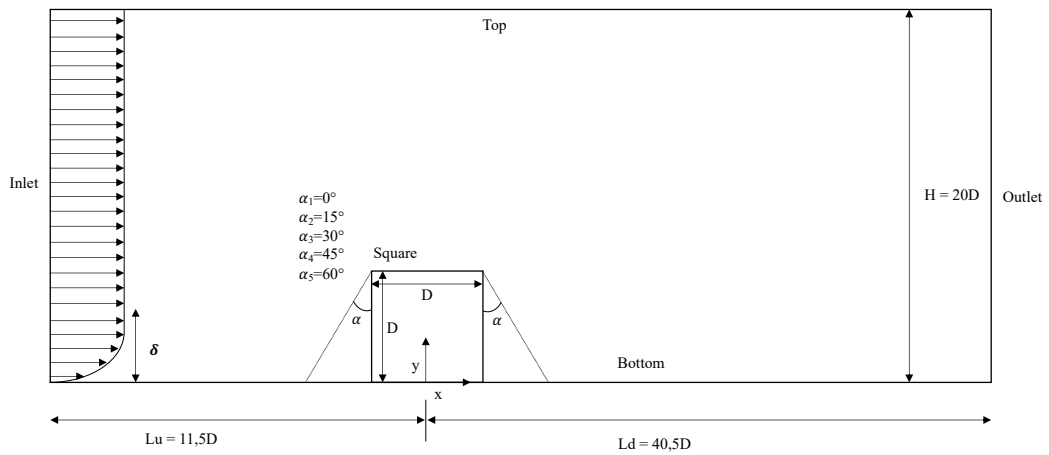

The tandem case investigates identical cover shapes in tandem where the gap ratio G/D is the distance in between Square 1 and Square 2, presented in Figure 4.2. The G/D investigated are $2, 3\ 6, 10$ and 14 for the square configuration and $G/D = 6, 10$ and 14 for all trapezoidal structures. The maximum downstream length from Square 2 to the outlet is $40.5D - 14D = 26.5D$ which is sufficient in terms of far field effects.

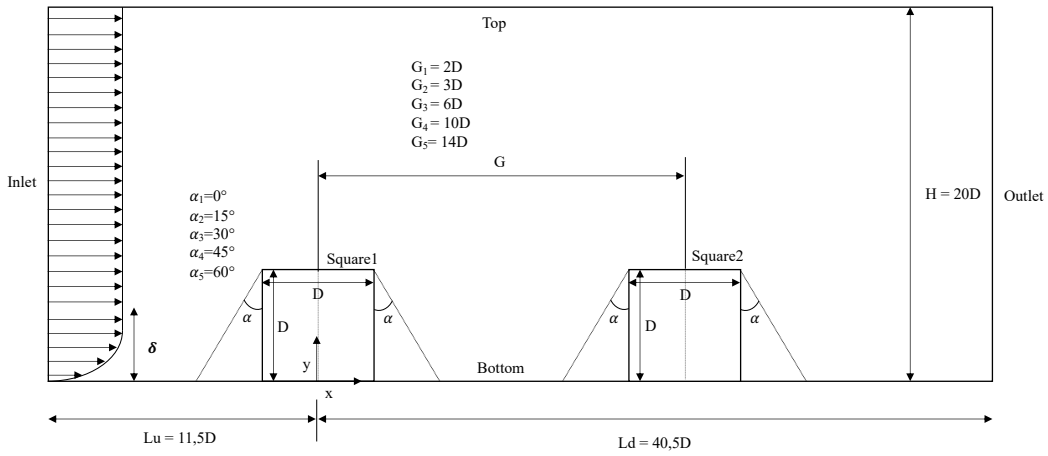

Figure 4.2 Computational domain and boundary conditions for tandem case

4.2 Boundary Conditions

The boundary conditions are based on previous experiments done by Arie et al (1975). The Reynolds numbers studied for the single cases are 1.19×10^5 and 1.0×10^6 and are meant to cover a typical range for subsea environmental conditions. The tandem case was investigated at $Re = 1.19 \times 10^5$.

4.2.1 Inlet

The inlet velocity is a logarithmic boundary layer flow, with a horizontal velocity profile, adapted from the experiments done by Arie et al (1975) to ensure similarity to the experimental set up for validation study in Chapter 5.2 . The velocity profile is used throughout the study and given by

$$u = min\{u^{*}\left(c_1 * \log\left(\frac{y}{\delta}\right) + c_2\right), U_\infty\} \quad 4.1$$

Here u^* is the bottom wall friction velocity, c_1 and c_2 are the constants from the velocity profile adaptation found to be 0.1006 and 0.9656, respectively, by using curve fitting functions in Matlab2018.

The velocity in y direction is set to be zero and the value of k and ω is calculated as follows:

$$k(y) = max\left\{C_\mu^{\frac{-1}{2}}\left(1 - \frac{y}{\delta}\right) \times \left|1 - \frac{y}{\delta}\right| u^{*2}, 0.0001U_\infty^2\right\} \quad 4.2$$

$$\omega = \frac{k^{0.5}}{C_\mu^{0.5} l} \quad 4.3$$

$$l = min\left\{\kappa y\left(1 + 3.5\frac{y}{\delta}\right)^{-1}, C_\mu \delta\right\} \quad 4.4$$

where $C_\mu = 0.09$ is the turbulent-viscosity constant, $\kappa = 0.41$ is the Karman constant and l is the turbulent length scale (see e.g Brørs, 1999; Ong et al., 2010).

4.2.2 Walls: Bottom and Structures

No-slip condition ($u_1 = u_2 = 0$) and standard near-wall conditions are used. When using these wall functions, the criteria of $y^+ > 30$ from Equation 2.4 must be satisfied.

4.2.3 Outlet, Top and Front & Back

At the outlet, u_1, u_2, k and ω are specified as zero gradient and the pressure is set as zero. At the top, u_1, u_2, k and ω are set as zero gradient. The front & back patches are specified as empty for u_1, u_2, k and ω since the problem is two dimensional.

4.3 Computational mesh

The computational meshes used for the present study are shown in **Error! Reference source not found.** and **Error! Reference source not found.** for the single and tandem set up, respectively. The grids in the present study are constructed as structured mesh with quadrilateral cell shapes. Structured mesh is used due to its convergence advantages and higher resolution as well as being applicable to for the present geometry.

a) b)

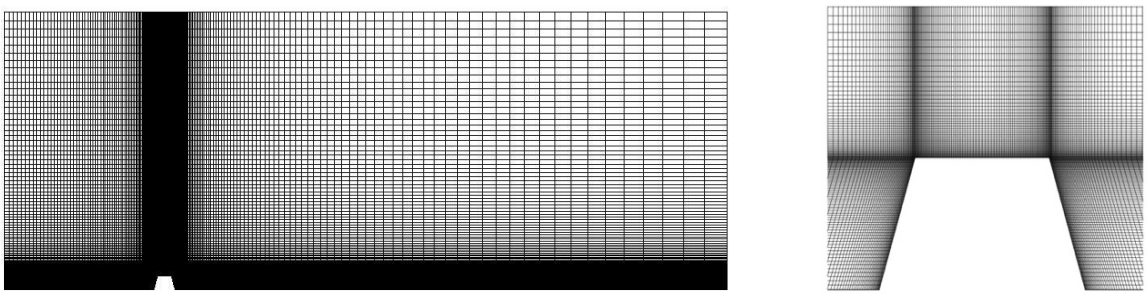

a) b)

F

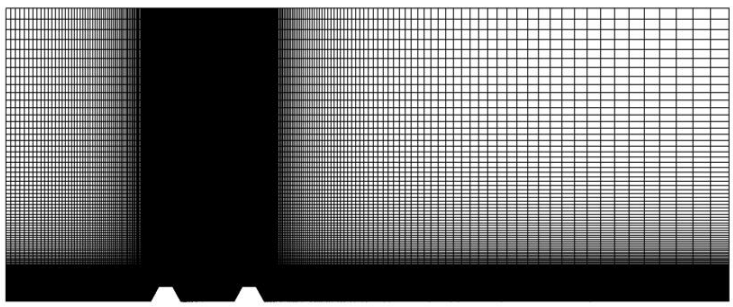

10^5

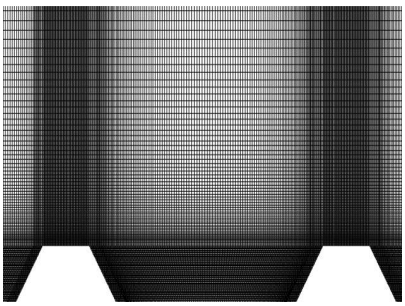

To ensure the validity of using wall functions the first height of the first cell layer Δy for the walls was $0.025D$ and $0.0041D$ for $Re = 1.19 \times 10^5$ and $Re = 1.0 \times 10^6$, respectively. These lengths were found to satisfy the averaged $30 \leq y^+ \leq 42$ for all α configurations for the single case. For the tandem case, the Δy at all walls, including the second structure was $0.027D$ for all configurations to maintain $30 \leq y^+ \leq 42$. The cell size is refined in the high gradient regions while coarser grids are used in the far field regions to reduce computational cost.

5 Results and Discussion for Single Case

This section presents and discusses the results for the single structure case. Chapter 6 will discuss the results for the tandem case. Table 5.1 and 5.2 shows the results of for all single structure cases at $Re = 1.19 \times 10^5$ and $Re = 1.0 \times 10^6$, respectively.

Mesh	α [°]	C_D	C_L	x_R/D
19076	0	1.030	0.604	15.27
30424	0	1.021	0.608	15.39
46531	0	1.001	0.595	15.05
26 800	15	0.991	0.487	14.82
36166	15	0.988	0.486	14.88
48789	15	0.984	0.487	15.01
26 800	30	0.943	0.411	14.36
36166	30	0.940	0.411	14.41
48789	30	0.937	0.413	14.62
26 800	45	0.851	0.367	13.36
36166	45	0.846	0.368	13.40
48789	45	0.844	0.369	13.48
26 800	60	0.677	0.362	11.57
36166	60	0.673	0.363	11.88
48789	60	0.672	0.363	11.43

Table 5.1 Hydrodynamic quantities for varying α with different grids at $Re = 1.19 \times 10^5$

Mesh	α [°]	C_D	C_L	x_R/D
39 360	0	1.115	0.624	16.90
53 124	0	1.125	0.657	16.83
85 824	0	1.113	0.655	16.10
39 360	15	1.070	0.488	16.52
56 124	15	1.060	0.504	16.28
98 244	15	1.059	0.507	15.77
39 360	30	0.997	0.410	15.64
56 124	30	0.990	0.417	15.71
98 244	30	0.987	0.438	14.82
39 360	45	0.874	0.369	14.22
56 124	45	0.869	0.380	14.20
98 244	45	0.870	0.395	13.60
39 360	60	0.653	0.389	11.42
56 124	60	0.646	0.386	11.54
98 244	60	0.639	0.406	11.06

5.1 Convergence study

The grid resolution study has been carried out for all five angles ($\alpha = 0°, 15°, 30°, 45°$ and $60°$) at $Re = 1.19 \times 10^5$ and $Re = 1.0 \times 10^6$ for $\delta/D = 0.73$. The variations of C_D, C_L and x_R/D are obtained and presented in Table 5.1 and Table 5.2. C_D and C_L are calculated directly from F_D and F_L which are computed from the total force acting on the surface of the structures. x_R/D is the horizontal distance between the separation point at the top left corner of the structures and the point where the bottom wall shear stress changes its sign in the wake region. Results

for the convergence studies of $Re = 1.19 \times 10^5$ and $Re = 1.0 \times 10^6$ are also shown with variation of the grid numbers for C_D, C_L and x_R/D in Figure 5.1. Three meshes are generated for each unique configuration to ensure mesh independence for the quantities of C_D, C_L and x_R/D. The three mesh densities are categorized into coarse, normal and dense grid resolutions and increased with 50% to ensure sufficient spatial discretization.

a) b)

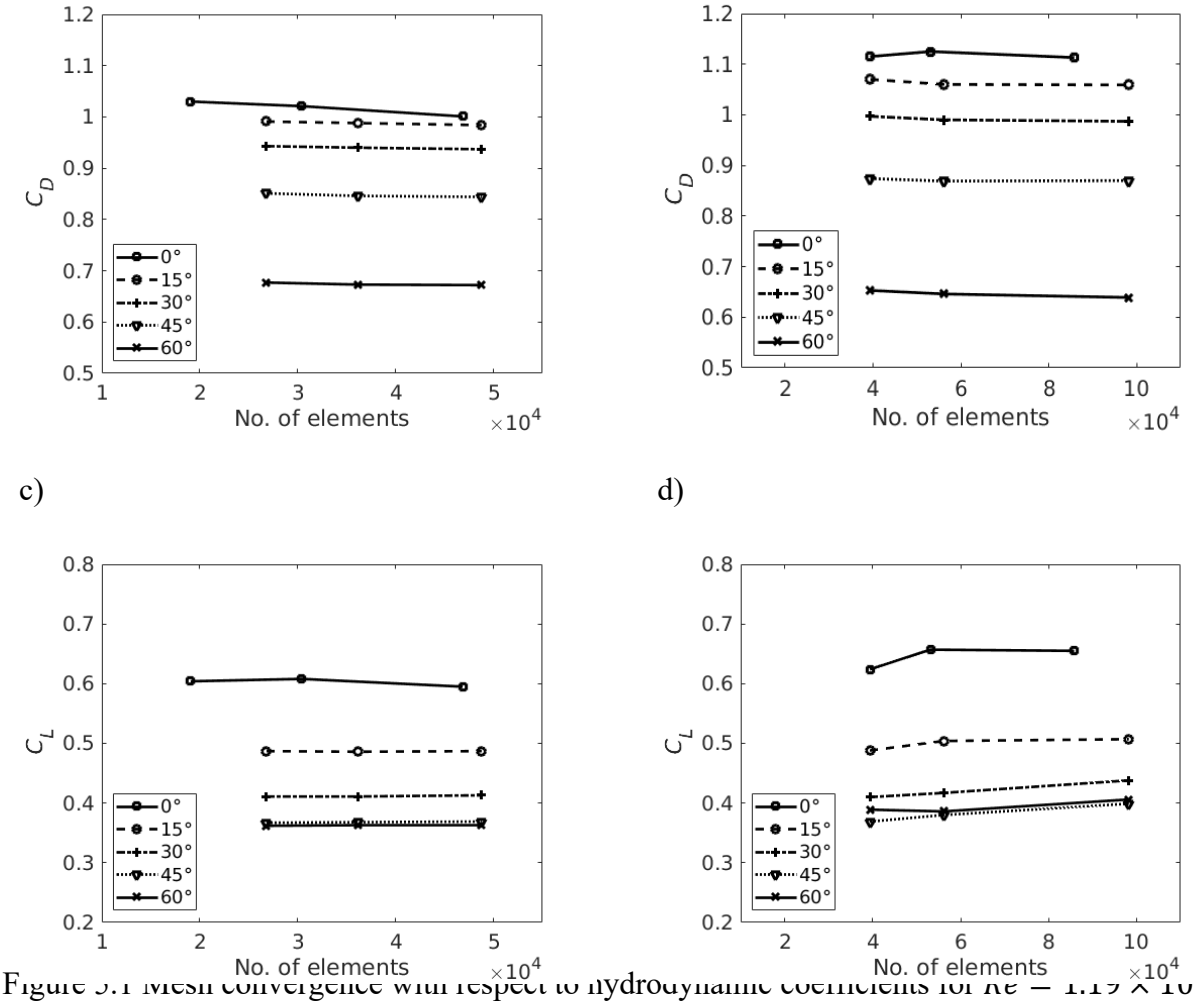

c) d)

Figure 5.1 Mesh convergence with respect to hydrodynamic coefficients for $Re = 1.19 \times 10^6$ (left side) and $Re = 1.0 \times 10^6$ (right side)

e) f)

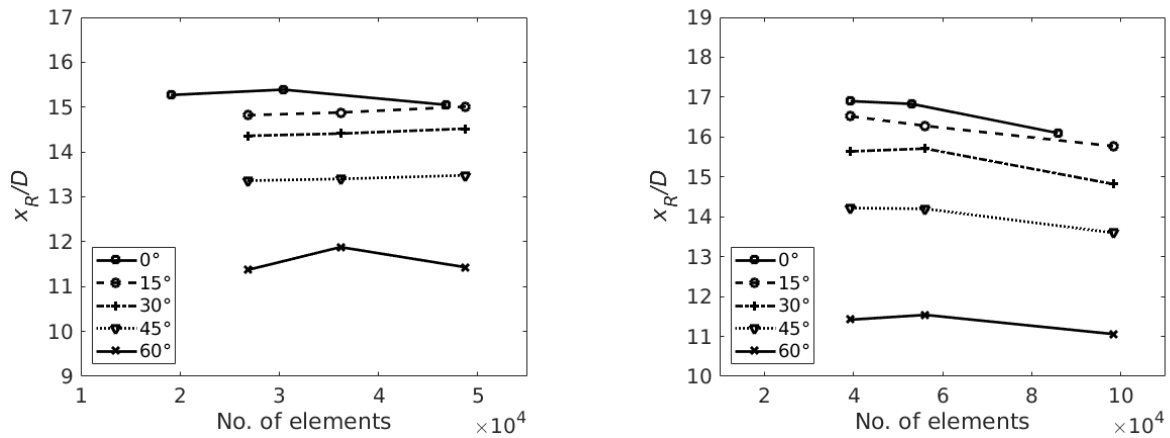

For different mesh densities at $Re = 1.19 \times 10^5$, the difference of C_D between the cases varies from 0.14% to 1.99%. The relative difference of C_L is from 0.16% to 2.18% and the relative difference of x_R/D varies from 0.59% to 2.23%. For different mesh densities at $Re = 1.0 \times 10^6$, the relative difference of C_D between cases alters between 0.09% and 1.09%. The relative difference of C_L varies between 0.3% and 4.86% and that for x_R/D alters between 3.24% and 6%. Therefore, the normal mesh densities for both square and trapezoid cases at the two Reynolds numbers have achieved sufficient grid resolutions.

Since wall functions are applied for all the simulations, a requirement of $y^+ > 30$ for the first grid above the wall needs to be satisfied. In the present study, y^+varies between 30 and 42 for different configurations at both Reynolds numbers. It can be concluded that grid resolutions for all configurations in the present study can provide satisfactory results.

5.2 Validation study

Validation study is done by comparing the drag coefficient and the horizontal velocity profiles of the present study with those of the earlier numerical and experimental studies. The drag coefficient was compared to the experimental data from Arie et al. (1975) and the numerical data from Tauqeer et al. (2017) using identical flow conditions of $\delta/D = 0.73$ at $Re = 1.19 \times 10^5$. The present study simulated $C_D = 1.00$, which is in good agreement with the previous results of $C_D = 0.96$ (Arie et al., 1975) and numerical data $C_D = 1.02$ (Tauqeer et al., 2017).

To further validate the simulation, a comparison of horizontal velocity profiles between the experimental data from Liu et al. (2008) and the present study has also been performed. The experiment of Liu et al. (2008) was conducted at $Re = 1.32 \times 10^4$ with $\delta/D = 0.75$;and it is compared to the present simulation at $Re = 1.19 \times 10^5$ with $\delta/D = 0.73$. The horizontal velocity profiles are compared at six different locations along the computational domain shown in Figure 5.2. The velocity profile at the upstream location of $x/D = -3.5$ shows no negative part and it appears to be the same as the experimental profile. The velocity profile at the separation point $x/D = -0.5$ also appears to follow the experimental data but has a slight overpredicted region in the upper section of the velocity profile. This overprediction is also observed for the other four downstream locations and this may be due to the difference in Reynolds number. Furthermore, the overprediction of the velocity profiles compared with Tauqeer et al. (2017), where the $k - \epsilon$ turbulence model is used, may be due to the low dissipation by using the $k - \omega$ SST model in the present study. A small negative region in the velocity profiles appears at $x/D = 0.5$ on the top right corner of the square which shows the presence of an adverse pressure gradient. There is a large negative region close to the bottom wall in the velocity profiles downstream the square indicating that a recirculation zone has been developed. In general, the profiles show reasonable agreement with the experimental data.

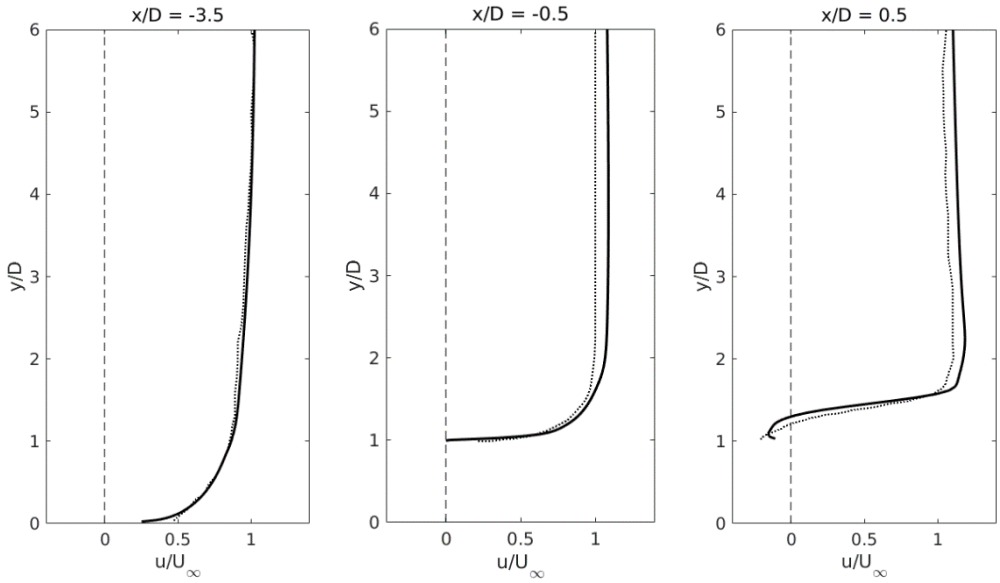

Figure 5.2 Comparisons of horizontal velocity profiles of the present simulation and experimental data from Liu et al. (2009)

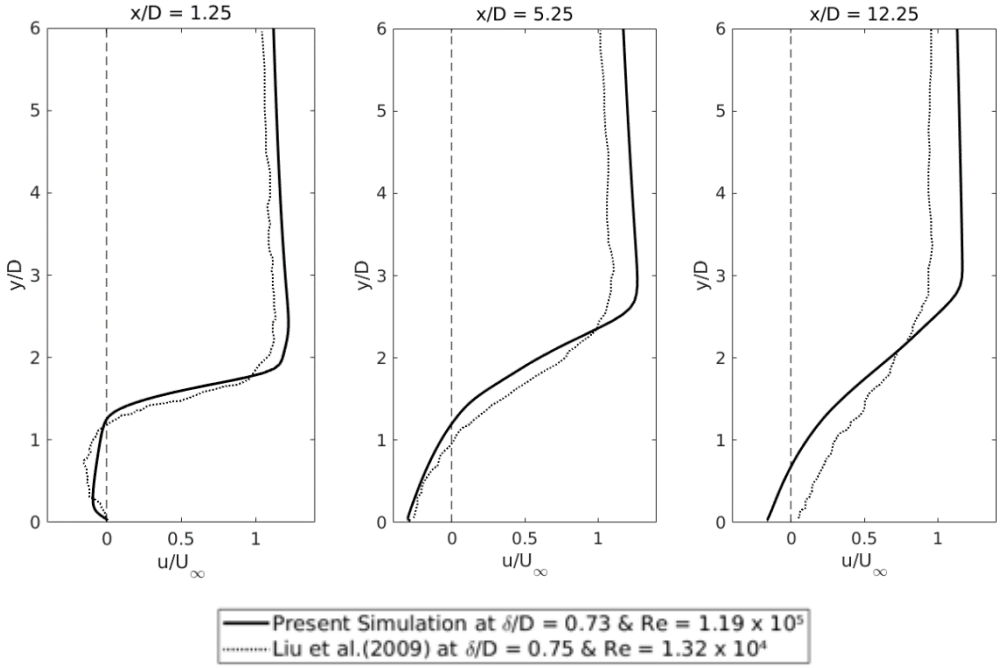

5.3 Effect of α on hydrodynamic quantities and x_R/D

The angles $0° < \alpha < 60°$ have been studied at $Re = 1.19 \times 10^5$ and $Re = 1.0 \times 10^6$ to examine its effects on the hydrodynamic quantities: C_D, C_L and x_R/D. As seen from Figure 5.3 (a), the drag coefficient is monotonically decreasing with increasing α. The physical explanation for the trend can be outlined as follows. The main contribution of the total drag is the pressure difference between the front and the back face of the structure. The block effect of structure becomes weak with increasing α, which results in less pressure difference. This can also be observed in the pressure distribution in Figure 5.4. However, as α further increases, the contribution of the viscous drag increases and with $\alpha = 60°$ the trapezoid tends to be flat and a larger part of the total drag on the structures comes from the viscous drag.

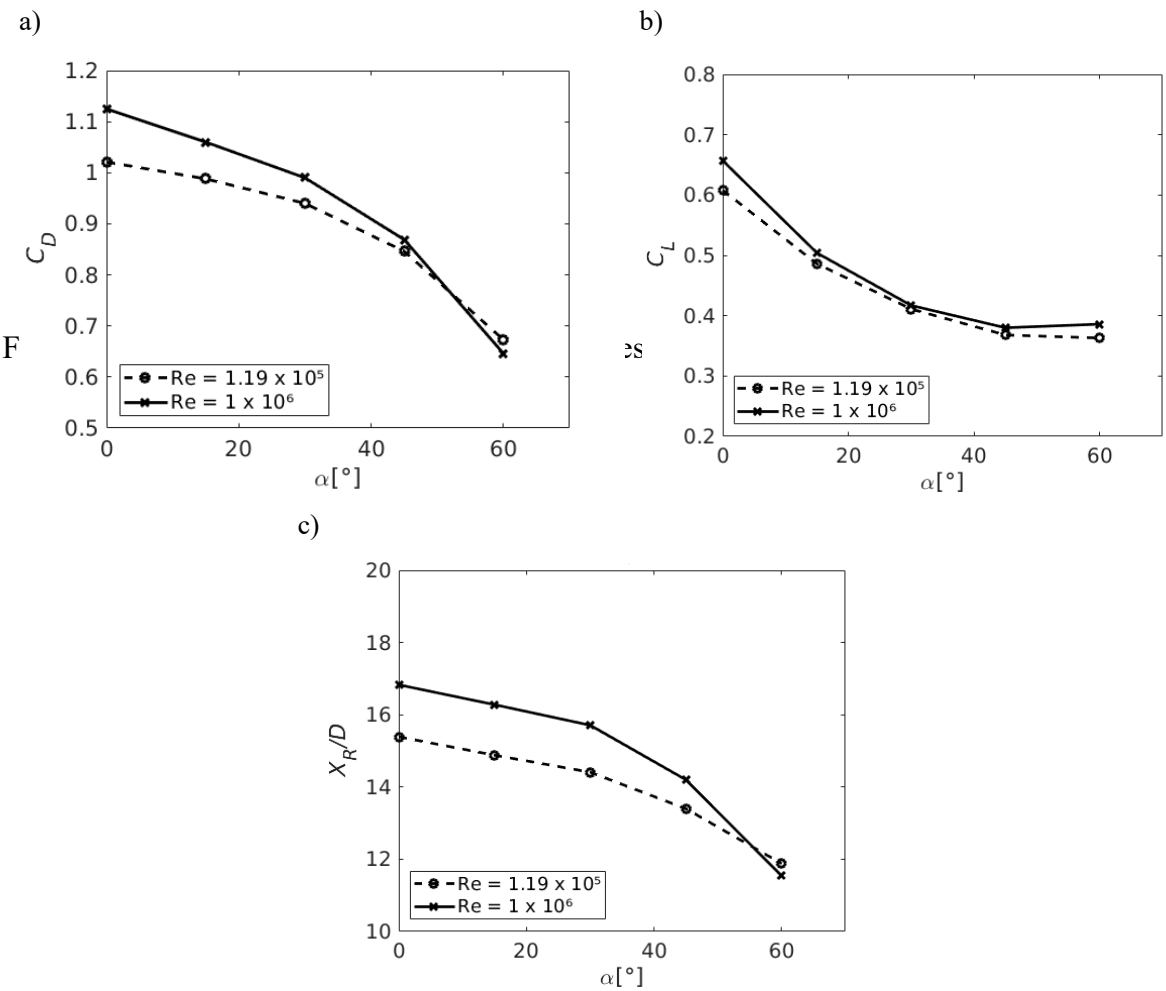

The viscous drag is higher at $Re = 1.19 \times 10^5$ and causes larger C_D than that at $Re = 1.0 \times 10^6$ for higher α as shown in Figure 5.3.1 (a). The recirculation length x_R/D, shown in Figure 5.3 (c), also decreases for increasing α and behaves similar to C_D. This implies that the

viscous effect has a significant influence on these two quantities when the pressure contribution decreases.

5.4 Velocity and Pressure Distributions

The color contours of the pressure at $Re = 1 \times 10^6$ are presented in Figure 5.4. The pressure contour values seen in Figure 5.4 (a) represents the kinematic pressure $P = p/\rho_0$, where ρ_0 is the constant mass density. Due to the block effect of the structures to the flow, there is a high-pressure region in front of the structure because of the energy conservation. Furthermore, due to the conservation of mass, a high-speed velocity region forms after the separation point above the structure. Hence, due to the Bernoulli's principle, the high-speed velocity region creates a local negative pressure region around the right top edge of the structure as seen in Figure 5.4. It can be observed that the intensities of both the positive and negative pressure regions reduces with increasing α. This is due to the fact that the reducing blocking effect, associated with higher α, causes lower velocity drop over the structure, hence resulting in weaken pressure regions due to the Bernoulli's principle.

a) b)

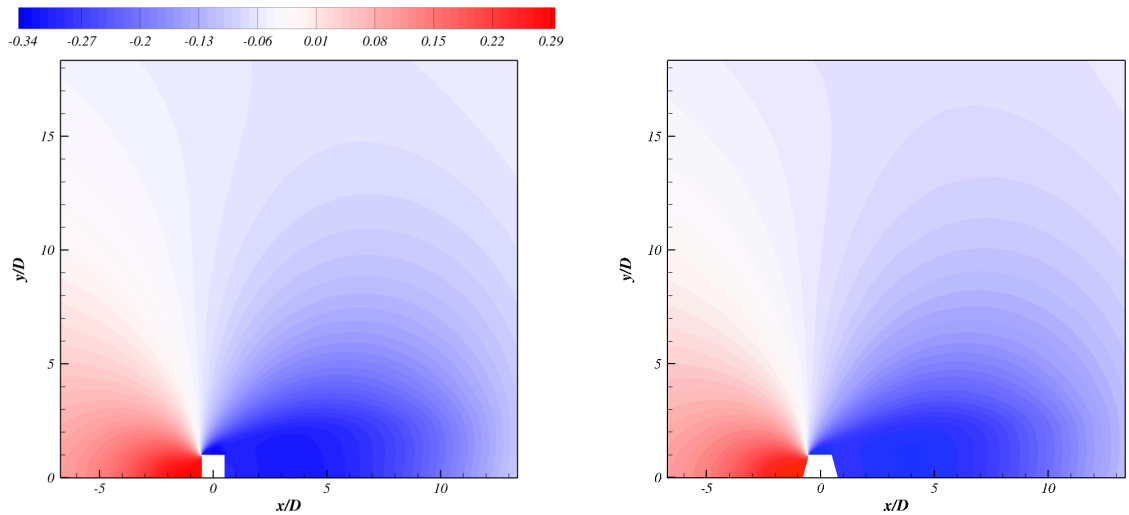

c) d)

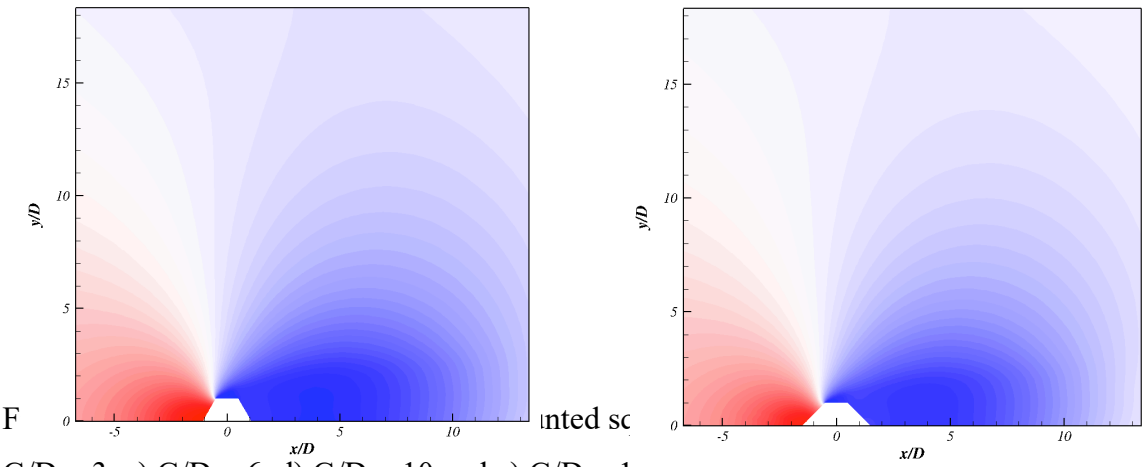

F nted sc D = 2, b) G/D = 3, c) G/D = 6, d) G/D = 10 and e) G/D = 14

e)

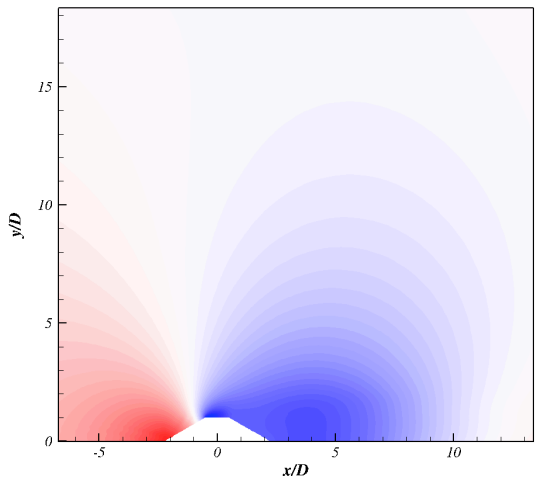

The contours of the horizontal velocities at $Re = 1 \times 10^6$ are presented in Figure 5.5 for all α. The velocity at the front face of the structure is zero and propagates further upstream due to the blocking effect. After the separation point at the top left corner of the structure, the velocity is accelerated due to the conservation of mass. A shear layer is generated with a high-speed region above the structure and a recirculation region behind the structure. The area of the high-speed region reduces with decreasing α. The negative velocity region downstream close to the bottom wall implies that recirculation takes place.

a)

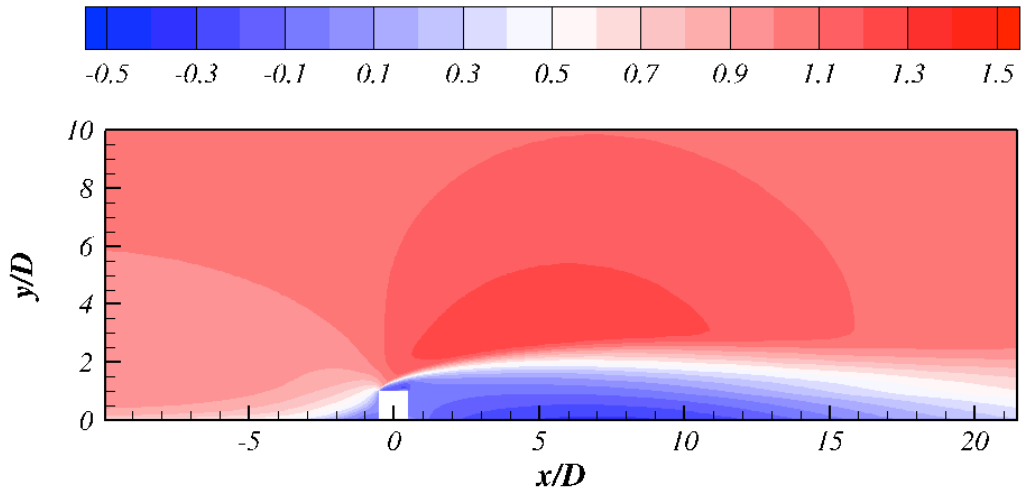

b)

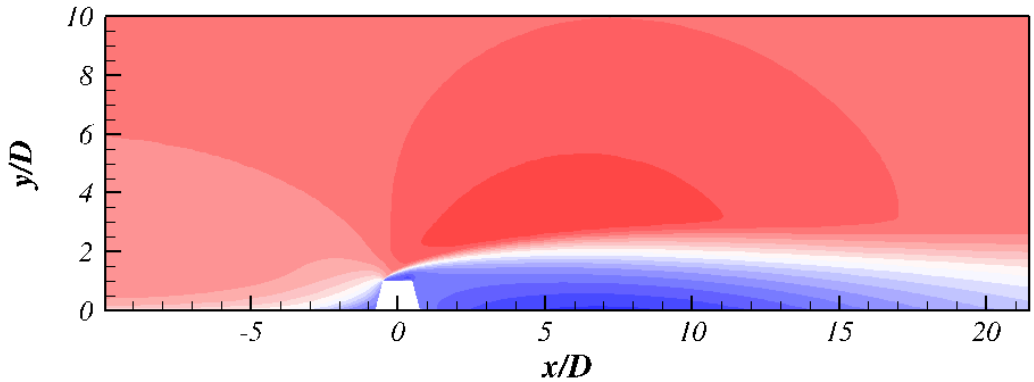

c)

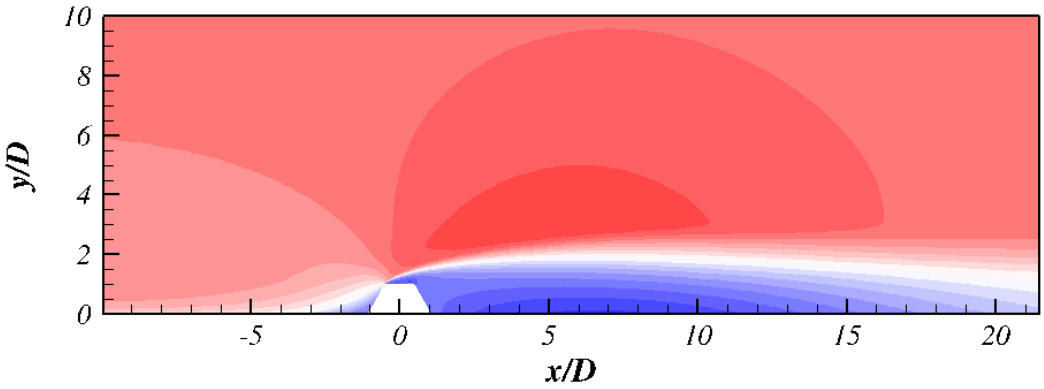
10
8
6
4
2
0
y/D
-5
0
5
10
15
20
x/D

d)

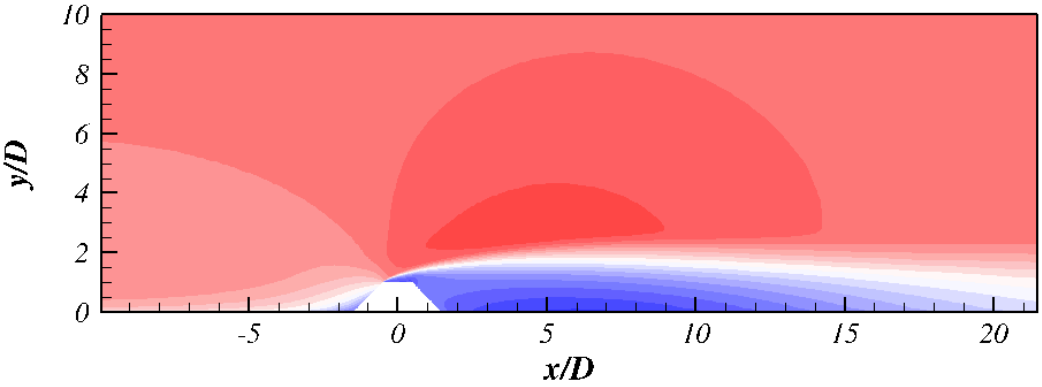
10
8
6
4
2
0
y/D
-5
0
5
10
15
20
x/D

e)

F 0°, (d)

4

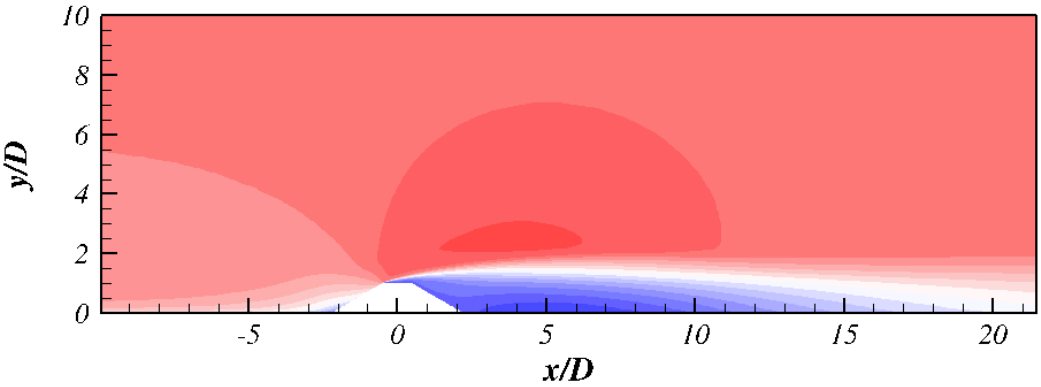
10
8
6
4
2
0
y/D
-5
0
5
10
15
20
x/D

The contours of vertical velocity are presented in Figure 5.6 for all angles α. There is an increase in the vertical velocity along the front face of the structure due to the conservation of mass, accelerating the mass above and past the structure to maintain conservation of energy. The intensity of the high vertical velocity region around the top left corner reduces with increasing α, as seen in Figure 5.6 (b) - (e). This is because the trapezoidal structures shift the direction of the flow more gradually. There is also a slight positive vertical velocity region at the rear face of the structure, indicating that a recirculation region forms behind the structures.

a)

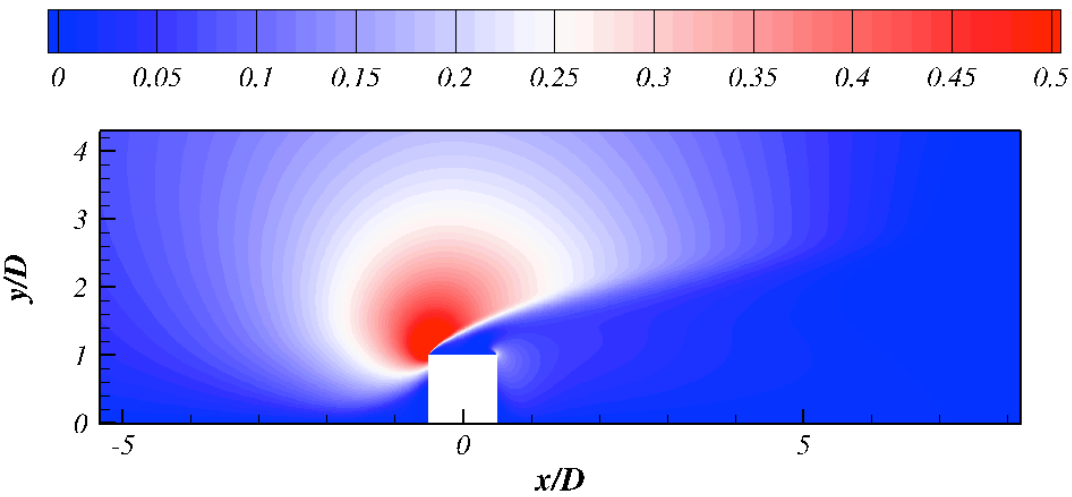

b)

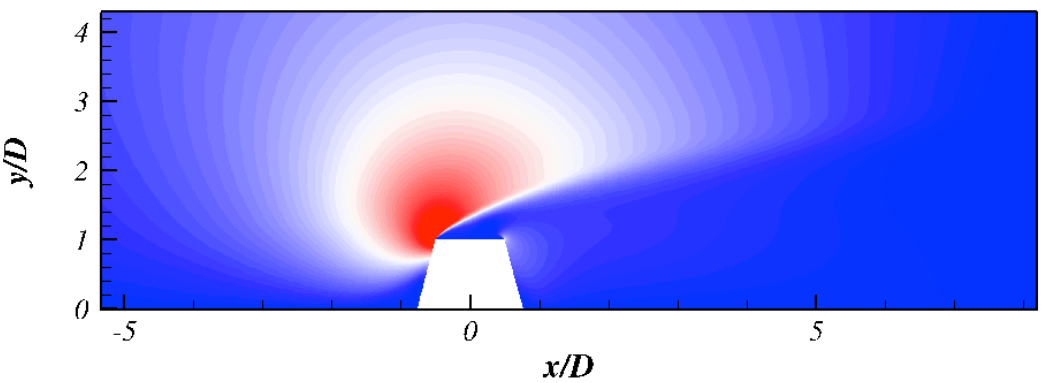

c)

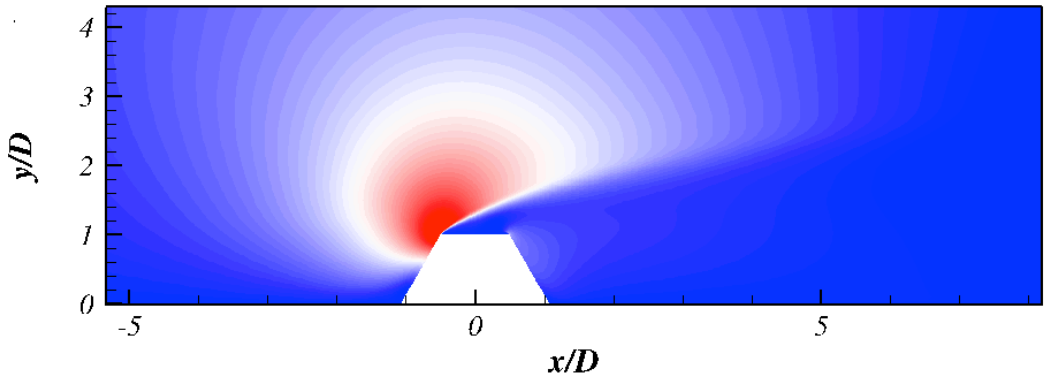

d)

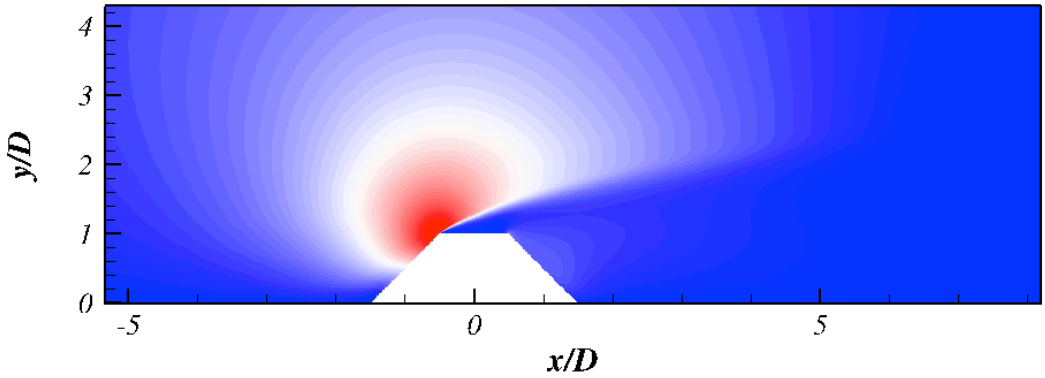

e)

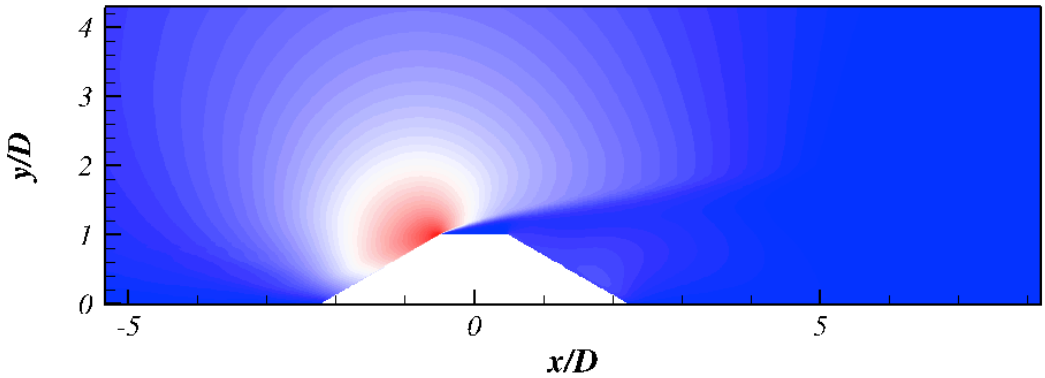

F

a

d) 45°

5.5 Bed shear stress and Scour

In actual subsea environment, bed shear stress is closely related to the scour process, which is removal of sediment around the base of subsea structures. High absolute values of τ/τ_∞ close to the structure can indicate a significant scour process, which is a typical source for failures in subsea operations (Zhao et al.,2012). Therefore, the present study investigates the bed shear stress on the seabed surfaces adjacent to the structures with different configurations of α.

a) b)

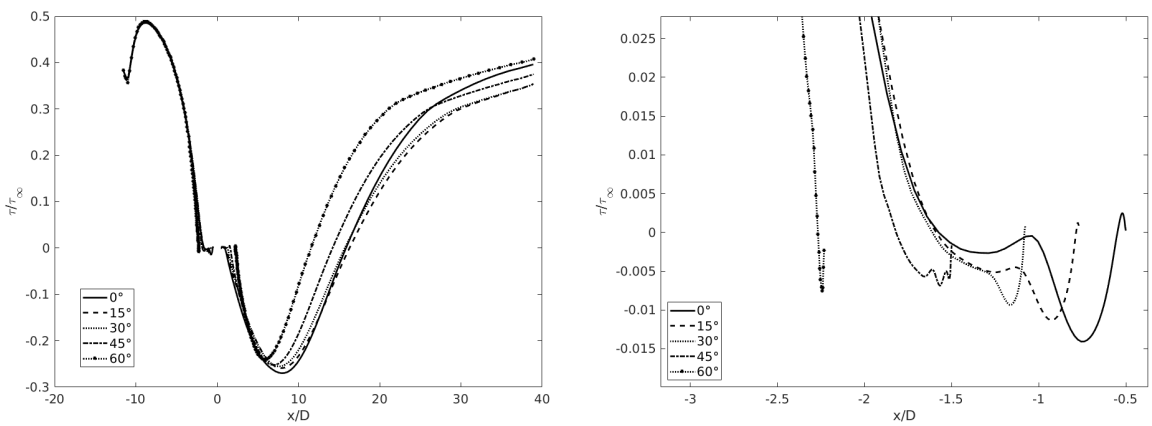

Figure 5.7 shows the non-dimensional bed shear stress τ/τ_∞, where τ_∞ is the undisturbed bed

Figure 5.7 Bed shear stress along the bottom surface at $\mathrm{Re} = 1 \times 10^6$ for: a) the whole domain. b) the front face of the structures

shear stress, along the bottom wall surface. τ/τ_∞ stagnates towards zero close to the front faces of the structures which are located $x/D = (-0.5, -0.768, -1.077, -1.5, -1.732)$ for $\alpha = (0°, 15°, 30°, 45°, 60°)$, respectively. Figure 5.7 (b) shows small negative τ/τ_∞ regimes in front of the structure for all α due to the backflow and the adverse pressure gradient caused by the conservation of energy. It can be observed that these negative regimes have lower amplitudes and are shorter in streamwise direction with increasing α. This behavior is due to the smooth flow transitions which is associated with larger α. The bed shear stress has a large negative region behind the structures due to the recirculation motions for all configurations. This negative region is also reduced with increasing α, which is consistent with the declining recirculation length. It is also worth noting that the absolute minimal value of the bed shear stress also decreases with increasing α and its location shifts closer to the structure as seen in Figure 5.7 (a).

5.6 Streamlines

To further investigate the flow around the five configurations with different α, streamlines are plotted at $Re = 1.19 \times 10^5$ in 5.9 and at $Re = 1.0 \times 10^6$ in Figure 5.8 and Figure 5.10. There are three main recirculation motions around the square structure seen in Figure 5.8. The first vortex (1) forms because the fluid particle hits the structure, flows downward and reverses its direction due to the bottom wall. A large recirculation is generated by the shear layer separation after the front top edge of the square (2), which also induces a smaller one in the downward corner of the square (3). For both Reynolds numbers, with increasing α, the length of the dominating vortex behind the structure decreases, seen in Figure 5.9 and Figure 5.10. In addition, as the flow tend to follow the angle of the front face after separation, the height of the recirculation reduces as the structure becomes flat. Furthermore, the increasing α gradually suppresses the vortices (1) and (2) from 5.8 (a), of the structure because the flow tends to be attached to the structure surface as seen in Figure 5.8 (b).

Figure 5.8 Detailed stream lines for Re=1×10^6 for (a) α=0° and (b) α=60°

a) b)

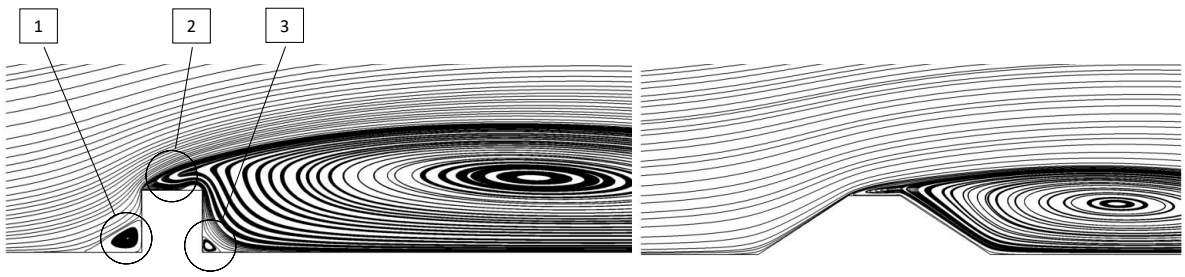

a)

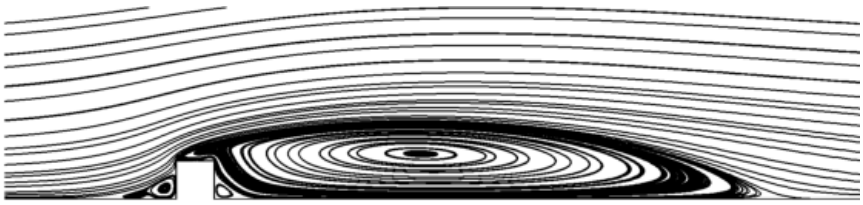

b)

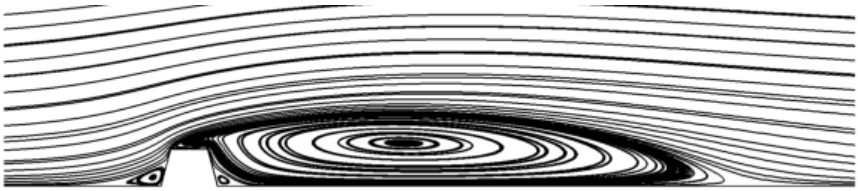

c)

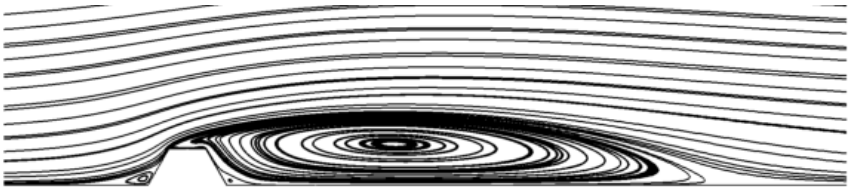

d)

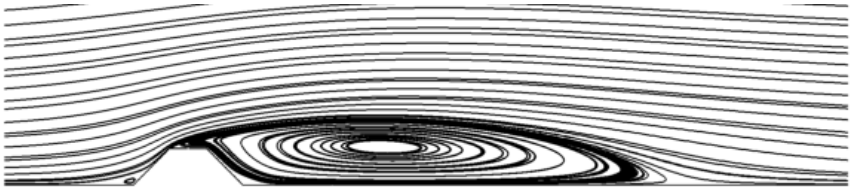

e)

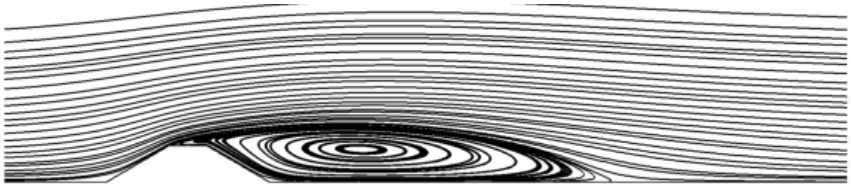

Figure 5.9 Stream lines at $\mathrm{Re} = 1.19 \times 10^5$ for varying α: (a) 0°, (b) 15°, (c) 30°, (d) 45° and (e) 60°

a)

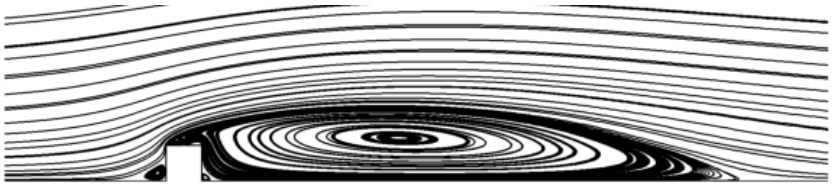

b)

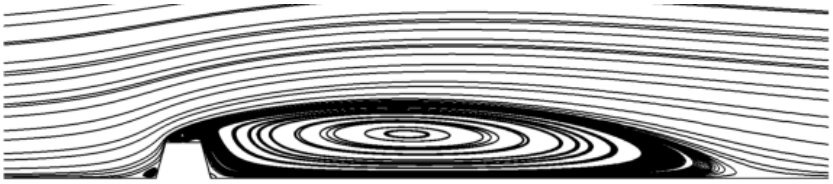

c)

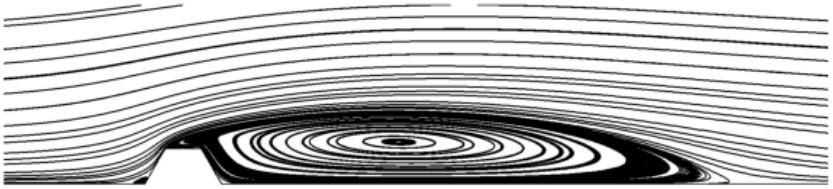

d)

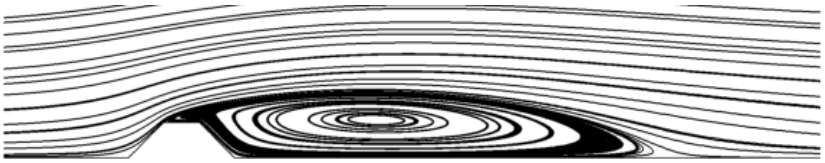

e)

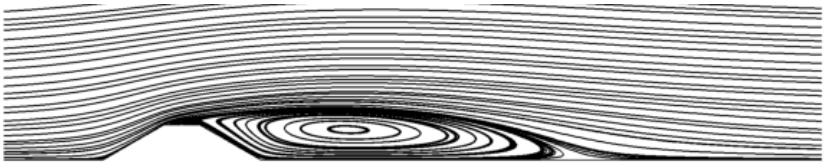

Figure 5.10 Stream lines at $\mathrm{Re} = 1 \times 10^6$ for varying α: (a) 0°, (b) 15°, (c) 30°, (d) 45° and (e) 60°

6 Results and Discussion for Tandem Case

This chapter presents and discusses the results for the tandem case. The chapter presents the convergence study with respect to G/D and investigates the hydrodynamic coefficients, pressure distributions, streamlines and velocity profiles by varying the parameters of G/D and α. All charts in this section are based on the data from Table 6.1, Table 6.2, Table 6.3 and Table 6.4. This chapter will use Square 1 and Square 2 when referring to the first and second square in tandem, respectively. Structure 1 and Structure 2 will similarly be used when referring to all trapezoidal configurations, including the square configuration.

Mesh	G/D	C_{D1}	C_{L1}	C_{D2}	C_{L2}
33005	2	1.118	0.706	-0.183	0.587
54135	2	1.112	0.717	-0.194	0.581
72895	2	1.109	0.721	-0.197	0.578
104838	2	1.105	0.719	-0.196	0.574
37139	3	1.134	0.755	-0.286	0.536
60495	3	1.126	0.762	-0.296	0.527
116138	3	1.116	0.758	-0.290	0.521
42219	6	1.150	0.718	-0.458	0.282
66855	6	1.138	0.716	-0.446	0.279
134218	6	1.132	0.711	-0.437	0.281
49839	10	1.061	0.625	-0.215	0.138
76395	10	1.051	0.621	-0.212	0.137
156818	10	1.045	0.618	-0.213	0.135
53649	14	1.026	0.573	-0.013	0.123
89115	14	1.017	0.577	-0.012	0.120
169695	14	1.012	0.580	-0.012	0.119

Table 6.1 Results of convergence study for hydrodynamic coefficients for Square 1 and Square 2

Table 6.2 Hydrodynamic coefficients for Structure 1 and Structure 2 with G/D = 6 for trapezoidal configurations using mesh number of 66855

α	C_{D1}	C_{L1}	C_{D2}	C_{L2}
0	1.138	0.716	-0.446	0.279
15	1.106	0.605	-0.434	0.387
30	1.104	0.533	-0.415	0.435
45	0.934	0.479	-0.382	0.450
60	0.728	0.443	-0.253	0.442

Table 6.4 Hydrodynamic coefficients for Structure 1 and Structure 2 with G/D = 10 for trapezoidal configurations using mesh number of 76395

α	C_{D1}	C_{L1}	C_{D2}	C_{L2}
0	1.051	0.621	-0.212	0.137
15	1.023	0.504	-0.198	0.206
30	0.969	0.421	-0.172	0.249
45	0.864	0.366	-0.119	0.274
60	0.671	0.335	-0.014	0.284

Table 6.3 Hydrodynamic coefficients for Structure 1 and Structure 2 with $G/D = 14$ for trapezoidal configurations using mesh number of 89115

α	C_{D1}	C_{L1}	C_{D2}	C_{L2}
0	1.017	0.577	-0.012	0.120
15	0.990	0.449	0.001	0.160
30	0.939	0.328	0.021	0.187
45	0.841	0.316	0.063	0.209
60	0.657	0.298	0.141	0.227

6.1 Convergence

Convergence studies with all gap ratios, $G/D = 2, 3, 6, 10$ and 14, are performed with respect to hydrodynamic quantities for both squares in tandem to ensure mesh independence. First, 4 different mesh densities with $G/D = 2$ were constructed to establish converged results for the original mesh set up, which was found for the normal mesh at 54135 cells. Thereafter, three

meshes of different densities; coarse, normal and dense were constructed for each G/D as shown in Table 5.1 where all the normal meshes for square configurations were found to provide sufficient mesh resolution, with difference less than 5% for any hydrodynamic coefficient from its corresponding dense mesh. Figure 6.1 shows the variation of hydrodynamic coefficients with the grid numbers. The converged trapezoidal mesh configurations from the single structure case were combined with the converged mesh configuration with $G/D \geq 6$ from Figure 6.1 to study the trapezoids in tandem as well. Investigations with $G/D < 6$ are not carried out for trapezoids in tandem because of the high skewness of the current mesh set up for trapezoidal geometries at low G/D.

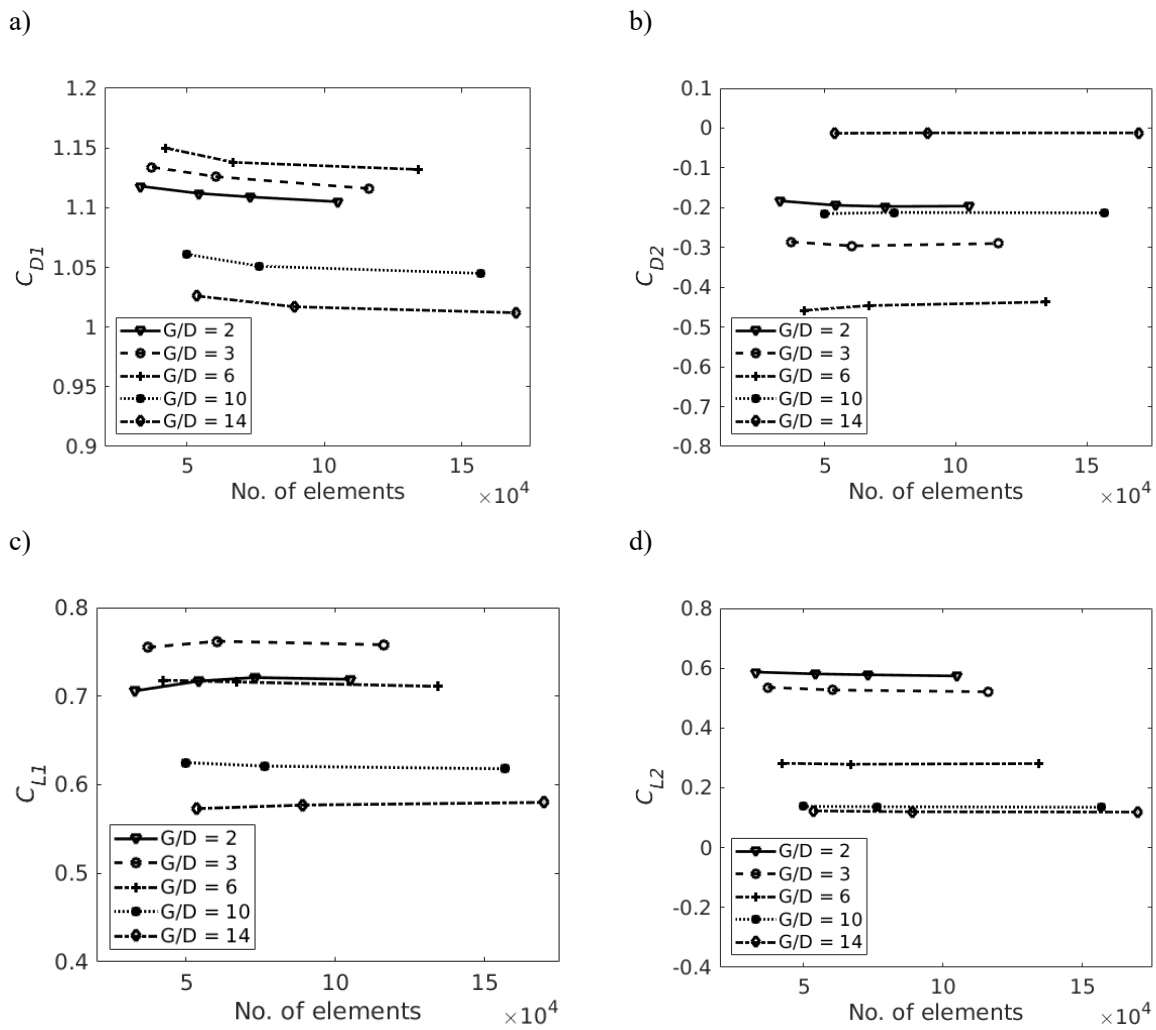

Figure 6.1 Convergence study for wall-mounted squares in tandem with $G/D = 2,3,6,10$ and 14 for the hydrodynamic quantities: a) C_{D1} for Square1, b) C_{D2} for Square2, c) C_{L1} for Square1 and d) C_{L2} for Square2

6.2 Effects of G/D and α on hydrodynamic quantities

Figure 6.2 presents the variation of the hydrodynamic quantities for the structures of same configuration at G/D at $Re = 1.19 \times 10^5$. The drag coefficient of Square 1 is increasing towards $G/D = 6$ however declining for higher G/D as seen in Figure 6.2 (a). The opposite is occurring for Square 2, seen in Figure 6.2 (b), where a distinct maximum absolute minimal value for the C_{D2} is found at $G/D = 6$ and hence increasing linearly with the G/D. This relationship can be explained by the shielding effect, from Square 1, on Square 2 and the retarded vortex development between the squares which will be further explained in Chapter 6.3 and 6.5. The lift coefficients for Square1 is maximum with $G/D = 3$ and is monotonically decreasing with increasing G/D. Furthermore, C_{D1} and C_{L1} for Structure 1 decrease as α becomes larger with $G/D > 6$ for all configurations. C_{L2} is decreasing with the G/D for all structures and its variation tends to be flat out for higher G/D.

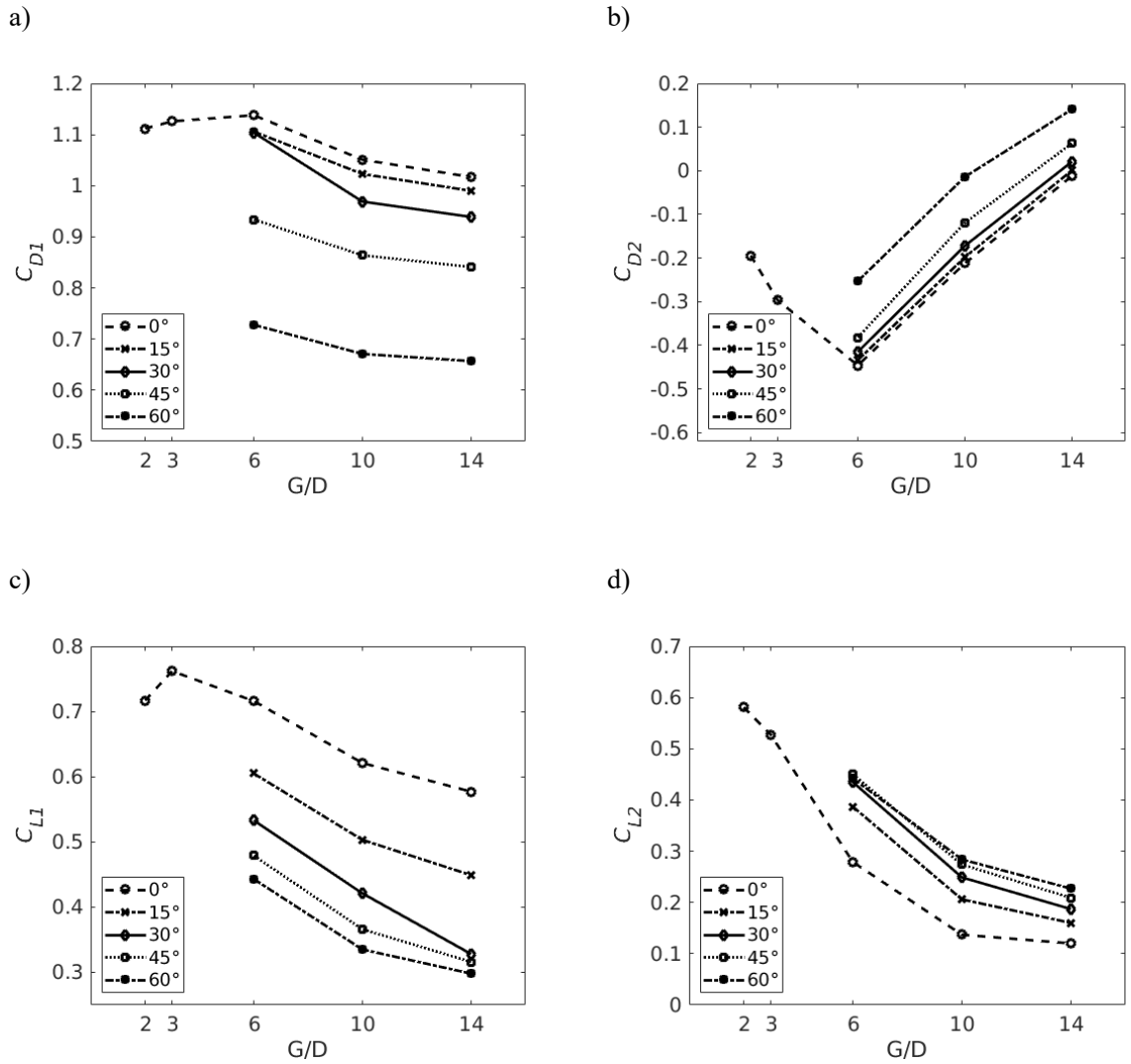

Figure 6.2 Investigation of gap ratios G/D for different configurations of α for the hydrodynamic quantities: a) C_{D1} for Square 1, b) C_{D2} for Square 2, c) C_{L1} for Square 1 and d) C_{L2} for Square 2

The variations of hydrodynamic quantities with $\alpha = 0°$, $15°$, $30°$, $45°$ and $60°$ are investigated with $G/D = 6{,}10$ and 14 and presented in Figure 6.2. Both C_{D1} and C_{L1} are decreasing, while C_{D2} and C_{L2} are increasing, with larger α. The effects of the additional Structure2 are compared to the single structure case in Figure 6.2 (a) and (c). Here C_{D1} follows the same trend as the single structure case by declining with increasing α. Furthermore, the hydrodynamic effects of the gap ratios for the square configuration increase between $2 \leq G/D \leq 6$ and the C_{D1} has a maximum deviation of 13.6% at $G/D = 6$ compared to the single square case. Moreover, it can be seen in Figure 6.2 (a) that the discrepancy of C_D between the single square and $G/D = 14$ is 0.004%, which indicates that the tandem drag effects on Structure1 has disappeared.

However, Figure 6.3 (c) shows that the C_L for the single structure is most compatible with $G/D = 10$ while $G/D = 14$ have lower values of C_L for all α. This indicates that the lift effects of Structure2 on Structure1 not have fully disappeared. From Figure 6.2 (b), the absolute value of C_{D2} slightly decreases with larger α and has negative values for $G/D = 6$ and 10. However, with $G/D = 14$, the C_{D2} becomes positive and increases with larger α. From Figure 6.2 (d), it is clear that $G/D = 6$ have the largest values of C_{L2} compared to the other G/D. C_{L2} for $G/D = 6$ has its maximum value at $\alpha = 45°$, and slightly declines when $\alpha = 60°$. This is not the situation for $G/D = 10$ and 14, where the C_{L2} is only slightly decreasing with larger α.

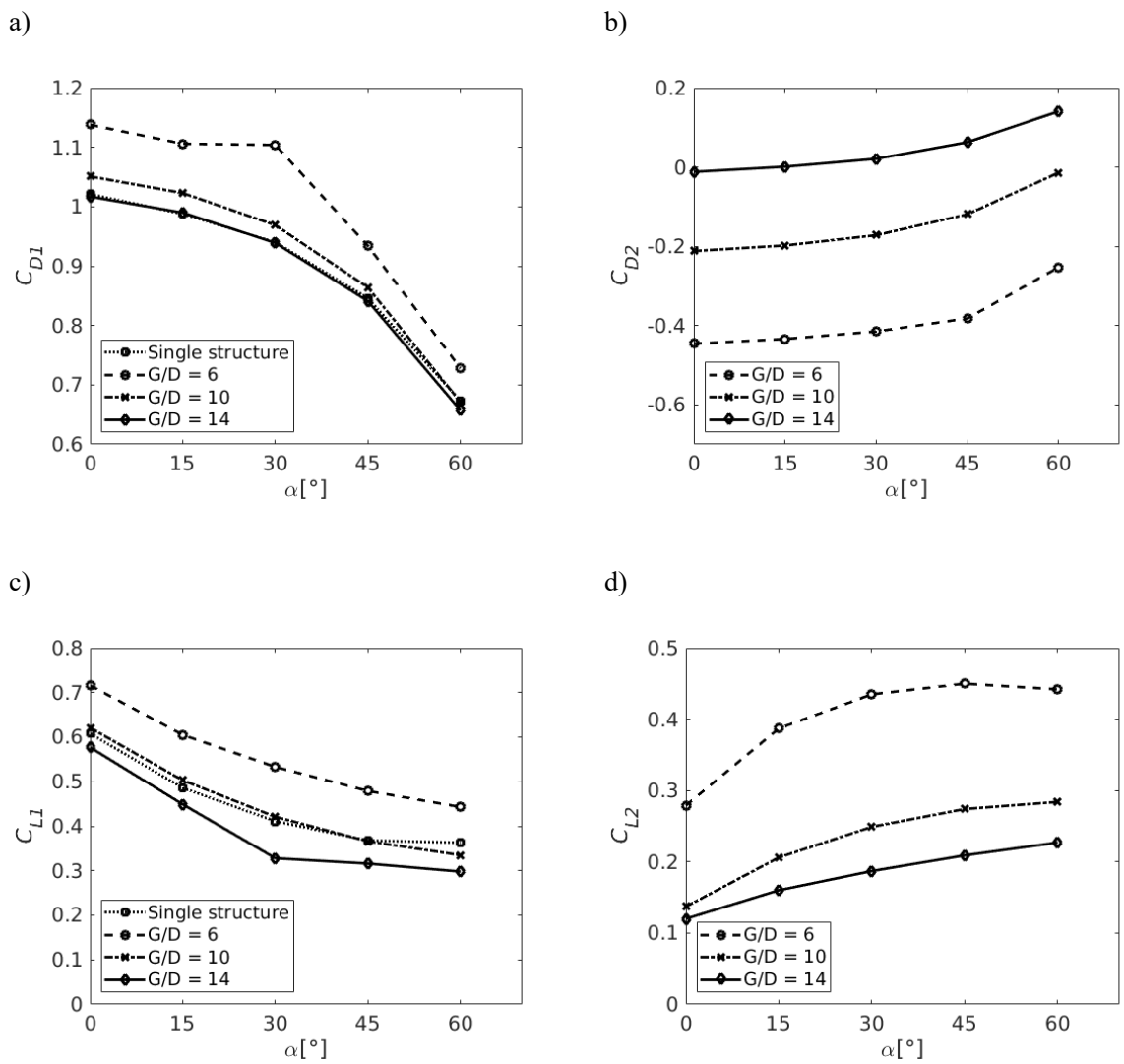

Figure 6.3 Investigation of α for gap ratios of $G/D = 6,10,14$ as well as for singular structures, for the hydrodynamic quantities: a) C_D for Square 1, b) C_D for Square 2, c) C_L for Square 1 and d) C_L for Square 2

6.3 Pressure distribution

The pressure distributions for all $G/D = 2,3,6,10$ and 14 for squares in tandem have been investigated and presented in Figure 6.4. It is worth to note that the pressure plotting scale for the tandem case has been adjusted from the single square case with the maximum positive pressure of 0.29 in front of Structure 1. Therefore, the pressure contour cases are not adequate for comparison.

6.3.1 Pressure distribution for squares in tandem

A large positive pressure region is observed at the front face of Square 1 due to the conservation of energy. Furthermore, for all G/D, two negative pressure zones are formed. One is formed in between the squares and the other one is formed behind Square 2. The negative pressure zone between the squares is associated with the vortex motions, seen from the streamline plots in Figure 6.5.2, and contributes most to the total drag force. The main contribution of the drag is from the pressure difference between the front and back face of the structures, which is the reason why C_{D2} is negative for all the G/D for square configurations. Dai et al. (2017) has also observed that the pressure zone between the structures imposes a suction force on Square 2, hence results in negative C_{D2} due to the pressure difference. For $G/D = 14$, C_{D2} is almost zero and the pressures adjacent to Square 2 has reached equilibrium.

The strength of the negative pressure zone between the two square increases in the range of $2 < G/D < 6$ and decreases in the range of $6 < G/D < 14$ as indicated in Figure 6.4 (c) – (e), which can be associated with the drag coefficient variations in Square 1 and Square 2. The second pressure zone, forming at $x/D \sim 5$ behind Square 2 as seen in Figure 6.4 (a) and (b) disappears in Figure 6.4 (c) - (e). For $G/D = 6$, it seems that the two negative pressure zones consolidate and a negative pressure zone between the squares is formed, hence imposing the highest pressure on both structures. Moreover, the strength of the negative pressure zone decreases for G/D is 6 to 14 and seems to be less affected by Square 2.

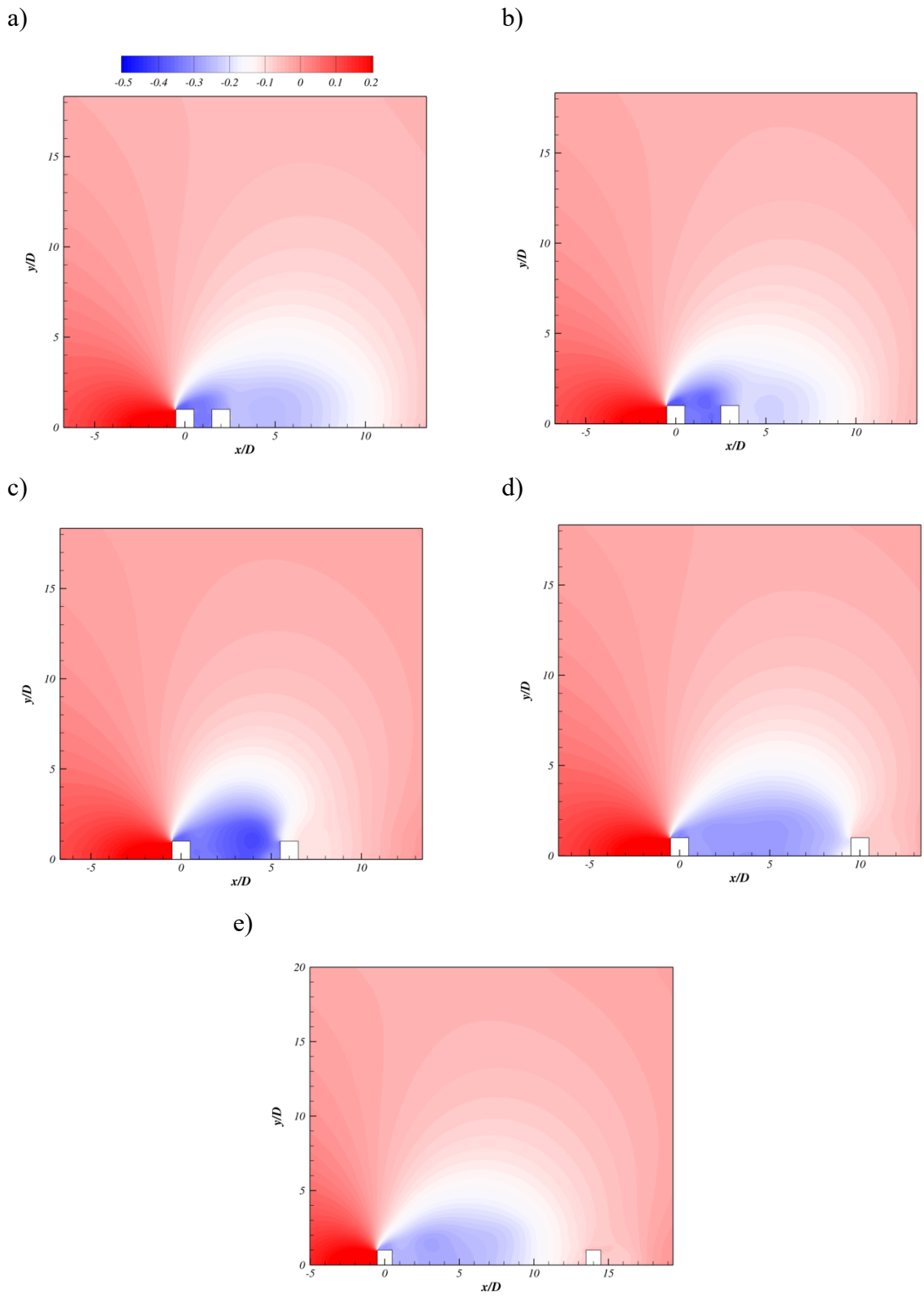

Figure 6.4 Pressure contours for wall-mounted squares in tandem with gap ratios of: a) $G/D = 2$, b) $G/D = 3$, c) $G/D = 6$, d) $G/D = 10$ and e) $G/D = 14$

6.3.2 *Pressure distribution for trapezoids in tandem*

Figure 6.5 shows the pressure contours of all trapezoidal configurations with $G/D = 6$, which is found to impose the most drag on the both squares in tandem. The pressure distribution at the front face of Structure 1 is, as for the single structure case, decreasing with increasing α. The strength of the negative pressure zone between the structures is also decreasing for increasing α and this trend is also observed for all configurations with $G/D > 6$ seen in Figure 6.5 and Figure 6.6. The low negative pressure zone forming behind Structure 2 is slightly increasing in size with increasing α disparate to the negative pressure zone behind Structure1. This is because the pressure zone behind Structure 2 is depending on the flow velocity over Structure 2 which again is governed by the shielding effect from Structure1. Structure 2 will be subjected to higher flow velocities with reduced shielding effect from Structure1, hence creating a higher negative pressure zone because of Bernoulli's principle.

The negative pressure region behind Structure 1 decreases in strength which is similar to $G/D = 6$ and $G/D = 14$. The increased negative pressure zone behind Structure 2, associated with increasing α, is obvious for $G/D = 10$ as seen in Figure 6.6. Here, the strength of the negative pressure region is clearly increased behind Structure 2 seen in Figure 6.6 (d) and (e). Figure 6.7 presents the pressure contours with all α configurations with $G/D = 14$. Here, the negative pressure region behind Structure 1 seems to behave identical to that of a single configuration at $Re = 1 \times 10^6$. This is further supported by the fact that the drag coefficient is

α	C_{D1}	C_{L1}	C_{D2}	C_{L2}
0	1.017	0.577	-0.012	0.120
15	0.990	0.449	0.001	0.160
30	0.939	0.328	0.021	0.187
45	0.841	0.316	0.063	0.209
60	0.657	0.298	0.141	0.227

almost the same for the cases of single square and squares in tandem with $G/D = 14$. For Structure 2 with α > 0° the pressure on its front face shifts to be positive and becomes larger with increasing α, which leads to a positive drag on Structure 2 shown in

. This is because the vortex motions behind Structure 1 are different for each trapezoidal configuration, hence creating different downstream flows which Structure 2 is subjected to. It is observed in Figure 6.7 (e) that pressure contours behind Structure 2 is formed in a similar manner as Structure 1 since the flow profile it is subjected to has started to recover from the

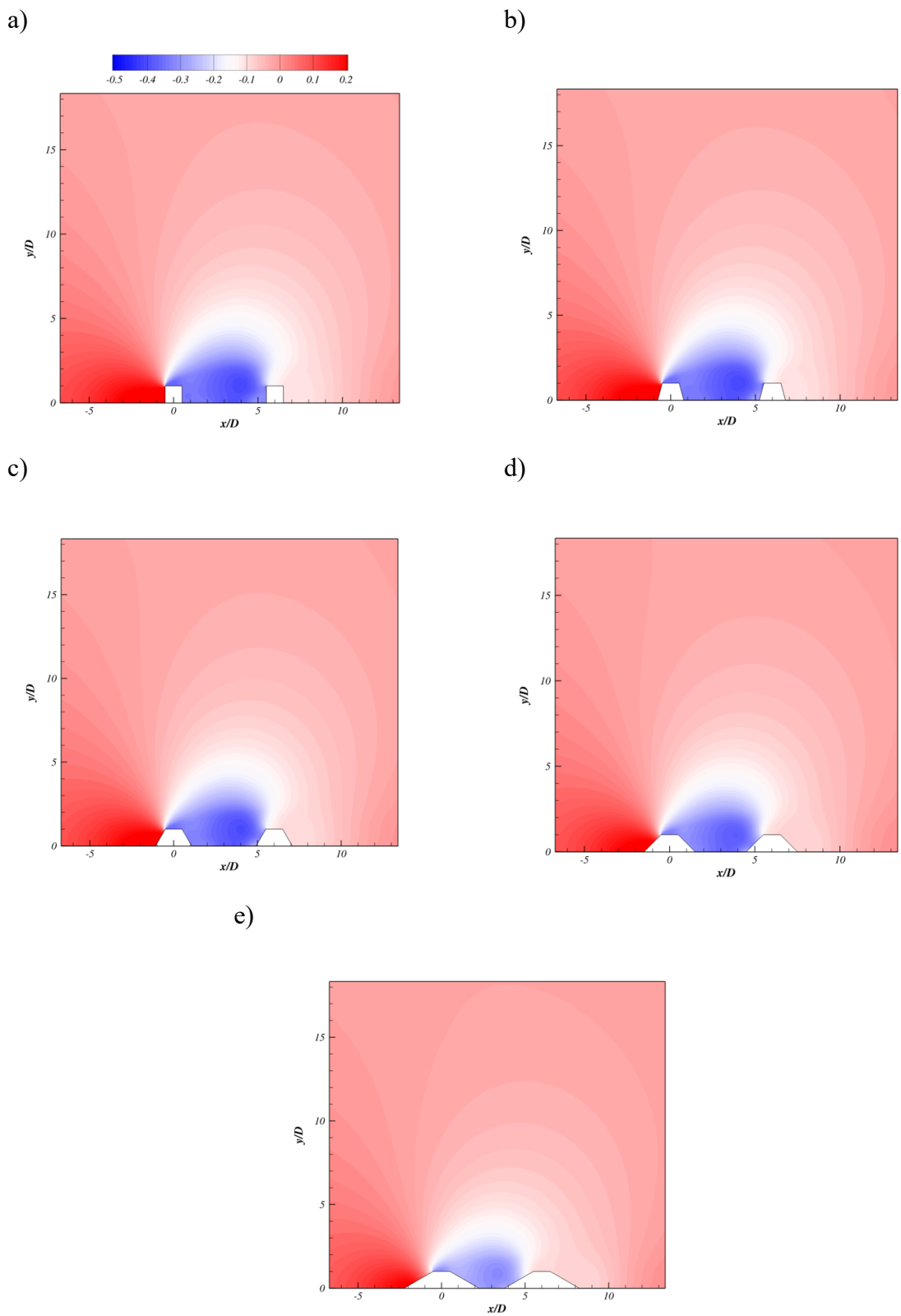

Figure 6.5 Pressure contours for $G/D = 6$ for varying trapezoidal configurations α: (a) 0°, (b) 15°, (c) 30°, (d) 45° and (e) 60°

effects of Structure 1. This subsequently results in similar hydrodynamic quantities on Structure 2 to those on Structure 1 due to Bernoulli's principle.

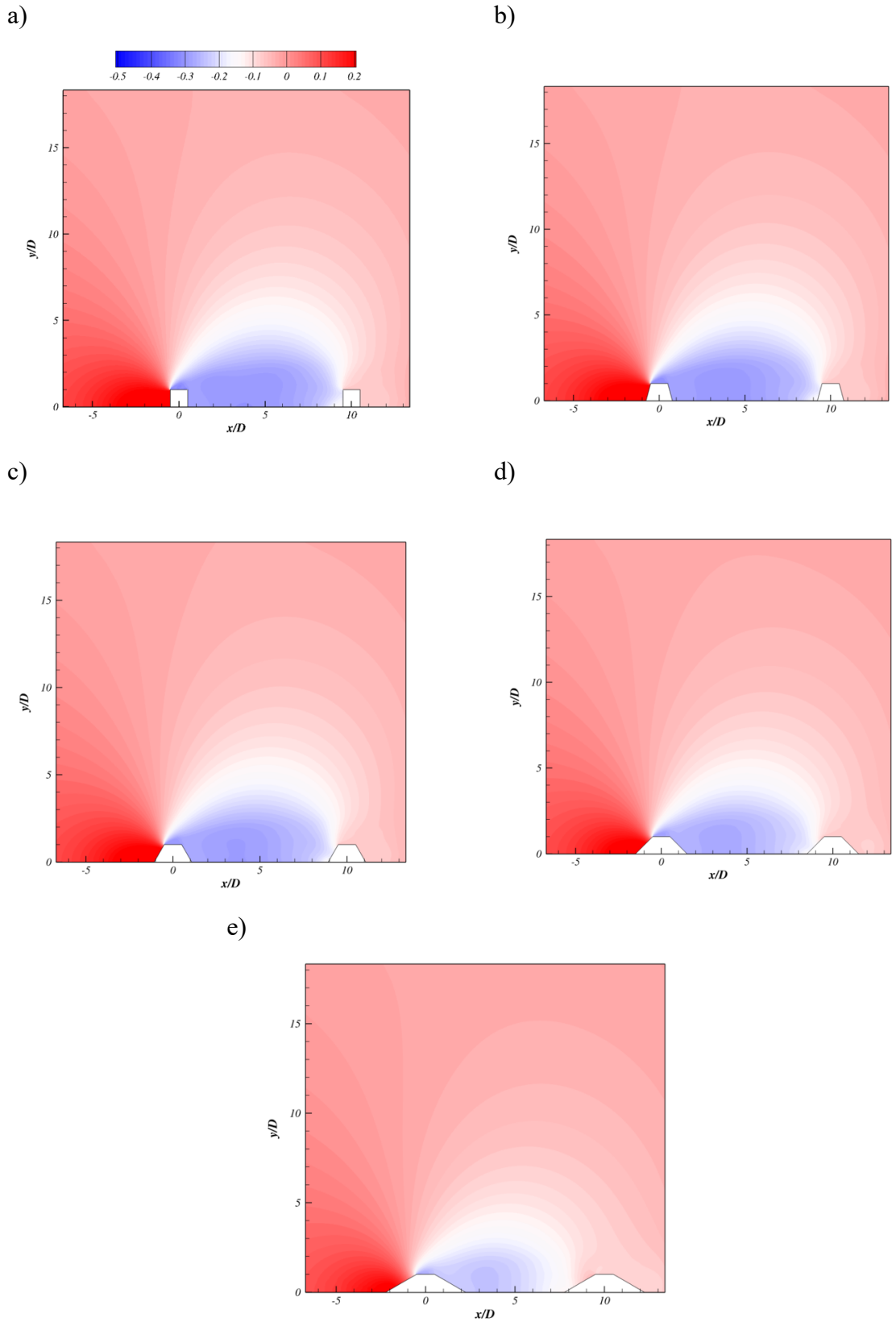

Figure 6.6 Pressure contours for $G/D = 10$ for varying trapezoidal configurations α: (a) 0°, (b) 15°, (c) 30°, (d) 45° and (e) 60°

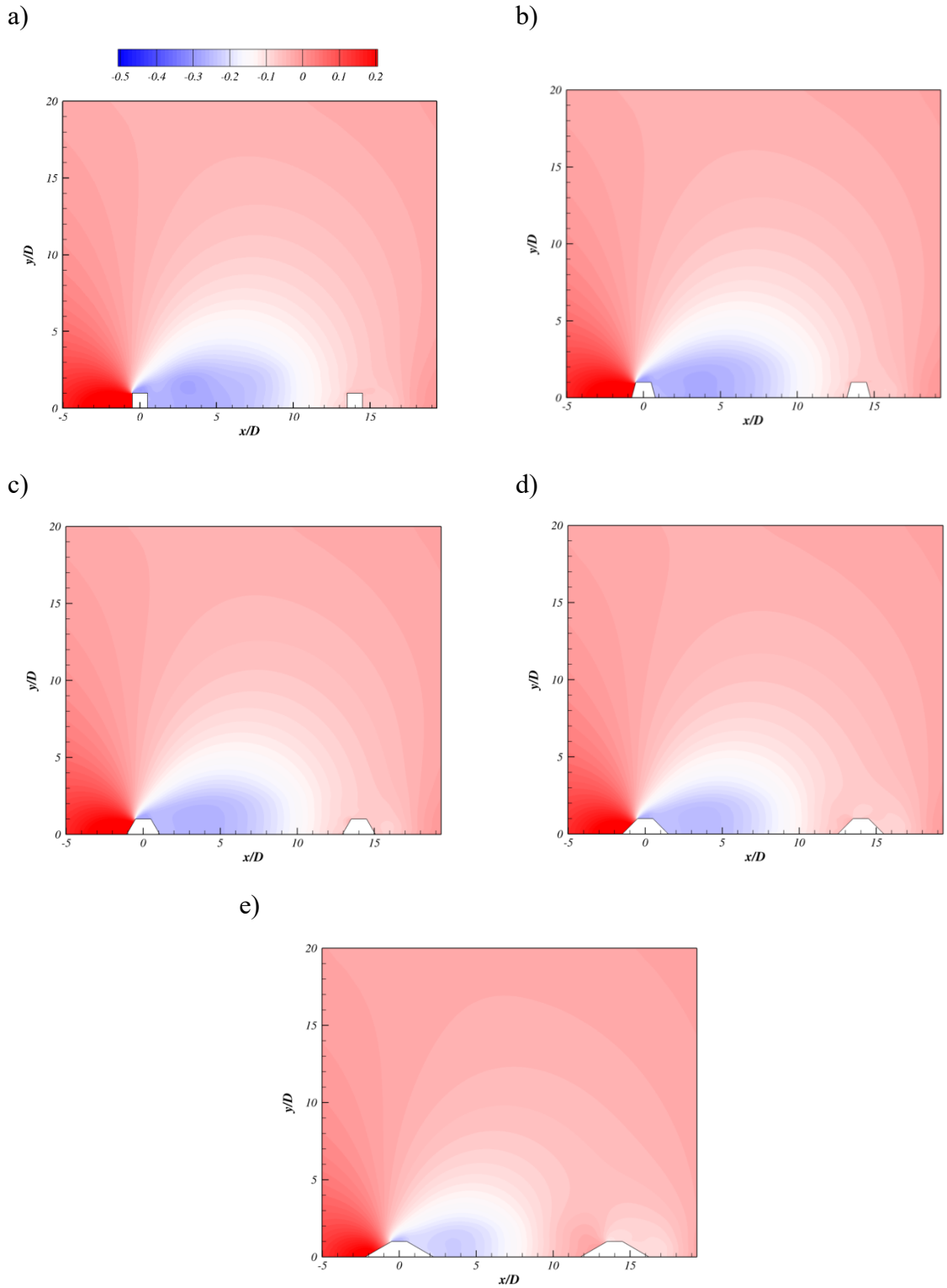

Figure 6.7 Pressure contours for $G/D = 14$ for varying trapezoidal configurations α: (a) 0°, (b) 15°, (c) 30°, (d) 45° and (e) 60°

6.4 Horizontal velocity contours

6.4.1 Horizontal velocity contours for squares in tandem

The horizontal velocity profiles for wall-mounted squares in tandem for $G/D = 2,3,6,10$ and 14 is presented in Figure 6.8. A high-speed region V1 is formed at $(x/D, y/D) = (0,2)$ above the shear layer shown in Figure 6.8 (a). It is obvious that $G/D = 6$ have a squeezed V1, however, the strength of its core region is the largest of all gap ratios and can be seen with contours inside V1. Moreover, for $G/D > 6$ V1 is expanded with increasing G/D following Square 2. The low-speed region between the two squares are coherent with the vortex motions shown in Figure 6.11. For $G/D = 2, 3$ and 6 the core of the low-speed region is located close to the left top edge of Square 2. However, when $G/D > 6$ the core of the low-speed region is expanded and is attached to the bottom wall.

a)

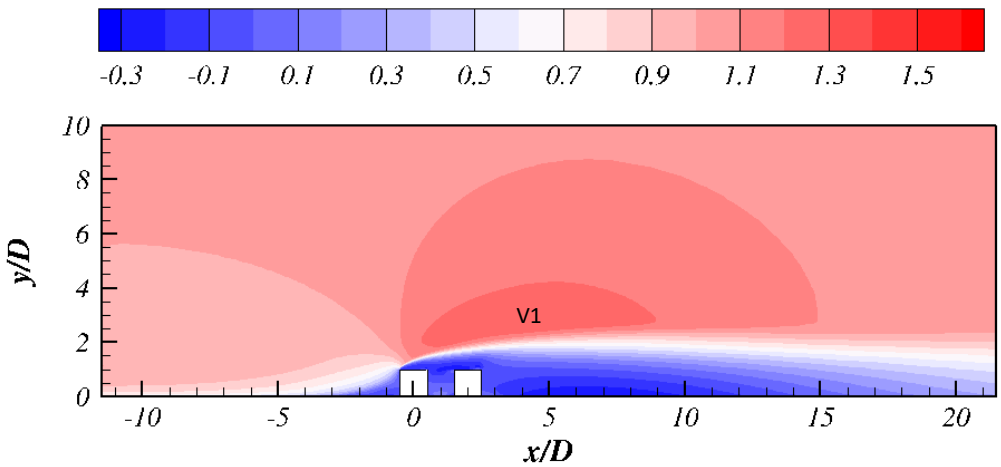

b)

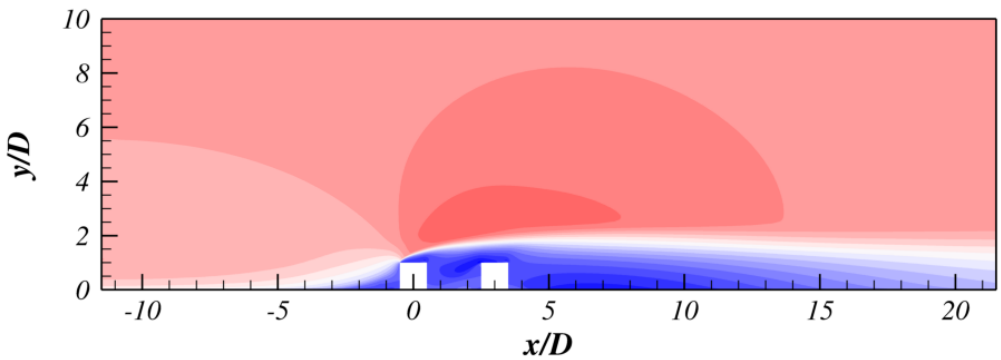

c)

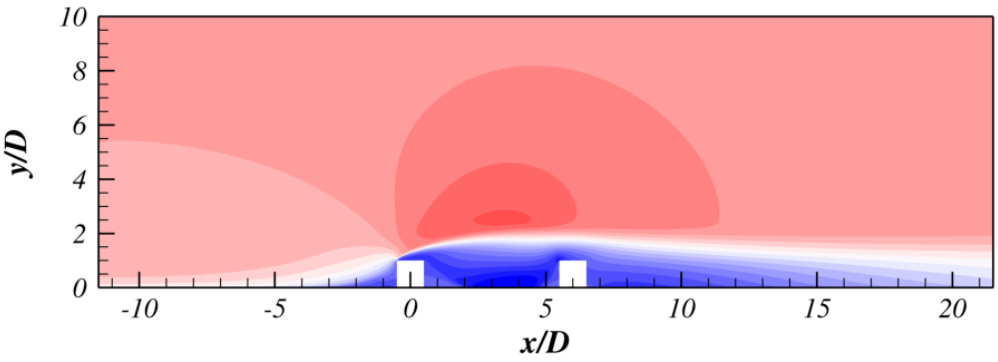

d)

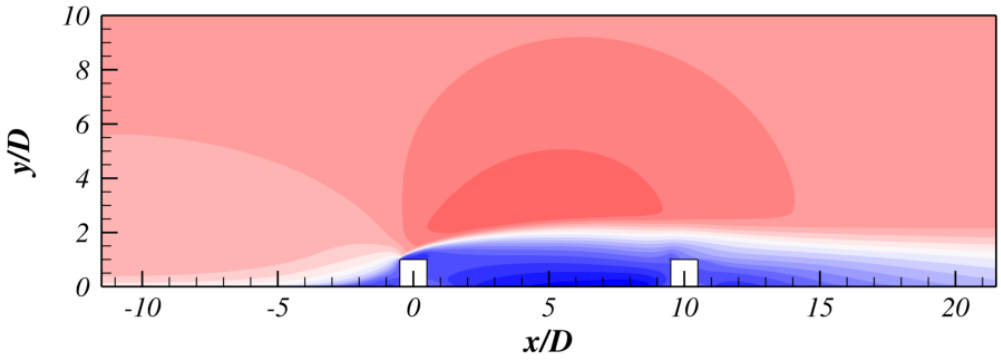

e)

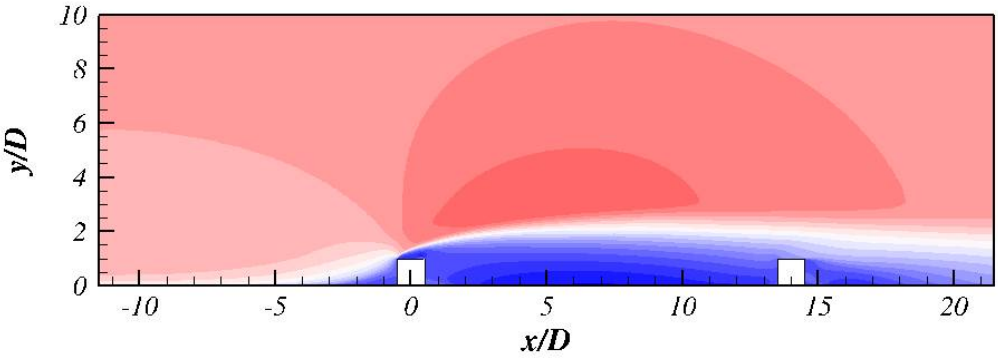

Figure 6.8 Horizontal velocity contours for wall-mounted squares in tandem with gap ratios of: a) $G/D = 2$, b) $G/D = 3$, c) $G/D = 6$, d) $G/D = 10$ and e) $G/D = 14$

6.4.2 *Horizontal velocity contours for trapezoids in tandem*

The streamwise velocity contours for all α with $G/D = 6$ and 14 are presented in Figure 6.9 and Figure 6.10, respectively. The high-speed velocity core V1, present for $G/D = 6$, is visible by contours for $\alpha \leq 30°$ in Figure 6.8 (a) – (c). However, as α increases, the area of this region is decreasing and the maximum velocity in the core of the high-speed region also decreases.

a)

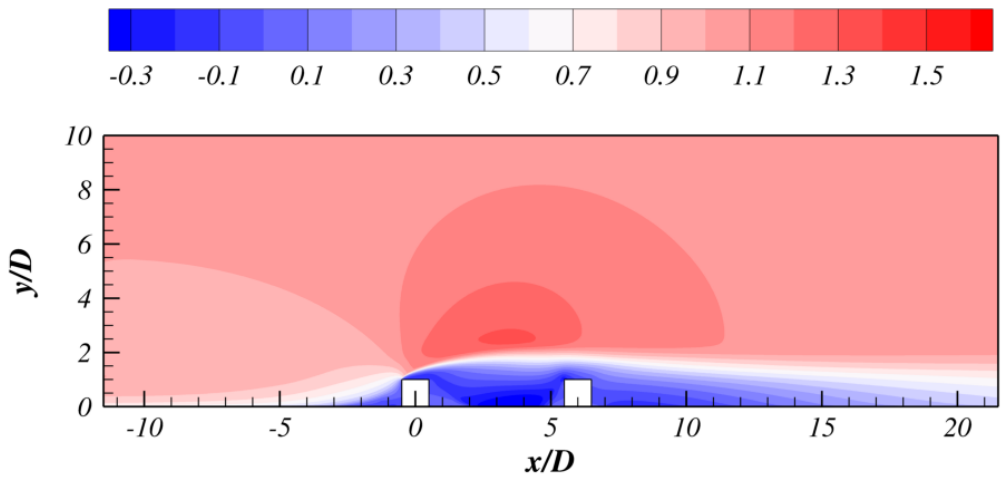

b)

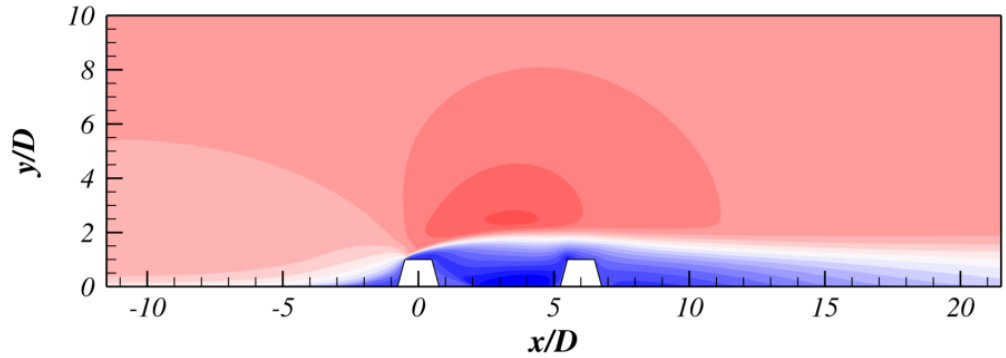

c)

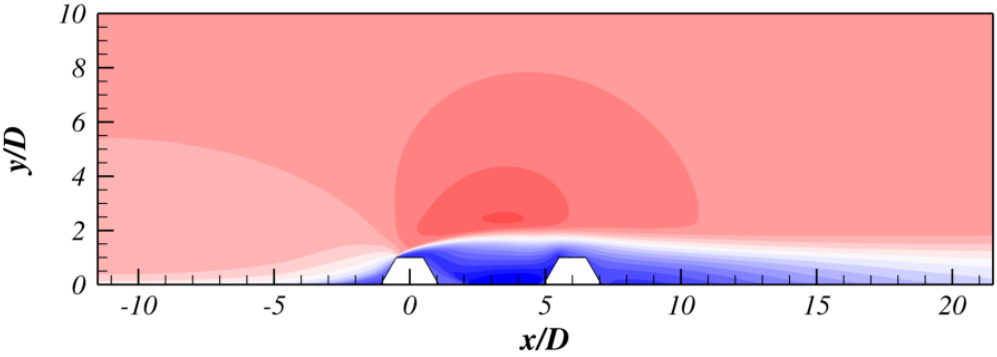

d)

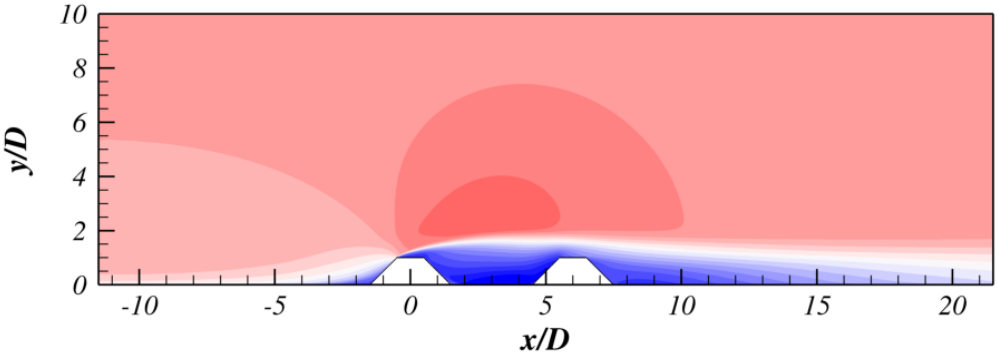

e)

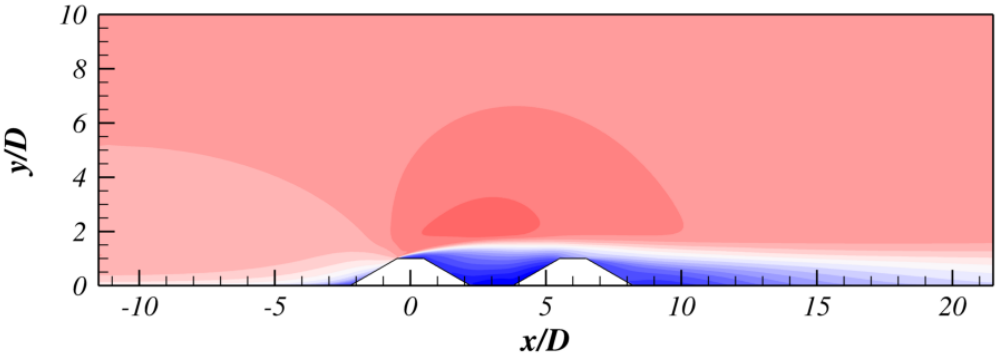

Figure 6.9 Horizontal velocity contours for $G/D = 6$ for varying trapezoidal configurations α: (a) 0°, (b) 15°, (c) 30°, (d) 45° and (e) 60°

a)

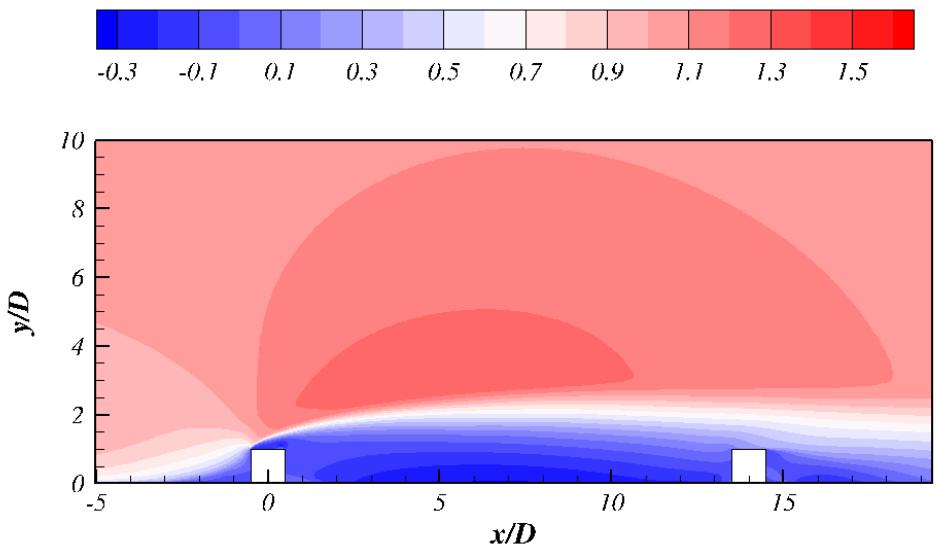

b)

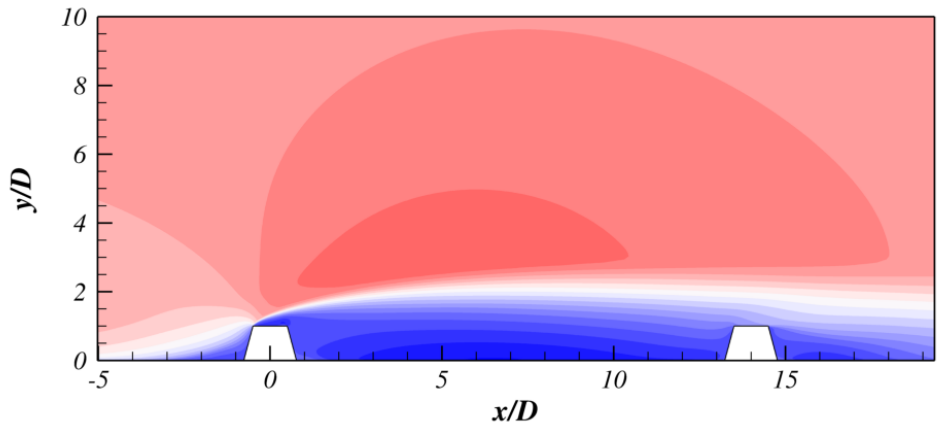

c)

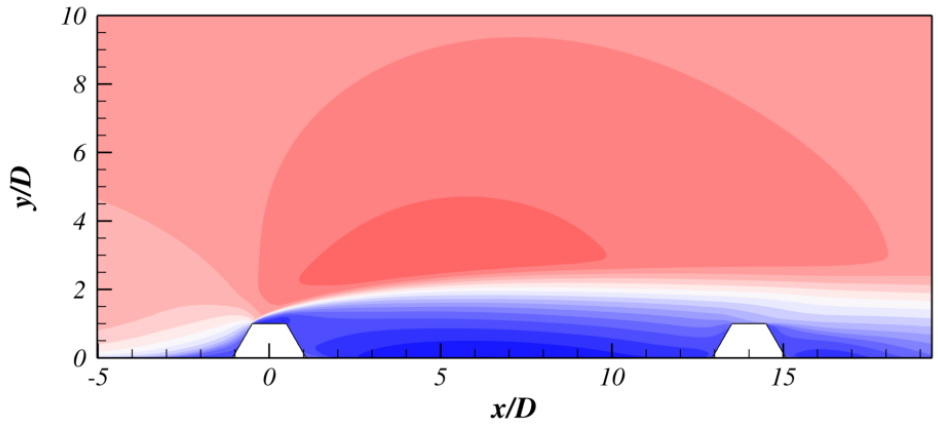

d)

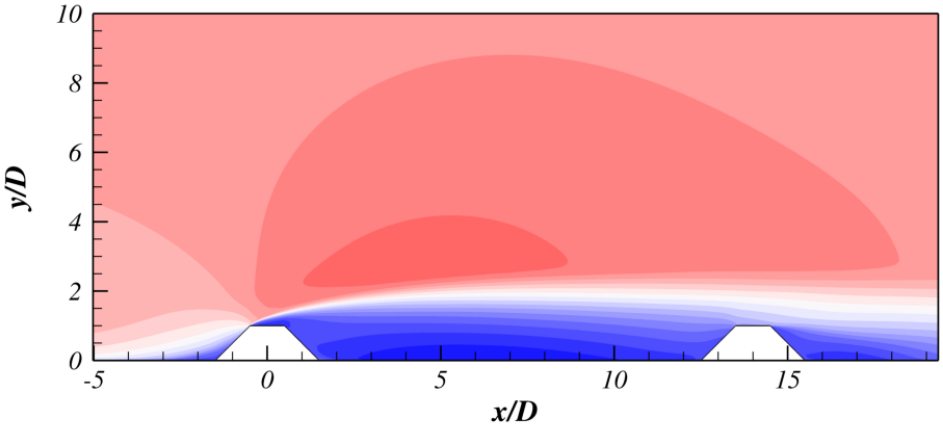

e)

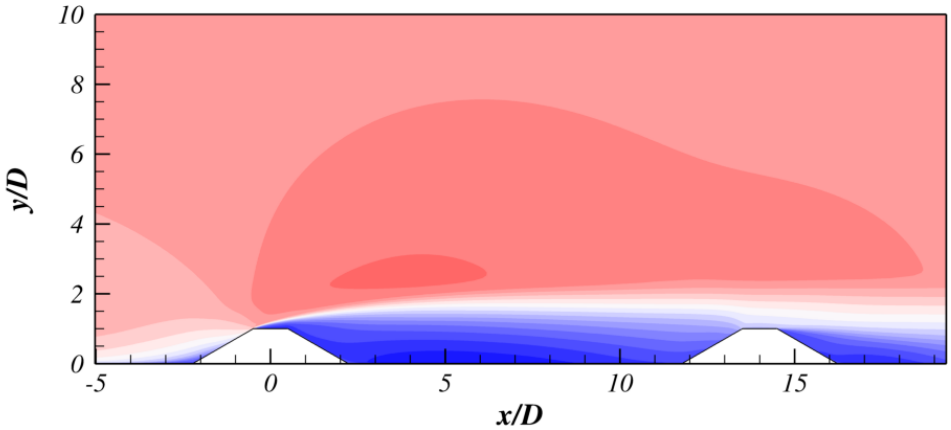

Figure 6.10 Horizontal velocity contours for $G/D = 14$ for varying trapezoidal configurations α: (a) 0°, (b) 15°, (c) 30°, (d) 45° and (e) 60°

6.5 Streamlines

The streamlines for $G/D = 2, 3, 6, 10\ and\ 14$ are plotted for squares in tandem, and vortexes are denoted Rx, where x is the number of the vortex explained in Figure 6.11. Moreover, the streamlines for all trapezoidal configurations have been plotted for $G/D = 6$ and 14.

6.5.1 Streamlines over tandem squares

The streamlines over the square configurations, presented in Figure 6.11, shows 7 visible vorticities whose appearances changes with different G/D. Figure 6.11(a), where $G/D = 2$, shows that the small R1 at the front face of Square 1 is developed in the same manner as the single square case. However, the vorticities downstream of Square 1 is varying with G/D. The elongated R2 is located on top of the two tandem squares and induces R3 in a counter clockwise direction in the gap between the two squares. At the back surface of Square 2, there is a small counterclockwise R4 which is induced by the large downstream R5, similar to the single square case. Increasing the gap distance from $G/D = 1$ (a) to $G/D = 2$ (b), the R2 starts to suppress R3 and becomes a larger vortex attached to the bottom wall. R3 additionally induces two small vorticities: R6 and R7 in a counter clockwise direction.

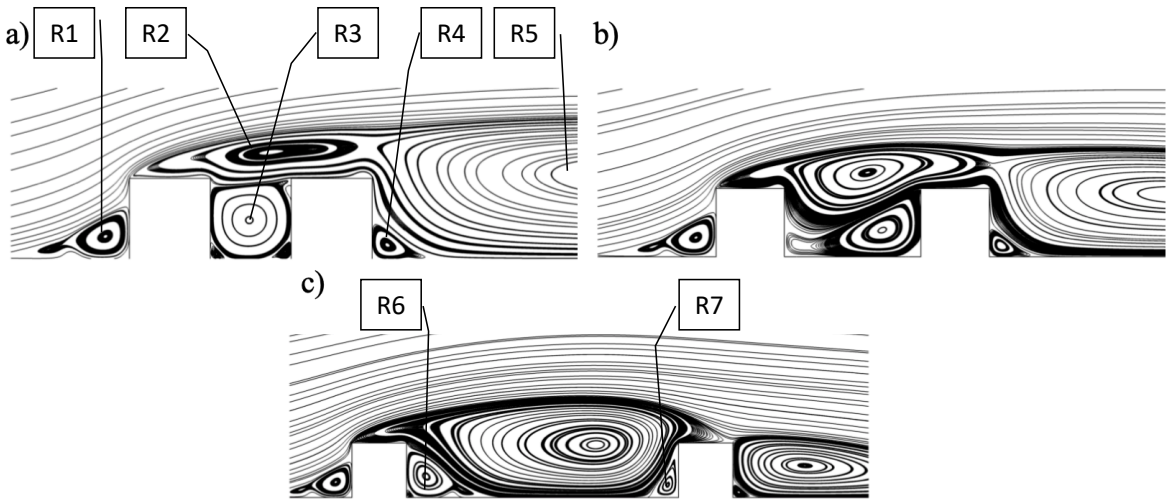

Figure 6.11 Time-averaged streamlines over wall-mounted squares in tandem with gap ratios of: a) $G/D = 2$, b) $G/D = 3$ and c) $G/D = 6$

Figure 6.12 shows the whole domain of interest with $G/D = 2, 3, 6, 10$ and 14 for the squares in tandem. It can be observed that R6 and R7 have been reduced significantly in size when increasing G/D to 10 and 14. The long downstream R5 behind Square 2 also decreases in size

due to its position downstream of Square 1 with large G/D. This is because the turbulent shear layers above R2, formed at the left top corner edge at Square 1, no longer reaches past Square 2 and affects R5 as seen Figure 12 (d) and (e). This subsequently leads to a highly reduced velocity profile over Square 2 which can be linked to the pressure and velocity contours discussed in Chapter 6.3.1 and Chapter 6.4.1, respectively.

a)

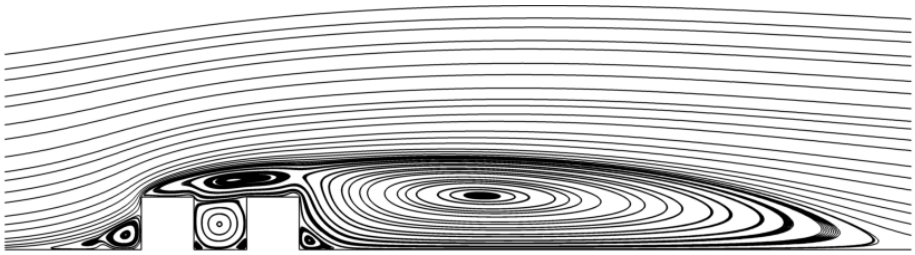

b)

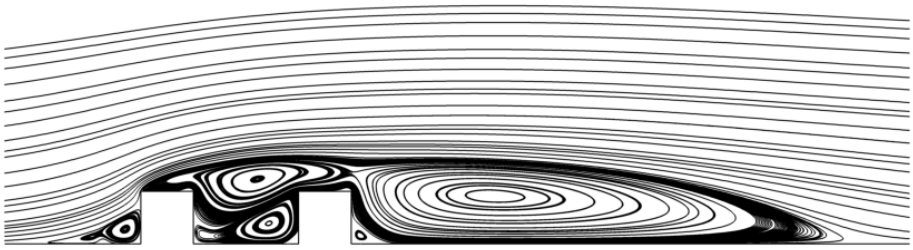

c)

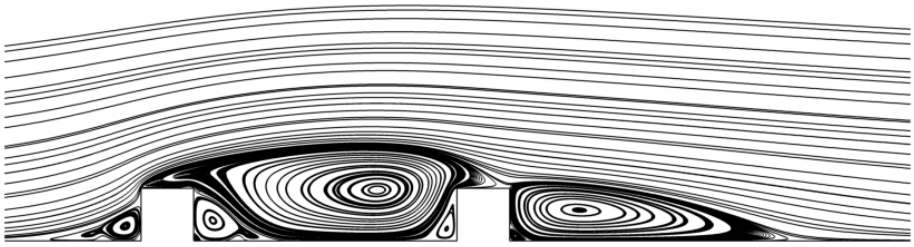

d)

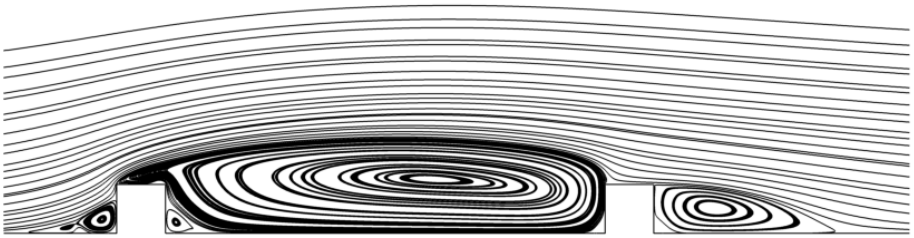

e)

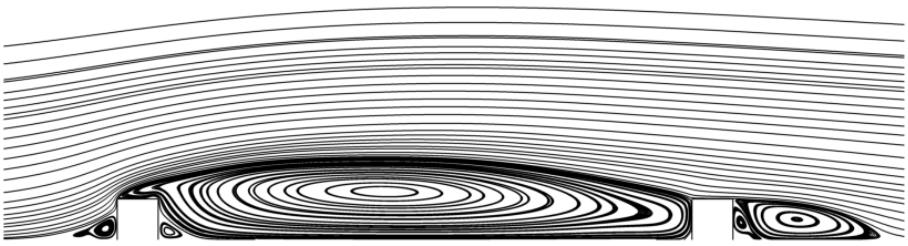

Figure 6.12 Streamlines for wall-mounted squares in tandem with gap ratios of: a) $G/D = 2$, b) $G/D = 3$, c) $G/D = 6$, d) $G/D = 10$ and $G/D = 14$

6.5.2 Streamlines over trapezoids in tandem

Figure 6.3 and Figure 6.4 shows the streamlines for all trapezoidal configurations in tandem with G/D of 6 and 14, respectively. With $G/D = 6$, the R6 and R7 are suppressed with increasing α. R2 recirculates over the top of Structure2 when $\alpha < 45°$, however for larger α, R2 seem to be shaped according to the gap shape between the two structures and is attached to its surrounding walls, as seen in Figure 6.3 (e).

The gap shape trend seems to be followed with $G/D = 14$ when α is 0° and 15°, but there is a steady drop in R2´s attachment to the front face of Structure 2 with increasing α, as clearly seen in Figure 6.14 (d) and (e). This is obviously due to the reason that the reduced high-speed region above the structures for larger α has not reach Structure 2. Finally, R5 is increasing in size in the streamwise direction with increasing α, clearly seen in Figure 6.14.

a)

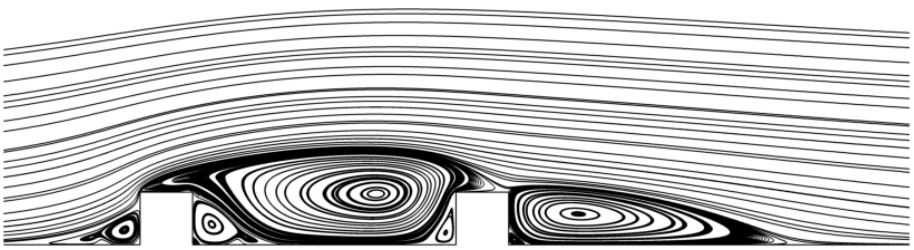

b)

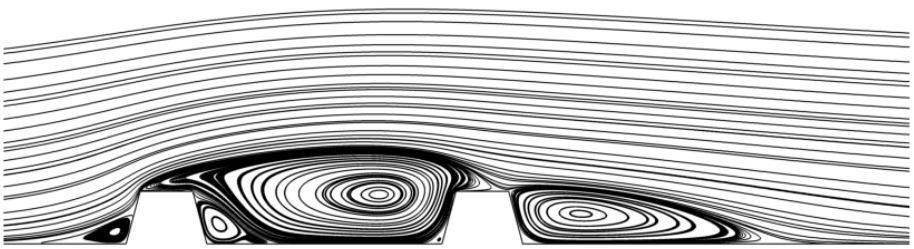

c)

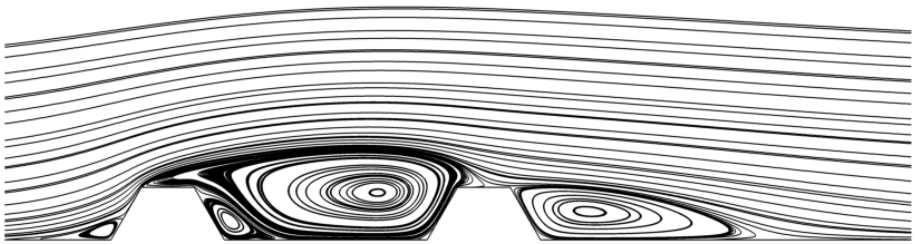

d)

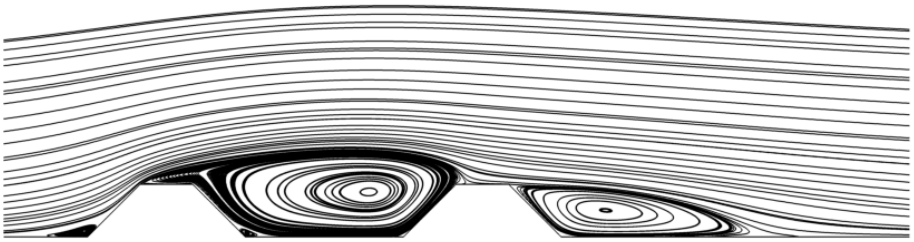

e)

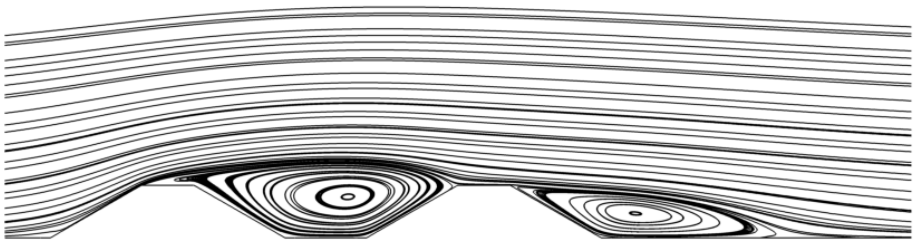

Figure 6.13 Streamlines for G/D = 6 for varying trapezoidal configurations α: (a) 0°, (b) 15°, (c) 30°, (d) 45° and (e) 60°

a)

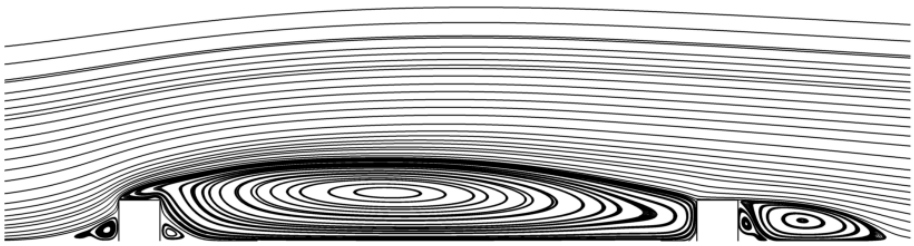

b)

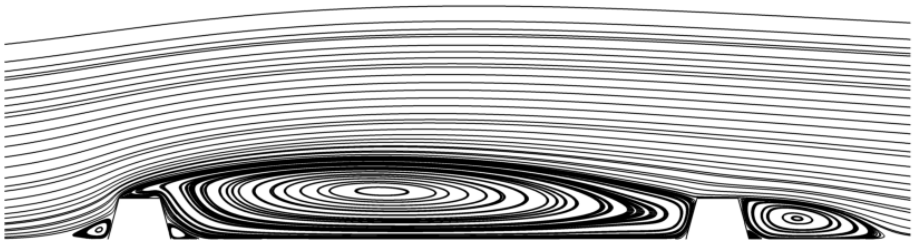

c)

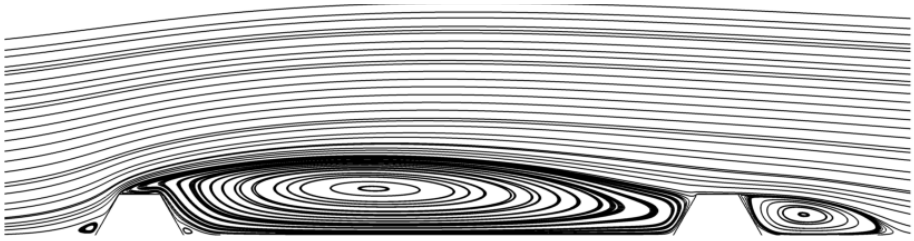

d)

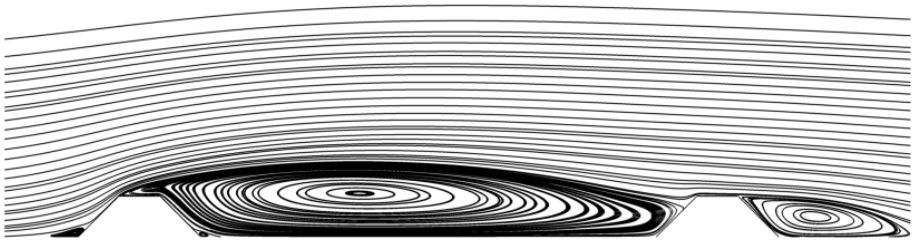

e)

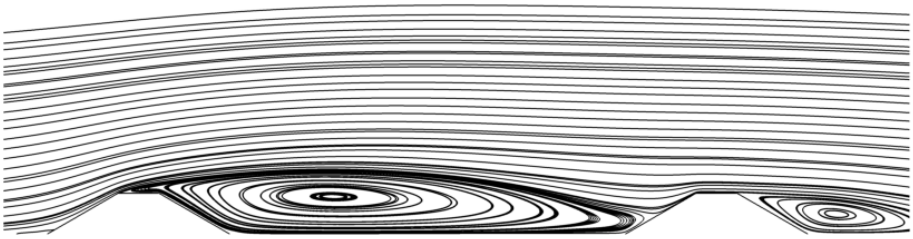

Figure 6.14 Streamlines for G/D = 14 for varying trapezoidal configurations α: (a) 0°, (b) 15°, (c) 30°, (d) 45° and (e) 60°

7 Conclusions

This chapter outlines the conclusions and main findings for the study on the single and tandem cases. It also discusses the possibilities of future work on the concept of square and trapezoidal structures in both single and tandem configurations.

7.1 Structures in single configuration

Two-dimensional numerical simulations of turbulent boundary layer flows at high Reynolds numbers around square and trapezoidal wall-mounted structures have been carried out. The effects of different bottom angles of the trapezoids on hydrodynamical quantities have been investigated. The simulations are based on RANS equations using the $k-\omega$ SST model combined with a wall function. The resulting drag coefficient (C_D) at $Re = 1.19 \times 10^5$ shows good agreement with that of experimental data. The horizontal velocity profiles at different locations near the square match well with those from the experiments (Liu et al., 2008) except that there is overprediction near the free stream because of the $k-\omega$ SST model. The validation shows that the present numerical model can provide satisfying results when used to study the hydrodynamic characteristics of different wall-mounted structures subjected to a boundary layer flow. Main conclusions can be outlined as follows:

1. The hydrodynamic quantities C_D , C_L and x_R/D all decrease with increasing α for trapezoidal configurations.
2. The main contribution of drag forces on the structures comes from the pressure difference between the front and back face of the structures. However, as α decreases, the viscous drag becomes more significant on the total drag.
3. The vortices on the back and front face of the structures dissipates with increasing angle of α.
4. The absolute minimal value of the bed shear stress is highest for the square configuration and lowest for α = 60°.

7.2 Structures in tandem configuration

Two-dimensional numerical simulations of turbulent boundary layer flows at $Re = 1.19 \times 10^5$ around square and trapezoidal wall-mounted structures in tandem have been carried out. The effects of the trapezoidal shape and the gap ratio G/D on hydrodynamic quantities for both structures in tandem have been investigated. The simulations are based on RANS equations using the $k - \omega$ SST model combined with a wall function. Main conclusions can be outlined as follows:

1. The most critical region, in terms of drag forces on both structures in tandem is found at $G/D = 6$.
2. The drag coefficient of Square 1 have negligble effect from the tandem Square 2 when $G/D = 14$.
3. The drag coefficient for Structure 2 shifts from negative to positive with $G/D = 14$ at $\alpha = 15°$
4. The strength of the negative pressure region between Square 1 and Square 2 increases from $2 < G/D < 6$ and decreasing from $6 < G/D < 14$.

7.3 Future work

Studies of flow around wall-mounted squares and trapezoids in single and tandem configurations are of great interest for several offshore applications. The present study used the $k - \omega$ SST model with the simpleFoam solver, but other simulation set ups could also be utilized. The velocity, pressure and streamlines contours would be interesting to compare to other turbulence models and numerical setups to study the discrepancies. Also comparing the present study to a 3D – simulation could observe the importance of the 3D effects of such flow problems.

The present simulations have proved to recreate reasonable hydrodynamic coefficients using low computational cost. It could efficiently be further used to investigate more configurations of G/D and α, and predict coefficients and flow behaviors for engineering purposes.

The results found in this study indicates that there are some critical configurations which would impose significant changes to the force on the subsea covers relative to other configurations, especially at $G/D = 6$ for the present flow conditions. Being able to properly predict the most

favorable configurations, both for single and tandem arrangement,would lead to an improved safety for operations with thesubsea equipment protected by the subsea covers.

References

Adams, E. W., and J. P. Johnston. "Effects of the separating shear layer on the reattachment flow structure part 2: Reattachment length and wall shear stress." *Experiments in Fluids* 6.7 (1988): 493-499.

ARIE, Mikio, et al. "Flow over rectangular cylinders immersed in a turbulent boundary layer: Part 2 flow patterns and pressure distributions." *Bulletin of JSME* 18.125 (1975): 1269-1276.

Brørs, B. "Numerical modeling of flow and scour at pipelines." *Journal of hydraulic Engineering* 125.5 (1999): 511-523.

Cengel, Y. A. and J. M. Cimbala. Fluid Mechanics: Fundamentals and Applications. McGraw-Hill Higher Education. (2017)

Clancy, Laurence Joseph. *Aerodynamics*. Halsted Press, 1975.

Coles, Donald. "The law of the wake in the turbulent boundary layer." *Journal of Fluid Mechanics* 1.2 (1956): 191-226.

Dai, Yukun, Hong Wang, and Cai Tian. "Numerical Simulations of Turbulent Flow Over Two Surface-Mounted Tandem Square Cylinders." *ASME 2017 36th International Conference on Ocean, Offshore and Arctic Engineering*. American Society of Mechanical Engineers, 2017.

Jasak, Hrvoje. "Error analysis and estimation for the finite volume method with applications to fluid flows." (1996).

Kleinstreuer, Clement. *Engineering fluid dynamics: an interdisciplinary systems approach*. Cambridge University Press, (1997).

Liu, Y. Z., F. Ke, and Hyung Jin Sung. "Unsteady separated and reattaching turbulent flow over a two- dimensional square rib." *Journal of Fluids and Structures* 24.3 (2008): 366-381.

Martinuzzi, R., and C. Tropea. "The flow around surface-mounted, prismatic obstacles placed in a fully developed channel flow." *Transactions-American Society of Mechanical Engineers Journal of Fluids Engineering* 115 (1993): 85-85.

Menter, Florian R., Martin Kuntz, and Robin Langtry. "Ten years of industrial experience with the SST turbulence model." *Turbulence, heat and mass transfer* 4.1 (2003): 625-632.

Menter, Florian R. "Two-equation eddy-viscosity turbulence models for engineering applications." *AIAA journal* 32.8 (1994): 1598-1605.

Meroney, Robert N., and David E. Neff. "Wind effects on roof-mounted solar photovoltaic arrays: CFD and wind-tunnel evaluation." *The Fifth International Symposium on Computational Wind Engineering (CWE 2010)*. 2010.

Nielsen, Anders Wedel, et al. "Flow and bed shear stresses in scour protections around a pile in a current." *Coastal Engineering* 72 (2013): 20-38.

Nymo, Dennis Alexander. *Numerical Simulation of Boundary Layer Flow Around Simplified Subsea Structures*. MS thesis. NTNU, 2015.

Ong, Muk Chen, et al. "Numerical simulation of flow around a circular cylinder close to a flat seabed at high Reynolds numbers using ak–ε model." *Coastal Engineering* 57.10 (2010): 931-947.

Robertson, E., et al. "Validation of OpenFOAM numerical methods and turbulence models for incompressible bluff body flows." *Computers & Fluids* 123 (2015): 122-145.

Ryu, D. N., Do Hyung Choi, and V. C. Patel. "Analysis of turbulent flow in channels roughened by two- dimensional ribs and three-dimensional blocks. Part I: Resistance." *International Journal of Heat and Fluid Flow* 28.5 (2007): 1098-1111.

Sanz-Serna, Jesús M., and Marc N. Spijker. "Regions of stability, equivalence theorems and the Courant-Friedrichs-Lewy condition." *Numerische Mathematik* 49.2-3 (1986): 319-329.

Tauqeer, Muhammad Ahmad, Zhong Li, and Muk Chen Ong. "Numerical simulation of flow around different wall-mounted structures." *Ships and Offshore Structures* 12.8 (2017): 1109-1116.

Versteeg, Henk Kaarle, and Weeratunge Malalasekera. *An introduction to computational fluid dynamics: the finite volume method*. Pearson education, 2007.

Zhao, X. F., Li, L., Ba, Q., & Ou, J. P. (2012). Scour monitoring system of subsea pipeline using distributed Brillouin optical sensors based on active thermometry. *Optics & Laser Technology*, *44*(7), 2125-2129.

APPENDIX A

Numerical Simulations of Flow Around Subsea Covers at High Reynolds Numbers

Martin Andersen[a], Guang Yin[1a], Muk Chen Ong[a]

[a]Department of Mechanical and Structural Engineering and Material Sciences, University of Stavanger, Stavanger, Norway

Abstract:

In the present study, the flow around symmetric trapezoidal wall-mounted subsea covers with different bottom angles subjected to a boundary layer flow at Reynolds numbers of 1.19×10^5 and 1×10^6 (based on the height of the structures and the free stream velocity) is under investigation using Reynolds-averaged Navier-Stokes (RANS) equations combined with the $k - \omega$ Shear Stress Transport (SST) turbulence model. It is found that the drag coefficient on the wall-mounted square structures using the $k - \omega$ SST turbulence model is in good agreement with the experimental data. The effects of bottom angles on the hydrodynamic quantities and the flow field around the structures have been discussed.

1. Introduction

Wall-mounted square and trapezoidal shaped rib structures are studied due to their wide application in offshore technology such as protection covers for pipelines. These structures are regularly subjected to extreme subsea environmental conditions and at a typical Reynolds number of $300 < Re < 3 \times 10^5$ (sub-critical) and $Re > 4 \times 10^6$ (transcritical). Here $Re = U_\infty D/\nu$ where U_∞ is the free stream velocity and D is the structure height and ν is the kinematic viscosity of the fluid. Flows around these structures are complex and depend on various parameters such as Reynolds number, normalized boundary layer thickness δ/D (δ is the incident boundary layer thickness) and the shape of the structures.

Many experimental and numerical studies have been carried out to investigate the flow around wall mounted structures at high Reynolds numbers. Arie et al. (1975) conducted experimental studies of the pressure distribution around square structures subjected to a turbulent boundary layer at Reynolds numbers $3.41 \times 10^4 < Re < 1.19 \times 10^5$. Tauqeer et al. (2017) conducted a numerical study for flows around subsea covers with different geometries subjected to different δ/D at $Re = 1 \times 10^6$. The study presented reasonable results compared to the experimental data (Arie et al. 1975) using the $k - \varepsilon$ turbulence model. Hydrodynamic quantities on wall-mounted structures with different geometries were also investigated. Meroney R. N (2010) conducted validation studies on turbulence models for flows over wall-mounted panels. The study found that

[1] Corresponding author.
E-mail address: guang.yin@uis.no (Guang Yin)

the k-ω turbulence model is sufficient to reproduce consistent hydrodynamic quantities with the experimental data. Martinuzzi et al (1993) investigated flow over square ribs with varying spanwise lengths W/D (W is the spanwise length of the rib structures and D is the height of the structures) using experiments. The study found that the flow around rib structures with W/D >10 can be considered as two-dimensional. Liu et al. (2008) studied the spatio-temporal characteristics of the separation and reattachment of turbulent flows over a two-dimensional square rib at $Re = 1.32 \times 10^4$ with $\delta/D = 0.75$. Synchronized measurements of fluctuating pressure and velocity were obtained by using microphone arrays and a split-fiber film. The study showed that the shear layer separates from the leading edge of the rib, sweeps past the rib and reattaches on the bottom wall with a distance of $x_R/D = 9.75$ from the rib. Ryu et al. (2007) investigated the characteristics of turbulent channel flow over two-dimensional rib structures at $Re = 2 \times 10^4$ employing Reynolds Averaged Navier-Stokes Equations and the $k - \omega$ turbulence model. The structures in the study were square, triangular, semicircular and wavy wall (sinusoidal function shaped). It was found that the square shaped structure imposed the most resistance to the incoming flow while the wavy wall offered the least. The results were in good agreement with experimental data and the RANS $k - \omega$ turbulence model was found to capture the essential features of flow over wall-mounted strucures.

The literature review shows that flow around wall-mounted structures has been studied in experiments for high Reynolds numbers and by RANS equations with the $k - \varepsilon$ and the $k - \omega$ turbulence models. To the authors knowledge, the hydrodynamic effects of varying trapezoidal configurations have not been studied using 2D RANS equations with $k - \omega$ SST turbulence model. In an economical point of view RANS is preferred over Direct Numerical Simulation (DNS) and Large Eddy Simulation (LES) due to computational cost as well as giving reasonable accuracy. In the present study RANS simulations with $k - \omega$ SST model have been carried out to obtain the hydrodynamic quantities such as; drag coefficient (C_D), lift coefficient (C_L) and recirculation length (x_R/D), for symmetric trapezoidal wall-mounted strucures with different bottom angles ($90° - \alpha$) at $Re = 1.19 \times 10^5$ and $Re = 1.0 \times 10^6$. Here $C_D = F_D/0.5\rho A U_\infty^2$, where F_D is the steady state drag force in the streamwise direction, ρ is the fluid density and A is the projected area. $C_L = F_L/0.5\rho A U_\infty^2$, where F_L is the steady state lift force in the cross-stream direction.

The numerical setup used in this study is validated against the experimental data of Arie et al. (1975) and numerical results of Tauqeer et al. (2017) for square configuration with $\delta/D = 0.73$ at $Re = 1.19 \times 10^5$. The paper is organized as follows. First, the mathematical formulation, numerical methods as well as convergence studies are given in Section 2. The results and discussions are presented in Section 3. Finally, conclusions are given.

2. Mathematical formulation

2.1. Flow model

The Reynolds-averaged equations for conservation of momentum and mass are expressed as:

$$\frac{\partial u_i}{\partial x_i} = 0 \tag{1}$$

$$\frac{\partial u_i}{\partial t} + u_j \frac{\partial u_i}{\partial x_j} = \frac{-1}{\rho}\frac{\partial P}{\partial x_i} + \nu \frac{\partial^2 u_i}{\partial x_j^2} - \frac{\partial \overline{u_i{}' u_j{}'}}{\partial x_j} \tag{2}$$

where $i, j = 1,2$ (for x,y) denote the streamwise and cross-stream directions, respectively; u_1 and u_2 (for u and v) are the corresponding mean velocity components. $\overline{u_i{}' u_j{}'}$ is the Reynold stress component and $u_i{}'$ represents the fluctuating part of the velocity, P is the pressure and ρ is the fluid density.

The $k - \omega$ SST turbulence model (Menter, 1994) is employed in the present study. The SST model is a combination of the $k - \omega$ and the $k - \varepsilon$ model. The near wall region of the domain is treated with the $k - \omega$ model of Wilcox (1998) while the standard $k - \varepsilon$ model of Jones and Launder (1973) is used in the outer wake region and in the free shear layers. According to Menter et al. (2003), the equations of k and ω can be expressed as follow:

$$\frac{D(\rho k)}{Dt} = \widetilde{P_k} - \beta^* \rho \omega k + \frac{\partial}{\partial x_j}\left[(\mu + \sigma_k \mu_t)\frac{\partial k}{\partial x_j}\right] \tag{3}$$

$$\frac{D(\rho \omega)}{Dt} = \alpha \rho S^2 - \beta \rho \omega^2 + \frac{\partial}{\partial x_j}\left[(\mu + \sigma_\omega \mu_t)\frac{\partial \omega}{\partial x_j}\right] + 2(1 - F_1)\rho \sigma_{\omega 2}\frac{\partial k}{\partial x_j}\frac{\partial \omega}{\partial x_j} \tag{4}$$

where $\widetilde{P_k}$ is expressed by

$$\widetilde{P_k} = min\left[\mu_t \frac{\partial u_i}{\partial x_j}\left(\frac{\partial u_i}{\partial x_j} + \frac{\partial u_j}{\partial x_i}\right), 10\beta^* \rho \omega k\right] \tag{5}$$

Φ_1 represents any constant in the original $k - \omega$ model (σ_{k1}, …) and Φ_2 represents any constant in the original $k - \varepsilon$ model (σ_{k2}, ...). Then the constant Φ of the new model is denoted as

$$\Phi = F_1 \Phi_1 + (1 - F_1)\Phi_2 \tag{6}$$

$$F_1 = tanh\,(arg_1^4) \tag{7}$$

$$arg_1 = min\left[max\left(\frac{\sqrt{k}}{\beta^* \omega y}, \frac{500\nu}{y^2 \omega}\right)\frac{4\rho \sigma_{\omega 2} k}{CD_{k\omega} y^2}\right] \tag{8}$$

$$CD_{k\omega} = max\left(2\rho \sigma_\omega \frac{1}{\omega}\frac{\partial k}{\partial x_j}\frac{\partial \omega}{\partial x_j}, 10^{-10}\right) \tag{9}$$

where y is the distance to the closest wall. $CD_{k\omega}$ is the positive portion of the cross-diffusion term in (4).

The turbulent eddy viscosity is defined as

$$\nu_t = \frac{a_1 k}{max(a_1 \omega, SF_2)} \tag{10}$$

where S is the invariant measure of the strain rate and F_2 is given as

$$F_2 = tanh(arg_2^2), \tag{11}$$

$$arg_2 = max\left(2\frac{\sqrt{k}}{0.09\omega y}, \frac{500\nu}{y^2 \omega}\right) \tag{12}$$

The SST constants are: $\beta^* = 0.09$, $\alpha_1 = 0.5532$, $\alpha_2 = 0.4403$, $\beta_1 = 0.075$, $\beta_1 = 0.0828$, σ_{k2}= 1.0 and $\sigma_{\omega 1}$= 0.5, $\sigma_{\omega 2}$ = 0.85616.

2.2. Numerical Simulation Scheme, computational domain and boundary conditions

OpenFOAM, an open source computational fluid dynamic (CFD) code, is used in the present study. A solver based on semi-implicit method for pressure linked equations, simpleFoam is used. The spatial schemes for gradient, Laplacian and divergence are Gauss linear, bounded Gauss linear upwind, and Gauss linear limited corrected, respectively.

The origin of the coordinates is located at the bottom center of the wall mounted structure. The height and top length of the structure is D and the bottom angels of the trapezoidal structures are $90° - \alpha = 90°(\text{square}), 75°, 60°, 45°$and $30°$ as denoted in Figure 1. The length and height of the computational domain are $52D$ and $20D$, respectively. The flow inlet boundary is located Lu upstream from the center of the structure and the flow outlet boundary is located Ld downstream from the center of the structure. Ong et al. (2010) performed a numerical study of flow around circular cylinder close to a flat seabed at the same Reynolds number range as the present study and found that a computational domain with $(Lu, Ld) = (10D, 20D)$ is sufficient to suppress any far-field effects on the structures. In the present study, Lu is set to be $11.5D$ and Ld is set to be $40.5D$ to ensure that the domain is large enough. The boundary conditions for the simulations are set as follows:

(1) The inlet velocity is a logarithmic boundary layer flow, with a horizontal velocity profile, adapted from the experiments done by Arie et al (1975) to ensure similarity to the experimental set up for comparisons. The velocity profile is used throughout the study. The velocity in y direction is set to be zero and the value of k and ω is calculated as follows:

$$k(y) = max\left\{C_\mu^{\frac{-1}{2}}\left(1 - \frac{y}{\delta}\right) \times \left|1 - \frac{y}{\delta}\right| u^{*2}, 0.0001U_\infty^2\right\} \tag{13}$$

$$\omega = \frac{k^{0.5}}{C_\mu^{0.5} l} \tag{14}$$

$$l = min\left\{\kappa y\left(1 + 3.5\frac{y}{\delta}\right)^{-1}, C_\mu \delta\right\} \tag{15}$$

where $C_\mu = 0.09$ is the turbulent-viscosity constant, u^* is the bottom wall friction velocity, $\kappa = 0.41$ is the Karman constant and l is the turbulent length scale (see e.g Brørs, 1999; Ong et al. 2010).

(2) No-slip condition ($u_1 = u_2 = 0$) and standard near-wall conditions for k and ω is applied on the surface of the structures and the bottom wall. When using these near-wall functions, the criteria of $y^+ > 30$ must be satisfied and y^+ is given as:

$$y^+ = \frac{\Delta y u^*}{\nu} \tag{16}$$

where Δy is the distance of the first grid away from the wall.

(3) At the outlet, u_1, u_2, k and ω are specified as zero gradient and the pressure is set as zero.

(4) At the top, u_1, u_2, k and ω are set as zero gradient.

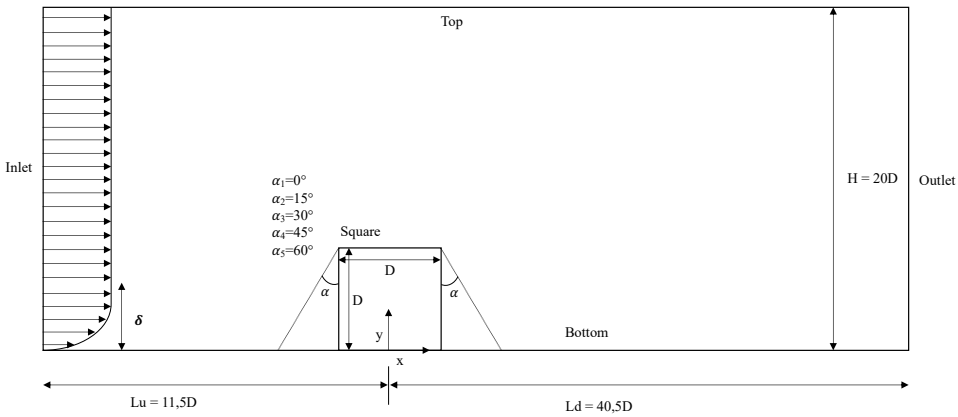

Figure 1. Computational domain and boundary conditions

2.3. Grid resolution Study

The grid resolution study has been carried out for all five angles ($\alpha = 0°, 15°, 30°, 45°$ and $60°$) at $Re = 1.19 \times 10^5$ and $Re = 1.0 \times 10^6$ for $\delta/D = 0.73$. The variations of C_D, C_L and x_R/D are obtained and presented in Table 1 and 2. C_D and C_L are calculated directly from F_D and F_L which are computed from the total force acting on the surface of the structures. x_R/D is the horizontal distance between the separation point at the top left corner of the structures and the point where the bottom wall shear stress changes its sign in the wake region. Results for the convergence studies for $Re = 1.19 \times 10^5$ are also shown with variation of the grid numbers for C_D, C_L and x_R/D in Figure 2.

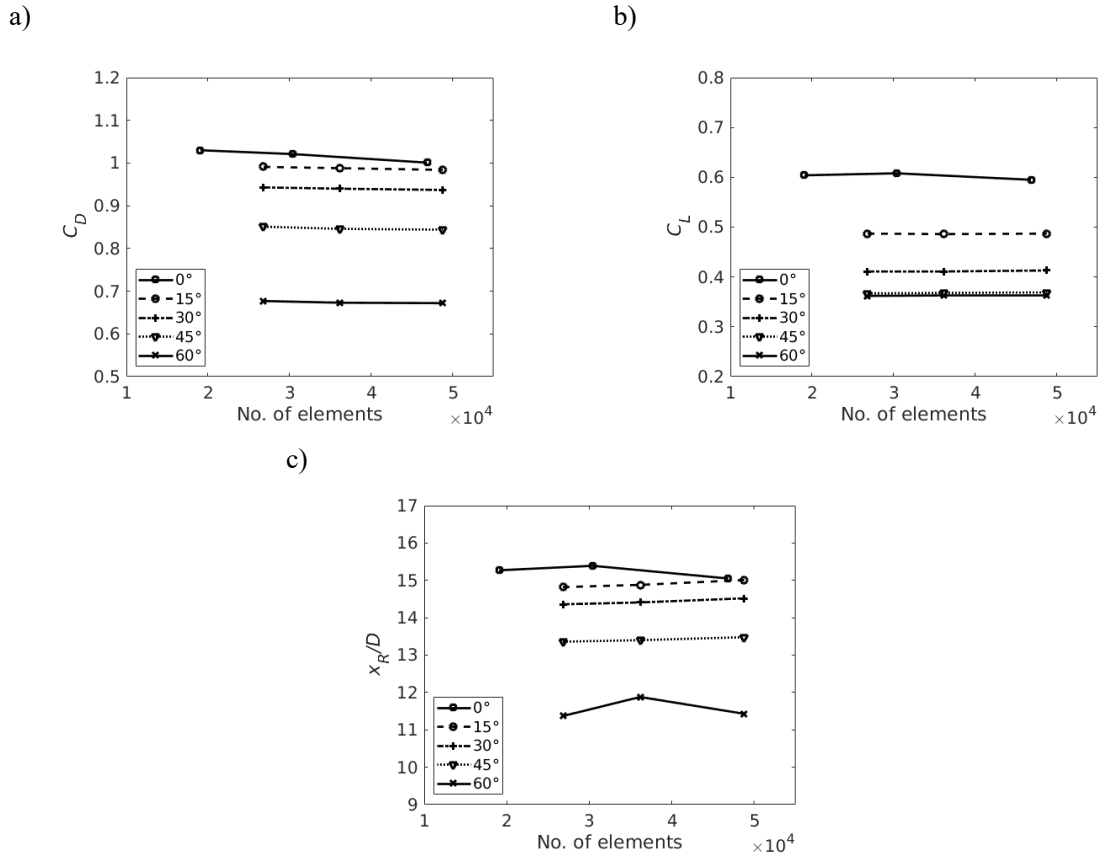

Figure 2. Convergence of trapezoidal configurations at Re $= 1.19 \times 10^5$

For different mesh densities at $Re = 1.19 \times 10^5$, the difference of C_D between the cases varies from 0.14% to 1.99%. The relative difference of C_L is from 0.16% to 2.18% and the relative difference of x_R/D varies from 0.59% to 2.23%. For different mesh densities at $Re = 1.0 \times 10^6$, the relative difference of C_D between cases alters between 0.09% and 1.09%. The relative difference of C_L varies between 0.3% and 4.86% and that for x_R/D alters between 3.24% and 6%. Therefore, the normal mesh densities for both square and trapezoid cases at the two Reynolds numbers have achieved sufficient grid resolutions.

Since wall functions are applied for all the simulations, a requirement of $y^+ > 30$ for the first grid above the wall needs to be satisfied. In the present study, y^+varies between 30 and 42 for different configurations at both Reynolds numbers. It can be concluded that grid resolutions for all configurations in the present study can provide satisfactory results. An example of the grid used for trapezoidal configurations is presented in Figure 3.

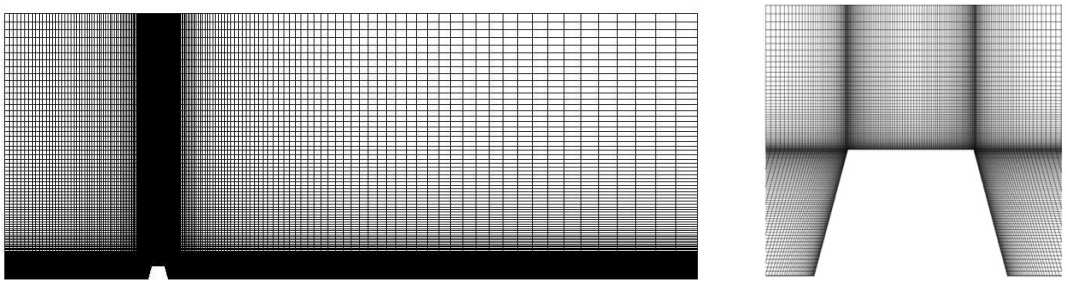

Figure 3. Grid structure for $\alpha = 15°$ and Re = 1 x 10^6

Mesh	α [°]	C_D	C_L	x_R/D
19076	0	1.030	0.604	15.27
30424	0	1.021	0.608	15.39
46531	0	1.001	0.595	15.05
26 800	15	0.991	0.487	14.82
36166	15	0.988	0.486	14.88
48789	15	0.984	0.487	15.01
26 800	30	0.943	0.411	14.36
36166	30	0.940	0.411	14.41
48789	30	0.937	0.413	14.62
26 800	45	0.851	0.367	13.36
36166	45	0.846	0.368	13.40
48789	45	0.844	0.369	13.48
26 800	60	0.677	0.362	11.57
36166	60	0.673	0.363	11.88
48789	60	0.672	0.363	11.43

Table 1. Hydrodynamic quantities for varying α with different grids at $Re = 1.19 \times 10^5$

Mesh	α [°]	C_D	C_L	x_R/D
39 360	0	1.115	0.624	16.90
53 124	0	1.125	0.657	16.83
85 824	0	1.113	0.655	16.10
39 360	15	1.070	0.488	16.52
56 124	15	1.060	0.504	16.28
98 244	15	1.059	0.507	15.77
39 360	30	0.997	0.410	15.64
56 124	30	0.990	0.417	15.71
98 244	30	0.987	0.438	14.82
39 360	45	0.874	0.369	14.22
56 124	45	0.869	0.380	14.20
98 244	45	0.870	0.399	13.60
39 360	60	0.653	0.389	11.42
56 124	60	0.646	0.386	11.54
98 244	60	0.639	0.406	11.06

Table 2. Hydrodynamic quantities for varying α with different grids at $Re = 1 \times 10^6$

3. Results and discussion

3.1. Validation study

Validation study is done by comparing the drag coefficient and the horizontal velocity profiles of the present study and those of the earlier numerical and experimental studies.

The drag coefficient was compared to experimental data from Arie et al. (1975) and numerical data from Tauqeer et al. (2017) using identical flow conditions of $\delta/D = 0.73$ at $Re = 1.19 \times 10^5$. The present study simulated $C_D = 1.00$, which is in good agreement with the previous results of $C_D = 0.96$ (Arie et al. 1975) and numerical data $C_D = 1.02$ (Tauqeer et al. 2017).

To further validate the simulation, a comparison of horizontal velocity profiles between experimental data from Liu et al. (2008) and the present study has also been performed. The experiment of Liu et al. (2008) was conducted at $Re = 1.32 \times 10^4$ with $\delta/D = 0.75$ and compared to the present simulation at $Re = 1.19 \times 10^5$ with $\delta/D = 0.73$. The horizontal velocity profiles are compared at six different locations along the computational domain shown in Figure 4. The velocity profile at the upstream location of $x/D = -3.5$ shows no negative part and it appears to be the same as the experimental profile. The velocity profile at the separation point $x/D = -0.5$ also appears to follow the experimental data, but has a slight overprediction region in the upper section of the velocity profile. This overprediction is also observed for the other four downstream locations and this may be due to the difference in Reynolds number. Furthermore, the overprediction of the velocity profiles compared with Tauqueer et al. (2017), where the $k - \epsilon$ turbulence model is used, may be due to the low dissipation by using the $k - \omega$ SST model in the present study. A small negative region in the velocity profiles appears at $x/D = 0.5$ on the top right corner of the square which shows the presence of an adverse pressure gradient. There is a large negative region close to the bottom wall in the velocity profiles downstream the square indicating that a recirculation zone has been developed. In general, the profiles show reasonable agreement with the experimental data.

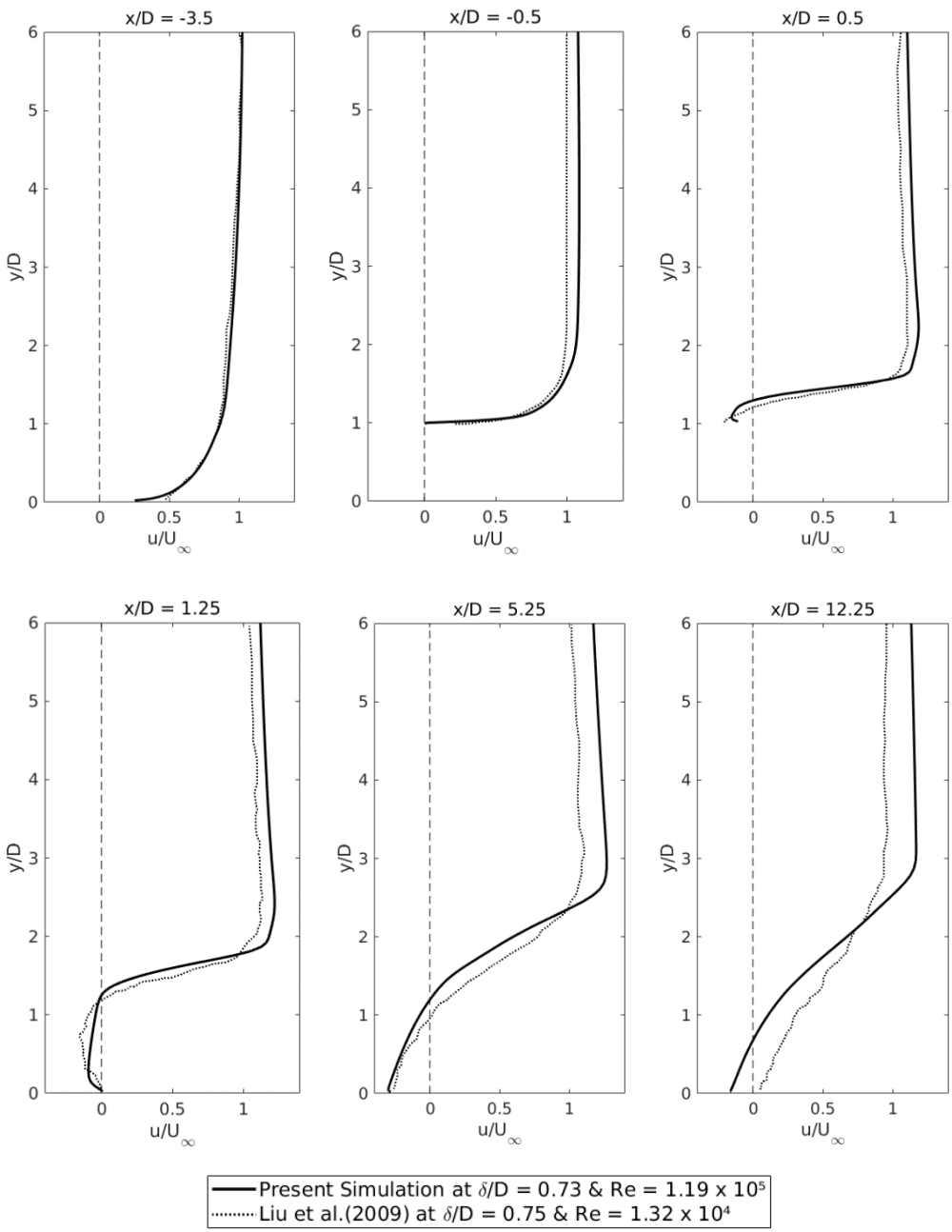

Figure 4. Comparisons of horizontal velocity profiles of the present simulation and experimental data from Liu et al. (2009)

3.2. Effect of α on hydrodynamic quantities and x_R/D

Varying angles $0° < \alpha < 60°$ have been studied at $Re = 1.19 \times 10^5$ and $Re = 1.0 \times 10^6$ to examine its effects on the hydrodynamic quantities: C_D, C_L and x_R/D.

As seen from Figure 5 (a), the drag coefficient is monotonically decreasing with increasing α. The physical explanation for the trend can be outlined as follows. The main contribution of the total drag is the pressure difference between the front and the back face of the structure. The block effect of structure becomes weak with increasing α, which results in less pressure difference. This can also be observed in the pressure

distribution in Figure 6. However, as α further increases, the contribution of the viscous drag increases and with $\alpha = 60°$ the trapezoid tends to be flat and a larger part of the total drag on the structures comes from the viscous drag. The viscous drag is higher at $Re = 1.19 \times 10^5$ and causes larger C_D than that at $Re = 1.0 \times 10^6$ for higher α as shown in Figure 5 (a). The recirculation length x_R/D, shown in Figure 5 (c), also decreases for increasing α and behaves similar to C_D. This implies that the viscous effect has a significant influence on these two quantities when the pressure contribution decreases.

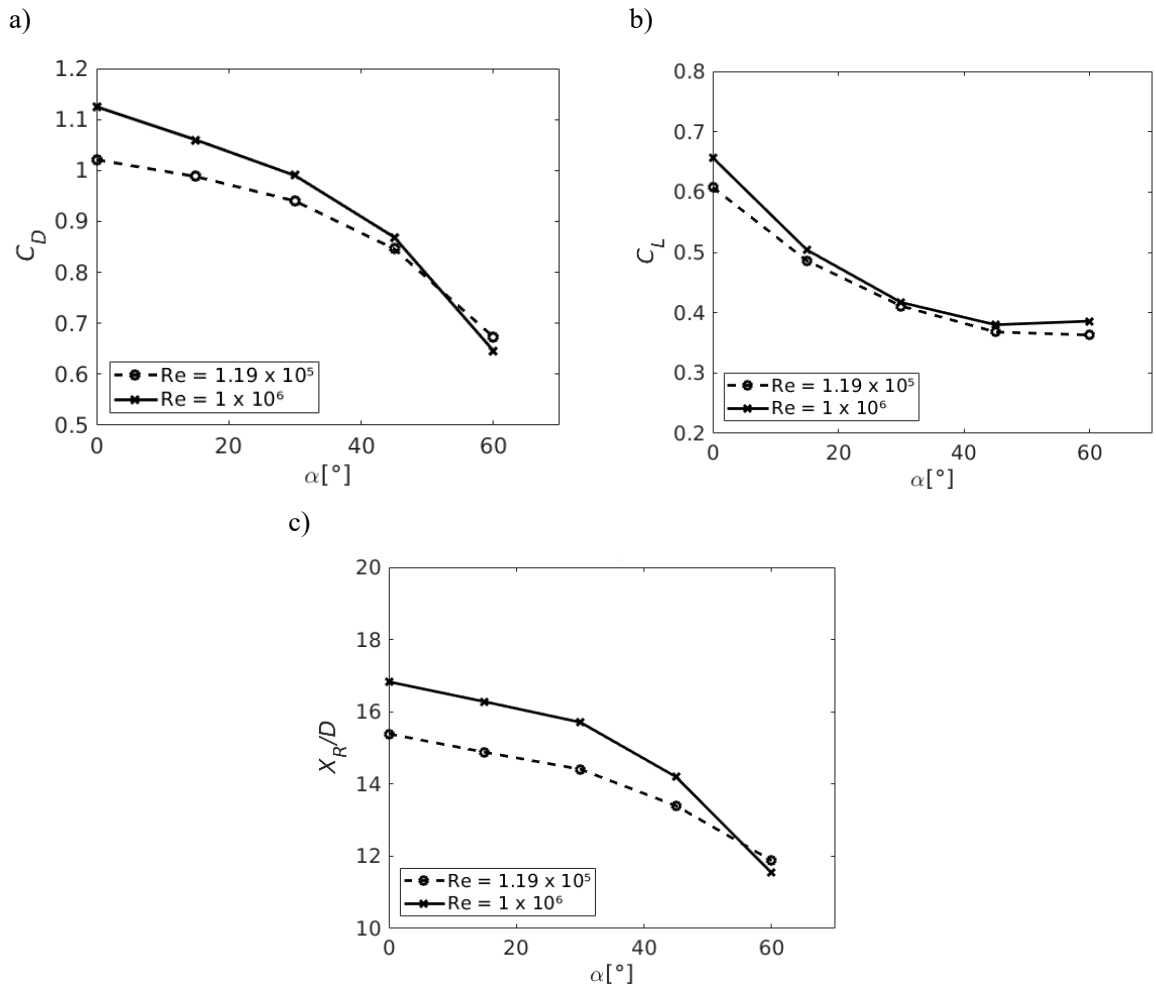

Figure 5. Effect of α on hydrodynamic quantities: (a) C_D, (b) C_L and (c) x_R/D

3.3 Velocity and Pressure Distributions

The color contours of the pressure at $Re = 1 \times 10^6$ are presented in Figure 6. Due to the block effect of the structures to the flow, there is a high-pressure region in front of the structure because of the energy conservation. Furthermore, due to the conservation of mass, a high-speed velocity region forms after the separation point above the structure. Hence, due to the Bernoulli's principle, the high-speed velocity region creates a local negative pressure region around the right top edge of the structure as seen in Figure 6. It can be observed that the intensities of both the positive and negative pressure regions reduces with increasing α. This is due to the fact that the reducing blocking effect, associated with higher α, causes lower velocity drop over the structure, hence resulting in reducing pressure regions due to the Bernoulli's principle.

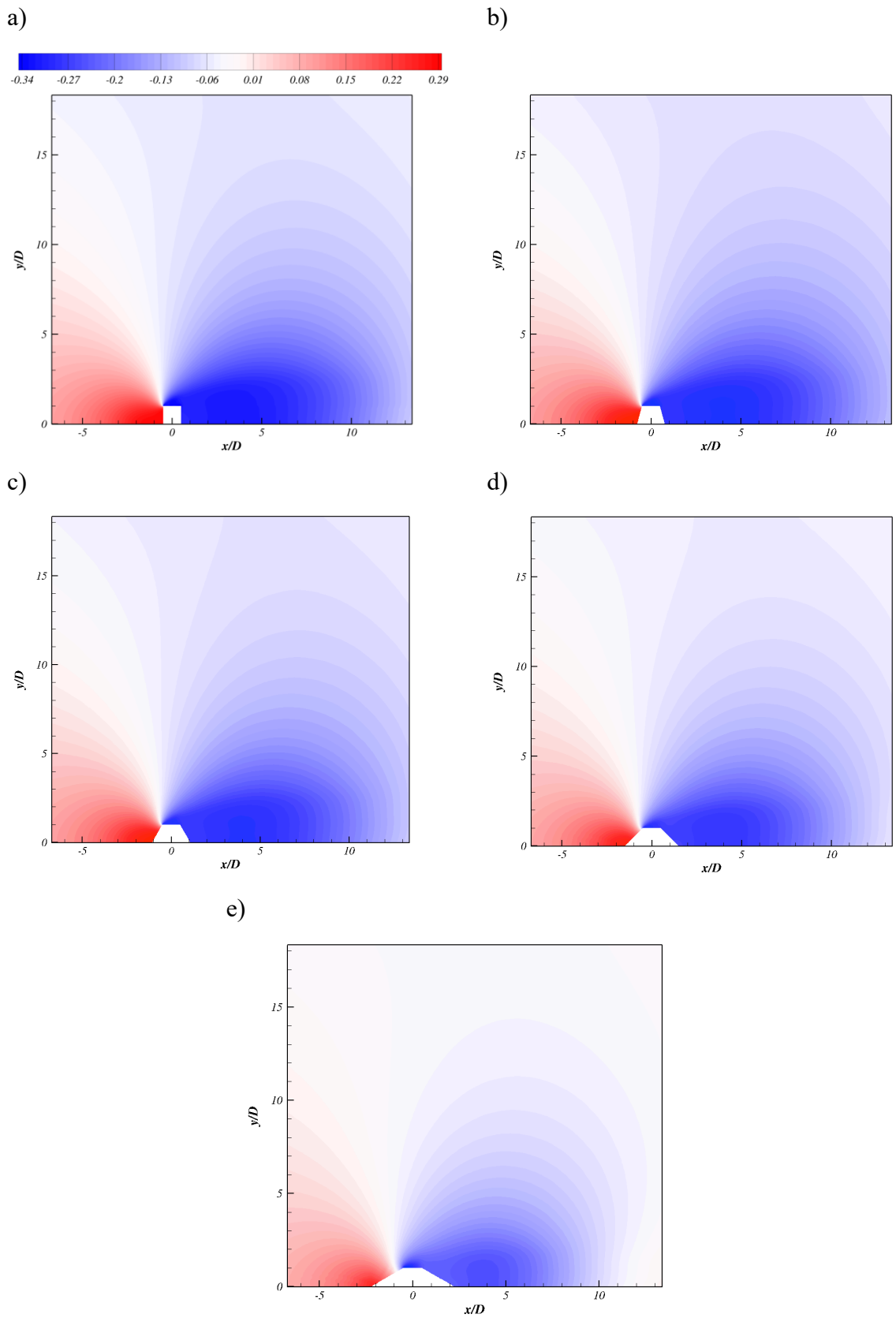

Figure 6. Pressure contours for $\mathrm{Re} = 1 \times 10^6$ for varying α: (a) 0°, (b) 15°, (c) 30°, (d) 45° and (e) 60°

The contours of the horizontal velocities at $Re = 1 \times 10^6$ are presented in Figure 7 for all α. The velocity at the front face of the structure is zero and propagates further upstream due to the blocking effect. After the separation point, at the top left corner of the structure, the velocity is accelerated due to the conservation of mass. A shear layer is generated with a high-speed region above the structure and a recirculation region behind the structure. The area of the high-speed region reduces with decreasing α.

a)

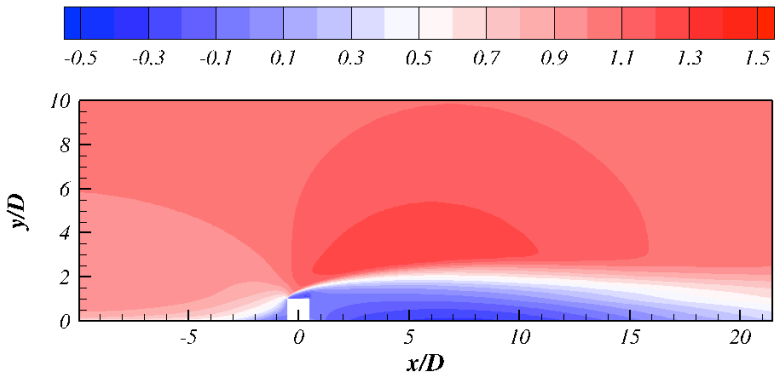

b)

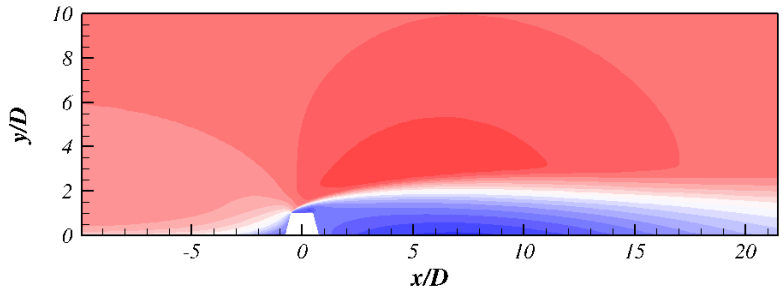

c)

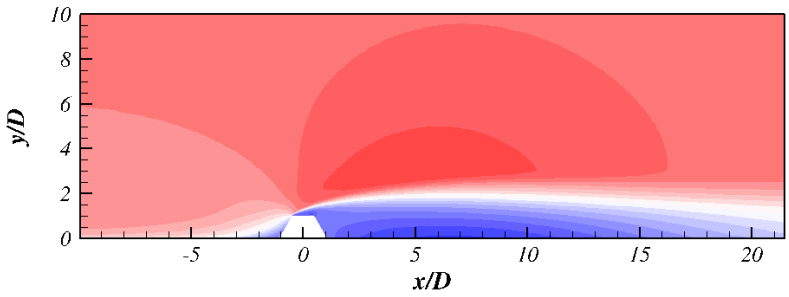

d)

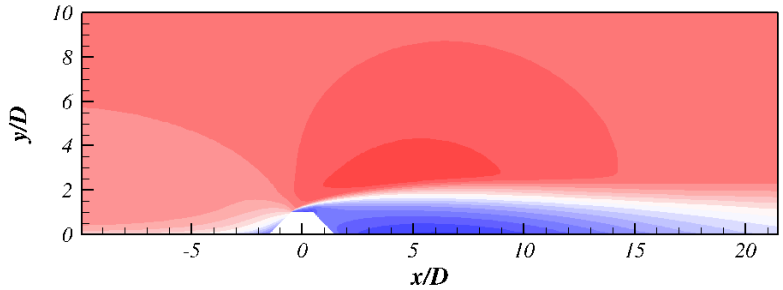

e)

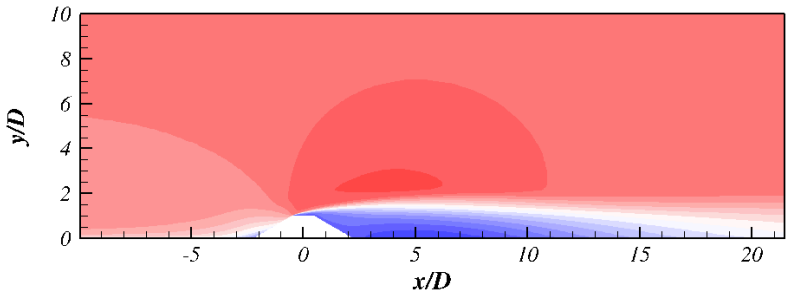

Figure 7. Horizontal velocity contours at Re $= 1 \times 10^6$ for varying α: (a) 0°, (b) 15°, (c) 30°, (d) 45° and (e) 60°

The contours of vertical velocity are presented in Figure 7 for all angles α. There is an increase in the vertical velocity along the front face of the structure due to the conservation of mass, accelerating the mass above and past the structure to maintain conservation of energy. The intensity of the high vertical velocity region around the top left corner reduces with increasing α, as seen in Figure 8 (b) - (e). This is because the trapezoidal structures shift the direction of the flow more gradually. There is also a slight positive vertical velocity region at the rear face of the structure, indicating that a recirculation region forms behind the structures.

a)

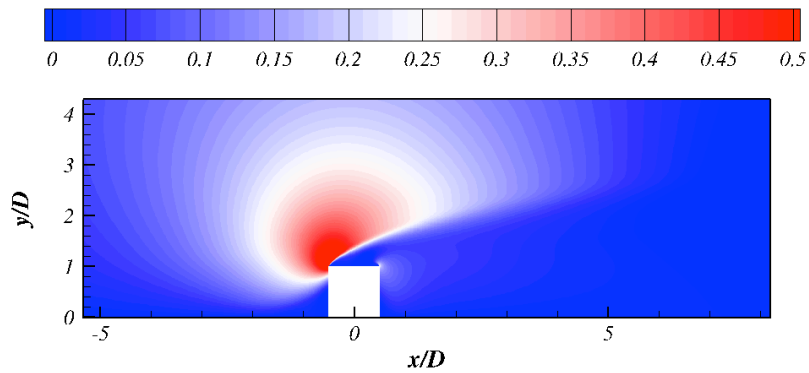

b)

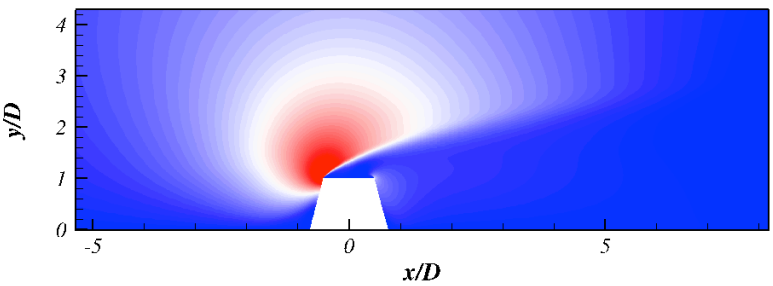

c)

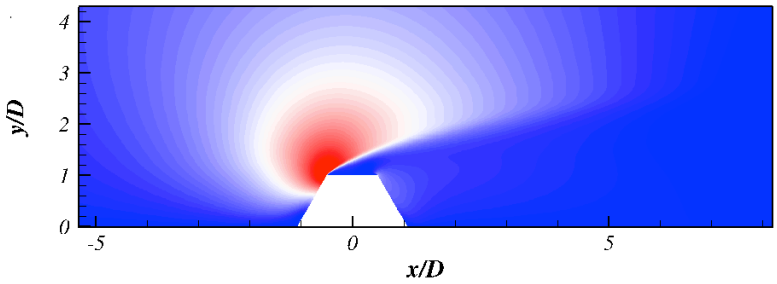

d)

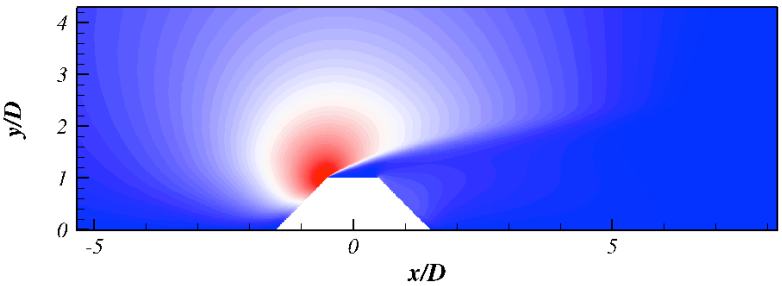

e)

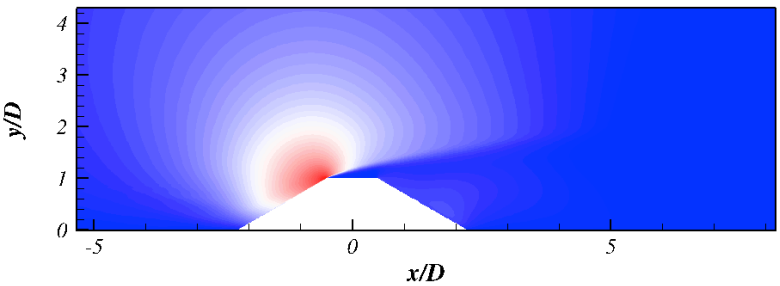

Figure 8. Vertical velocity contours at $\mathrm{Re} = 1 \times 10^6$ for varying α: (a) $0°$, (b) $15°$, (c) $30°$, (d) $45°$ and (e) $60°$

3.4. Bed shear stress and flow patterns

In actual subsea environment, bed shear stress is closely related to the scour process, which is removal of sediment around the base of an immerged structure. High absolute values of τ/τ_∞ close to the structure can indicate a significant scour process, which is a typical source for failures in subsea operations (Zhao et al. (2012)). Therefore, the present study investigates the bed shear stress on the seabed surfaces adjacent to the structures with different configurations of α.

a) b)

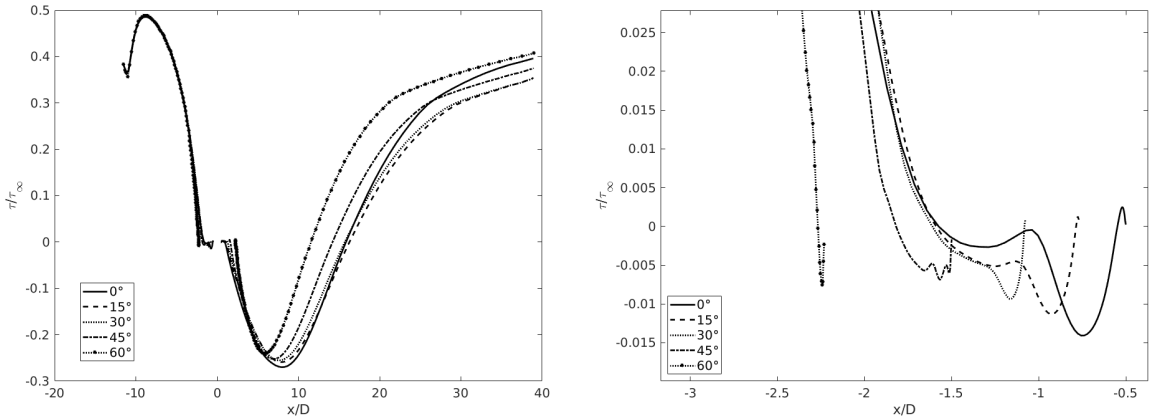

Figure 9. Bed shear stress along the bottom surface at $\mathrm{Re} = 1 \times 10^6$ for: a) the whole domain. b) the front face of the structures

Figure 9 shows the non-dimensional bed shear stress τ/τ_∞, where τ_∞ is the undisturbed bed shear stress, along the bottom wall surface. τ/τ_∞ stagnates towards zero close to the front faces of the structures which are located $x/D = (-0.5, -0.768, -1.077, -1.5, -1.732)$ for $\alpha = (0°, 15°, 30°, 45°, 60°)$, respectively. Figure 9 (b) shows small negative τ/τ_∞ regimes in front of the structure for all α due to the backflow and the adverse pressure gradient caused by the conservation of energy. It can be observed that these negative regimes have lower amplitudes and are shorter (in streamwise direction) for increasing α. This behavior is due to the smooth flow transitions which is associated with high α. The bed shear stress has a large negative region behind the structures due to the recirculation motions for all configurations. This negative region is also reduced with increasing α, which is consistent with the declining recirculation length. It is also worth noting that the absolute minimal value of the bed shear stress also decreases with increasing α and its location shifts closer to the structure.

To further investigate the flow around the five configurations with different α, streamlines are plotted at $Re = 1.19 \times 10^5$ and $Re = 1.0 \times 10^6$ in Figure 10, 11 and 12. There are three main recirculation motions: around the square structure seen in Figure 10. The first vortex (1) forms because the fluid particle hits the structure, flows downward and reverses its direction due to the bottom wall. A large recirculation is generated by the shear layer separation after the front top edge of the square (2), which also induces a smaller one in the downward corner of the square (3). For both Reynolds numbers, with increasing α, the length of the large recirculation behind the structure decreases. In addition, as the flow tend to follow the angle of the front face after separation, the height of the recirculation reduces as the structure becomes flat. Furthermore, the increasing α gradually suppresses the vortices on front and back faces, (1) and (2) from figure 10 (a), of the structure because the flow tends to be attached to the structure surface as seen in Figure 10 (b).

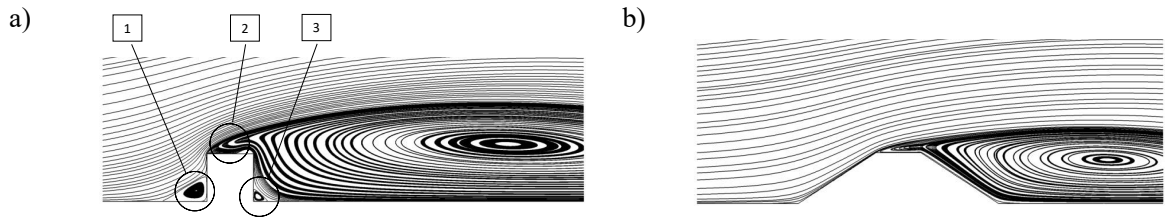

Figure 10. Detailed stream lines for $\mathrm{Re} = 1 \times 10^6$ for (a) $\alpha = 0°$ and (b) $\alpha = 60°$

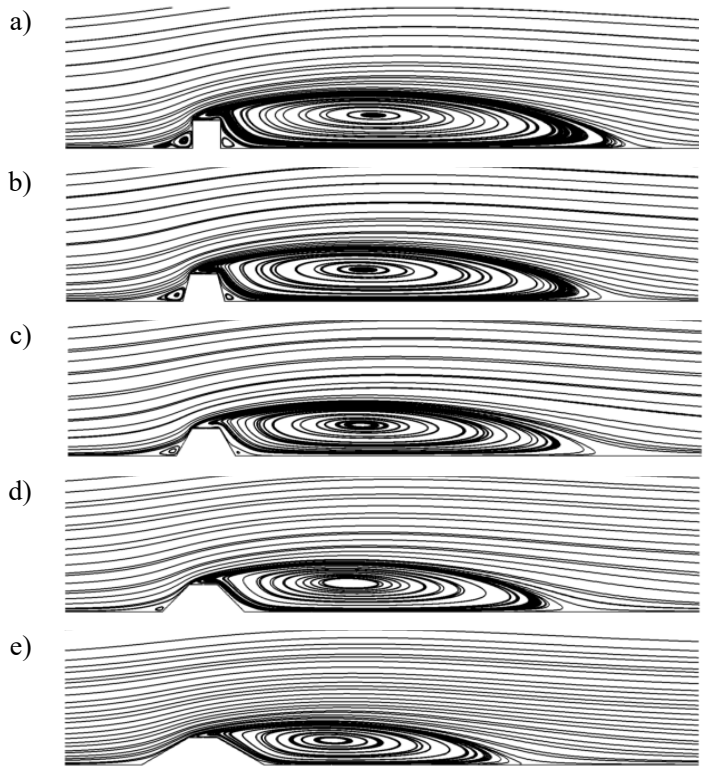

Figure 11. Stream lines at $\mathrm{Re} = 1.19 \times 10^5$ for varying α: (a) 0°, (b) 15°, (c) 30°, (d) 45° and (e) 60°

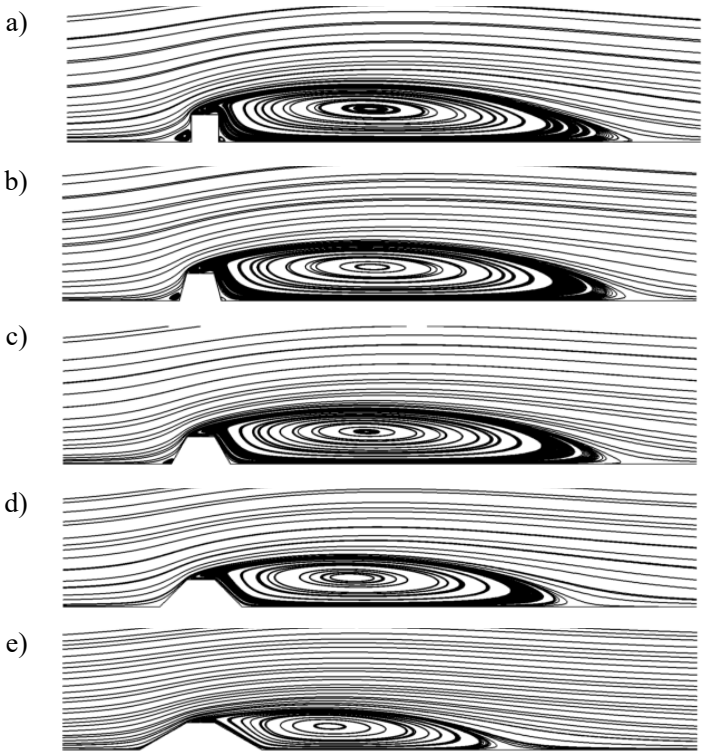

Figure 12. Stream lines at $\mathrm{Re} = 1 \times 10^6$ for varying α: (a) 0°, (b) 15°, (c) 30°, (d) 45° and (e) 60°

Conclusion

Two-dimensional numerical simulations of turbulent boundary layer flows at high Reynolds numbers around square and trapezoidal wall-mounted structures have been carried out. The effects of different bottom angles of the trapezoids on hydrodynamical quantities have been investigated. The simulations are based on RANS equations using the $k - \omega$ SST model combined with a wall function. The resulting drag coefficient (C_D) at $Re = 1.19 \times 10^5$ shows good agreement with that of experimental data. The horizontal velocity profiles at different locations near the square match well with those from the experiments (Liu et al. 2008) except that there is overprediction near the free stream because of the $k - \omega$ SST model. The validation shows that the present numerical model can provide satisfying results when used to study the hydrodynamic characteristics of different wall-mounted structures subjected to a boundary layer flow. Main conclusions can be outlined as follows:

1. The hydrodynamic quantities C_D , C_L and x_R/D all decrease with increasing α for trapezoidal configurations.
2. The main contribution of drag forces on the structures comes from the pressure difference between the front and back face of the structures. However, as α decreases, the viscous drag becomes more significant on the total drag.
3. The vortices on the back and front face of the structures dissipates with increasing angle of α.
4. The absolute minimal value of the bed shear stress is highest for the square configuration and lowest for α = 60°.

References

ARIE, Mikio, et al. "Flow over rectangular cylinders immersed in a turbulent boundary layer: Part 2 flow patterns and pressure distributions." *Bulletin of JSME* 18.125 (1975): 1269-1276.

Brørs, B. "Numerical modeling of flow and scour at pipelines." *Journal of hydraulic Engineering* 125.5 (1999): 511-523.

Liu, Y. Z., F. Ke, and Hyung Jin Sung. "Unsteady separated and reattaching turbulent flow over a two-dimensional square rib." *Journal of Fluids and Structures* 24.3 (2008): 366-381.

Martinuzzi, R., and C. Tropea. "The flow around surface-mounted, prismatic obstacles placed in a fully developed channel flow." *Transactions-American Society of Mechanical Engineers Journal of Fluids Engineering* 115 (1993): 85-85.

Menter, Florian R., Martin Kuntz, and Robin Langtry. "Ten years of industrial experience with the SST turbulence model." *Turbulence, heat and mass transfer* 4.1 (2003): 625-632.

Meroney, Robert N., and David E. Neff. "Wind effects on roof-mounted solar photovoltaic arrays: CFD and wind-tunnel evaluation." *The Fifth International Symposium on Computational Wind Engineering (CWE 2010)*. 2010.

Nielsen, Anders Wedel, et al. "Flow and bed shear stresses in scour protections around a pile in a current." *Coastal Engineering* 72 (2013): 20-38.

Ong, Muk Chen, et al. "Numerical simulation of flow around a circular cylinder close to a flat seabed at high Reynolds numbers using ak–ε model." *Coastal Engineering* 57.10 (2010): 931-947.

Ryu, D. N., Do Hyung Choi, and V. C. Patel. "Analysis of turbulent flow in channels roughened by two-dimensional ribs and three-dimensional blocks. Part I: Resistance." *International Journal of Heat and Fluid Flow* 28.5 (2007): 1098-1111.

Tauqeer, Muhammad Ahmad, Zhong Li, and Muk Chen Ong. "Numerical simulation of flow around different wall-mounted structures." *Ships and Offshore Structures* 12.8 (2017): 1109-1116.

Zhao, X. F., Li, L., Ba, Q., & Ou, J. P. (2012). Scour monitoring system of subsea pipeline using distributed Brillouin optical sensors based on active thermometry. *Optics & Laser Technology*, *44*(7), 2125-2129